Beam Characterization and Systematics of the Bicep2 and Keck Array Cosmic Microwave Background Polarization Experiments

Beam Characterization and Systematics of the BICEP2 and Keck Array Cosmic Microwave Background Polarization Experiments

A dissertation presented

by

Chin Lin Wong

to

The Department of Physics Department

in partial fulfillment of the requirements

for the degree of

Doctor of Philosophy

in the subject of

Physics

Harvard University

Cambridge, Massachusetts

September 2014

Dissertation advisor

John M. Kovac

Author

Chin Lin Wong

Beam Characterization and Systematics of the BICEP2 and Keck Array Cosmic Microwave Background Polarization Experiments

Abstract

Inflation, which posits an exponential expansion in the early universe, is well motivated since it resolves questions that are left unexplained by standard ΛCDM cosmology, such as the flatness and homogeneity of the universe. The exponential expansion of universe during inflation explains the structure in the universe by freezing out the quantum fluctuations of space. These quantum fluctuations are also expected to generate a background of gravitational waves which would then imprint a B-mode polarization signal on the Cosmic Microwave Background.

The BICEP2 and Keck Array experiments search for B-mode polarization from inflationary gravitational waves in the Cosmic Microwave Background. BICEP2 and the Keck Array use small aperture, cold, on-axis refracting optics optimized to target the degree angular scales at which the inflationary B-mode polarization is expected to peak. In this thesis we describe the optical design of BICEP2 and the Keck Array. The small aperture design allows us to fully characterize the far-field performance of the instrument on site at the South Pole using thermal and amplified sources on the ground. We describe the efforts taken to characterize the main beam shapes of each polarization sensitive bolometer, as well

as the differential beam paramters of each co-located orthogonally polarized detector pair. We study the residual temperature to polarization leakage induced by the beam mismatches after the principle modes have been mitigated in the analysis.

Contents

Acknowledgments

Graduate school has allowed me experiences that I would never have had otherwise. I would not have gotten this far without all the support, help and encouragement that I've received from many, many people along the way. I thank here a small subset of everyone that has supported me in my endeavors:

John Kovac, my advisor, without whom I would never have gotten this far. Thank you for taking me on as a student, and guiding me through the travails of graduate school. Thank you for teaching me how to do science. Most of all, thank you for your patience. I know I try it all the time.

Colin Bischoff, for being awesome and answering all, and I mean ALL, my questions. Abigail Vieregg, for being there in the trenches with me. Lab is so different now that you've left for greener pastures. Immanuel Buder, for helping me with all my work. Without everyone's help, encouragement, and knowledge, I doubt that I would have had such an easy time understanding. Thank you all for teaching me.

Melissa Franklin, without whose advice I probably would have floundered very early in this entire journey. Daniel Eisenstein for all the advice.

Kirit Karkare, thanks for keeping me company, and being a fun presence at the other end of the desk. Jake Connors, Kate Alexander, Victor Buza, thanks joining us and spicing things up.

Sarah Stokes Kernasovskiy, for being my friend in arms. All the months we spent in the women's restroom at Pole, and the weeks we spent writing. Your optimism and cheer kept me going. Dima Kernasovskiy, for being so kind as to house and feed me.

The BICEP2 and the Keck Array Collaboration, thank you for the chance to work on the two coolest experiments ever. Jamie Bock, Clem Pryke, Chao-Lin Kuo, thank you

for all your wisdom in leading the collaboration and for the comments you gave to me on my postings. Chris Sheehy, Jamie Tolan, Randol Aikin, Justus Brevik, Walt Ogburn, Zak Staniszewski, Jeff Filippini, Roger O'Brient, Martin Leuker, Stefan Fliescher, Grant Teply, Jon Kaufman, the rest of the BICEP2 and Keck crew, without whom I would not have nearly as much fun, and or got nearly as much done. Thanks for all the help!

Edward Tong, Robert Kimberk, Pat Riddle, Steve Leiker, Ray Blundell, Yury Lobanov, and the entire SMA Receiver Lab, for being so kind to us when we first arrived (and even now when we're mostly set up), and loaning us everything we need. Thanks for all the help and advice, and for being the lab next door.

Irene Coyle, Sarah Block, Peggy Herlihy, Sheila Ferguson, Lisa Cacciabaudo, Kathy Deniston, Barbara Wertz, thank you for all the administrative support that I could possibly need. Things would not have been as efficient without you.

Steffen Richter, Robert Schwarz, for taking such good care of BICEP2 and Keck!

Laura Jeanty, Jayson Paulose, Sofia Magkiriadou, Nick Hutzler, Julia Piskorski, Eddie Schlafly, Yiwen Chu, Renee Sher, Jack DiSciacca, my cohort in Physics, for being companions in this long journey.

Alana Firl, for sustaining me with frequent telephone calls throughout this entire seven years. Thank you for reminding me to read, write and think. Tongyan Lin, for being an example of how successful we can be. I've missed you this last two years. Jihye Seo, for making me go out to every single thing you can think of. I've missed your company at the ballet terribly. Allison Chang, for being a calm, assured presence in the last eleven years. Have I known you for that long? Emily Chang, for being present, and reminding me to have fun. Amy Sutton, for listening to me complain all the time; you have been so kind,

and so much a pillar of support.

Eleanor Millman, Gail Chan, Irina Balea, Katie Boronow, Matt Thornton for putting up with my messy, messy living habits and being such awesome people to come home to. I will miss you and our triangular apartment!

My sisters, Chin Pin and Min Min, for keeping me on my toes.

Lastly, my parents, who have always expected me to be the best that I can be. Thank you for letting me go so far for so long. This is for you.

For my parents

Chapter 1

Inflation and the Standard Model of Cosmology

ON MARCH 17TH, 2014, BICEP2 released a paper reporting on the detection of B-mode polarization at degree angular scales. The observed spectrum is well fit by a lensed-ΛCDM model with tensors at a tensor-to-scalar ratio, $r = 0.20^{+0.07}_{-0.05}$ with $r = 0$ disfavored at 7.0σ with no foreground subtraction. BICEP2, remarkably, has fulfilled its purpose and found the signal it was built to look for, to the consternation of everybody in the field.

A detection of tensor B-modes from gravitational waves originating in the early universe has far ranging implications in the study of cosmology as well as particle physics. This detection would be able to provide us a view of the early universe at 10^{-36} seconds after the beginning of the universe, allowing us to see much farther back in time than we ever have before. A detection of a signal due to primordial gravitational waves will inform us about the early universe and the tensor-to-scalar ratio measured will be able to tell us the energy scale at which inflation occurred, thus validating or invalidating many varied

theories of inflation. In addition, since tensor B-modes are theorized to be caused by the perturbations of primordial gravitational waves, a detection of primordial B-mode polarization could be an indication that gravity is quantized [45]. As such, the BICEP2, and Keck Array experiments are built with a single purpose in mind: to try to detect B-mode polarization from inflation, or to place the most stringent upper-limit currently possible on the existence of tensor B-modes.

The BICEP1 experiment published results from the three year data set in 2013. At that point, the BICEP1 experiment set the most stringent upper limit on the measured B-mode spectrum of $r < 0.70$ [6]. Planck and SPT had placed indirect upper limits of $r < 0.11$ based on the low-multipole measurements of the temperature spectrum [64, 53]. The design sensitivity of BICEP2 and Keck Array was to reach sensitivities that allowed measurements of the B-mode spectrum down to $r \sim 0.02$.

1.1 Cosmic Microwave Background

Standard ΛCDM cosmology has had huge success with describing the universe that we live in today. The existence of the Cosmic Microwave Background (CMB) and the observed expansion of the universe support the theory that the universe started in a small, hot, dense state which then expanded and cooled to become what it is today.

The CMB was emitted 380,000 years after the beginning of the universe, when the universe had expanded and cooled enough for atoms to form. Today, the CMB is measured to be 2.7 K [29], and is uniform throughout the entire sky to a level of 10^{-5}. The density perturbations at the surface of last scattering interacts with the temperature of the radiation to create temperature fluctuations in the CMB that are at a level of 10^{-5}. Figure 1.1 shows

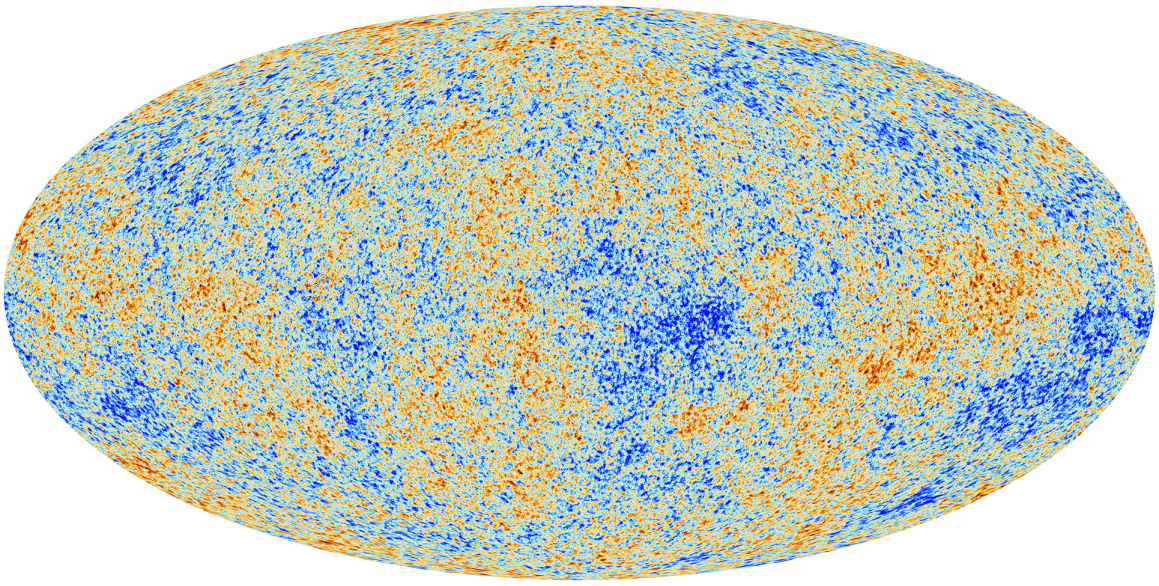

Figure 1.1: Cosmic Microwave Background temperature anisotropies as mapped by the Planck satellite [52]. The level of temperature fluctuations here are at a level of 10^{-5}. *Figure from [52].*

a map of the Cosmic Microwave Background temperature anisotropies as mapped by the Planck Satellite [52].

The temperature fluctuations of the CMB can be expanded as function of spherical harmonics, $Y_{\ell,m}$. We follow the derivation/expansions found in [16, 9]

We have

$$\Delta T(\hat{\mathbf{n}}) = \sum_{\ell,m} a_{\ell,m} Y_{\ell,m}(\hat{\mathbf{n}}) \tag{1.1}$$

where $\Delta T(\hat{\mathbf{n}})$ is the temperature fluctuation at point $\hat{\mathbf{n}}$ on the sky. The angular power spectrum, C_ℓ is defined as follows

$$C_\ell = \frac{1}{2\ell+1} \sum_m |a_{\ell,m}|^2 \tag{1.2}$$

The correlation between the temperature anisotropy at two different points in the sky is

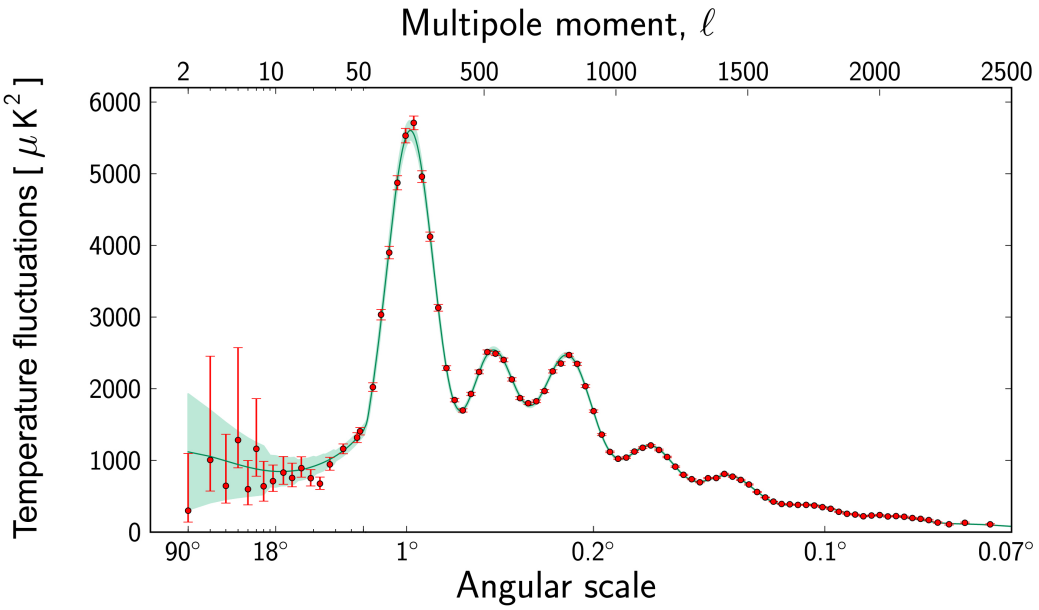

Figure 1.2: Cosmic Microwave Background temperature power spectrum as measured by the Planck satellite [52]. The level of temperature fluctuations here are at a level of 10^{-5}. *Figure from [52].*

then

$$\langle \Delta T(\hat{\mathbf{n}}_1) \Delta T(\hat{\mathbf{n}}_2) \rangle = T^2 \sum_\ell \frac{2\ell+1}{4\pi} C_\ell P_\ell(\cos\theta) \tag{1.3}$$

where $P_\ell(x)$ are the Legendre polynomials.

We take the mean square of this value to obtain

$$\langle \Delta T^2 \rangle = T^2 \sum_\ell \frac{2\ell+1}{4\pi} C_\ell \tag{1.4}$$

where we usually plot $\ell(\ell+1)C_\ell/2\pi$, the power of the temperature anisotropies as a function of angular scale, ℓ, as can be seen in Figure 1.2.

The CMB temperature anisotropy has been studied at very high precision to small angular scales [10, 32, 64, 33, 63, 20, 52, 53], allowing tight constraints to be placed on

parameters of standard ΛCDM cosmology. The temperature power spectrum allows us to measure and constrain various cosmological parameters such as the curvature and the matter density of the universe. High precision measurements of the CMB constraining the flatness and homogeneity of the universe have highlighted questions that are left unanswered by the standard model of cosmology.

One of the major problems in the standard model of cosmology is the horizon problem. The horizon problem poses the question of how the universe became so homogeneous. Measurements of the CMB shows us that the entire sky is uniform to one part in 10^5. However, in the standard model, causally connected regions at the surface of last scattering when the CMB was emitted correspond to about one degree in the sky today. The standard model of cosmology has no explanation of how parts of the sky that are larger than one degree apart come to have such similar temperatures, besides assuming that the universe began in very homogeneous conditions.

Measurements of the CMB show that the universe is very close to being flat. The flatness of the universe requires the density of the universe to be almost exactly the critical density. However, the flatness of the universe is an unstable solution. Any small deviations from the critical density during the early universe will result in a positively or negatively curved universe today. The flatness of the universe is a fine-tuning problem that is left unexplained by the standard model of cosmology.

1.2 Inflation

Inflation [30, 47] is a class of theories that posits the exponential expansion (10^{26} times) of space a fraction of a second (10^{-35} s) after the beginning of the universe. This period of

exponential expansion stretched space very quickly in a very short amount of time, before allowing the universe to evolve as we theorize in the standard model of cosmology.

Inflation solves the horizon problem by ensuring that the universe was very small and completely causally connected before inflation occurred. The rapid expansion of space caused all the causally connected regions to be frozen and stretched out into scales outside the horizon. As the universe expands, these super-horizon modes start moving into the horizon and as such, when we observe the universe today, we see the parts of the universe that were causally connected when the universe began.

Inflation solves the flatness problem by stretching out space so quickly that no matter what the initial density of the universe is, the density of the universe after inflation is driven close to the critical density, allowing the universe to still be flat today.

In addition to solving the flatness and horizon problems, inflation also explains the origin of the density perturbations in the universe. The rapid exponential expansion of space freezes out the quantum fluctuations of space, making these fluctuations real, thus generating the density perturbations in the early universe that eventually grow to become the stars and galaxies in the universe today. We see the density perturbations of the early universe in the temperature fluctuations of the CMB. The freezing out of the quantum fluctuations is also predicted to generate a stochastic background of gravitational waves. These gravitational waves generated at inflation propagate throughout the universe and are expected to leave an imprint on the CMB. This imprint is expected to be seen as a polarization pattern in the CMB called the B-mode polarization pattern.

1.3 Cosmic Microwave Background Polarization

The density perturbations at the surface of last scattering that source the temperature anisotropies in the CMB will also source a polarization pattern on the sky. Thomson scattering of electrons off of photons in the plane of the surface of last scattering will result in polarized light scattering towards us [34]. However, it is not enough to simply have Thomson scattering of electrons off photons at the surface of last scattering. If all the incoming photons scattering off the electron from all directions have the same energy, the net polarization of light scattered towards us will be zero. For the light scattering towards us to be polarized, there has to be at least a quadrupolar anisotropy around the electron at the surface of last scattering. This is illustrated in Figure 1.3.

The polarization of light is generally described using the Stokes parameters ($\mathbf{I}$, $\mathbf{Q}$, $\mathbf{U}$, $\mathbf{V}$), where $\mathbf{I}$ is the intensity of the light, $\mathbf{Q}$ and $\mathbf{U}$ are the linear polarization parameters in the horizontal/vertical directions and the diagonal directions respectively, and $\mathbf{V}$ is the circular polarization parameter.

For a wave of light propagating in the $\hat{z}$ direction, we describe the electric field in the $\hat{x}$ and $\hat{y}$ direction (E_x and E_y). The Stokes parameters are defined as

$$\mathbf{I} = \frac{1}{2}(|E_x^2| + |E_y^2|) \tag{1.5}$$

$$\mathbf{Q} = \frac{1}{2}(|E_x^2| - |E_y^2|) \tag{1.6}$$

$$\mathbf{U} = \frac{1}{2}(E_x^* E_y + E_y^* E_x) \tag{1.7}$$

$$\mathbf{V} = i\frac{1}{2}(E_x^* E_y - E_y^* E_x) \tag{1.8}$$

For BICEP2 and the Keck Array, the $\mathbf{Q}$ and $\mathbf{U}$ polarization components are measured with respect to the (RA, DEC) coordinate system we make our maps in.

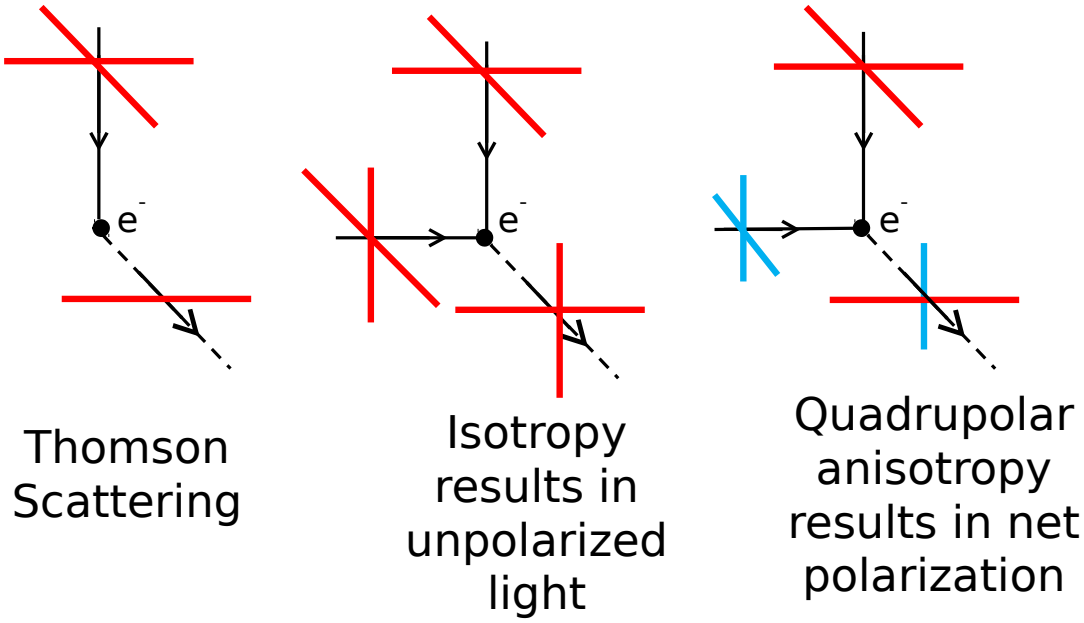

Figure 1.3: Left: Thomson scattering of photons off electrons at the surface of last scattering produce linearly polarized light directed towards us. Center: However, if the incoming photons all have the same energy, the scattered light will not have a net polarization. Right: A quadrupolar anisotropy is also required to produce a net polarization of light. *Figure after [34].*

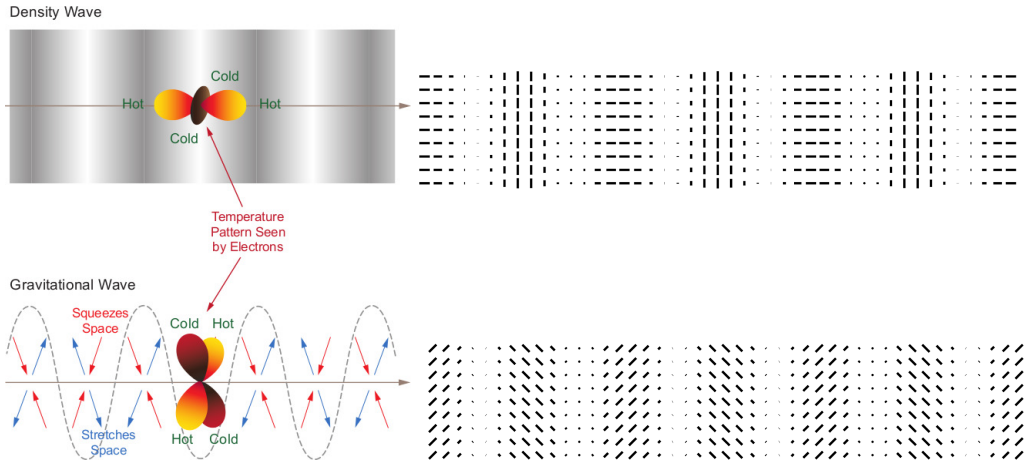

Figure 1.4: Density perturbations are expected to only create E-mode polarization patterns. In order to generate B-mode polarization patterns an additional direction has to be added into the problem. Gravitational waves from inflation are expected to generate both E-mode and B-mode polarization patterns. *Figure from* BICEP*/Keck Collaboration*.

In CMB observations, we use a completely equivalent description of polarization. We can decompose the polarization pattern on the sky into an E-mode polarization pattern and a B-mode polarization pattern [38, 59]. The advantage of this decomposition is that the E-mode polarization pattern is scalar, while the B-mode polarization pattern has a curl component.

The density perturbations at the surface of last scattering are scalar and therefore can only source an E-mode polarization pattern on the sky. A B-mode polarization pattern requires an additional direction to be introduced into the problem. Gravitational waves from inflation would stretch and squeeze space and influence the polarization pattern in the CMB. These gravitational waves will produce both E-mode and B-mode polarization as shown in the bottom panel of Figure 1.4.

We parameterize the expected level of the tensor perturbations with $r = \frac{T}{S}$, the ratio of the power of the tensor modes, T, to the scalar modes, S. The expected spectrum of

B-mode polarization from gravitational waves is expected to peak at $\ell = 100$, at degree angular scales. The height of the peak directly corresponds to the tensor-to-scalar ratio, r, and is an indication of the energy scale at which inflation occurred.

Figure 1.5 shows the temperature and polarization power spectra. The black line indicates the temperature spectrum. The E-mode polarization spectrum, which is primarily due to density perturbations, is shown in blue. Since the E-mode spectrum is related to the same density perturbations that source the temperature spectrum, there is a cross correlation between the temperature and E-mode polarization spectrum shown in the green line in the lower panel. The dashed lines show the expected spectrum generated by the gravitational waves from inflation. The contribution to the temperature and the E-mode power spectrum from gravitational waves is almost negligible. The dashed red line indicates the contribution of B-mode polarization for a tensor-to-scalar ratio $r = 0.1$. Also shown is the B-mode spectrum from the gravitational lensing of the E-mode polarization into B-mode polarization. Note that at smaller angular scales, the B-mode polarization from inflation decays away, and the B-mode polarization from gravitational lensing dominates. In order to try to detect the inflationary B-mode signal, we build our telescopes in order to concentrate as much sensitivity as possible at the degree angular scales.

1.4 Current Status

The E-mode polarization was first detected by the DASI experiment [44]. Measurements were further refined by many experiments such as CAPMAP [7, 11], CBI [57, 62], WMAP [51, 10], BOOMERANG03 [48], MAXIPOL [67], QUAD [54, 15], BICEP1 [19, 6], QUIET [55, 56], ACTPOL [49]. The most recent E-mode polarization measurement has

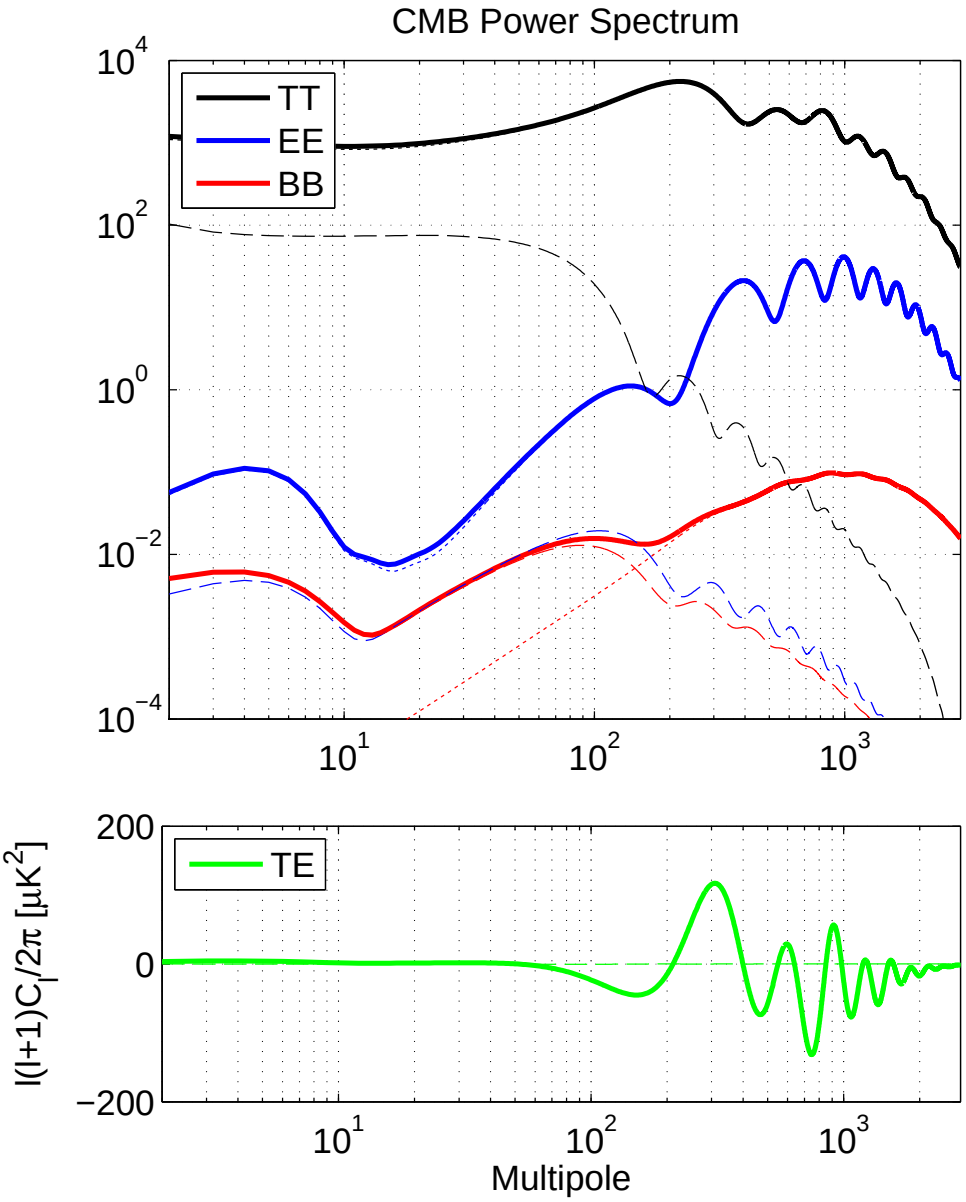

Figure 1.5: The TT, EE, BB and TB spectra. The dashed lines show the potential contribution from stochastic gravitational waves from inflation to the TT, EE, and BB amplitudes for the tensor-to-scalar ratio of $r = 0.1$. The dotted line indicates the power of B-modes from gravitational lensing of the E-mode polarization to B-mode polarization. The peak of the BB spectrum from primordial gravitational waves is expected to peak at $\ell \sim 100$, and so BICEP2 and the Keck Array are built to target polarization at degree angular scales. *Figure from [42].*

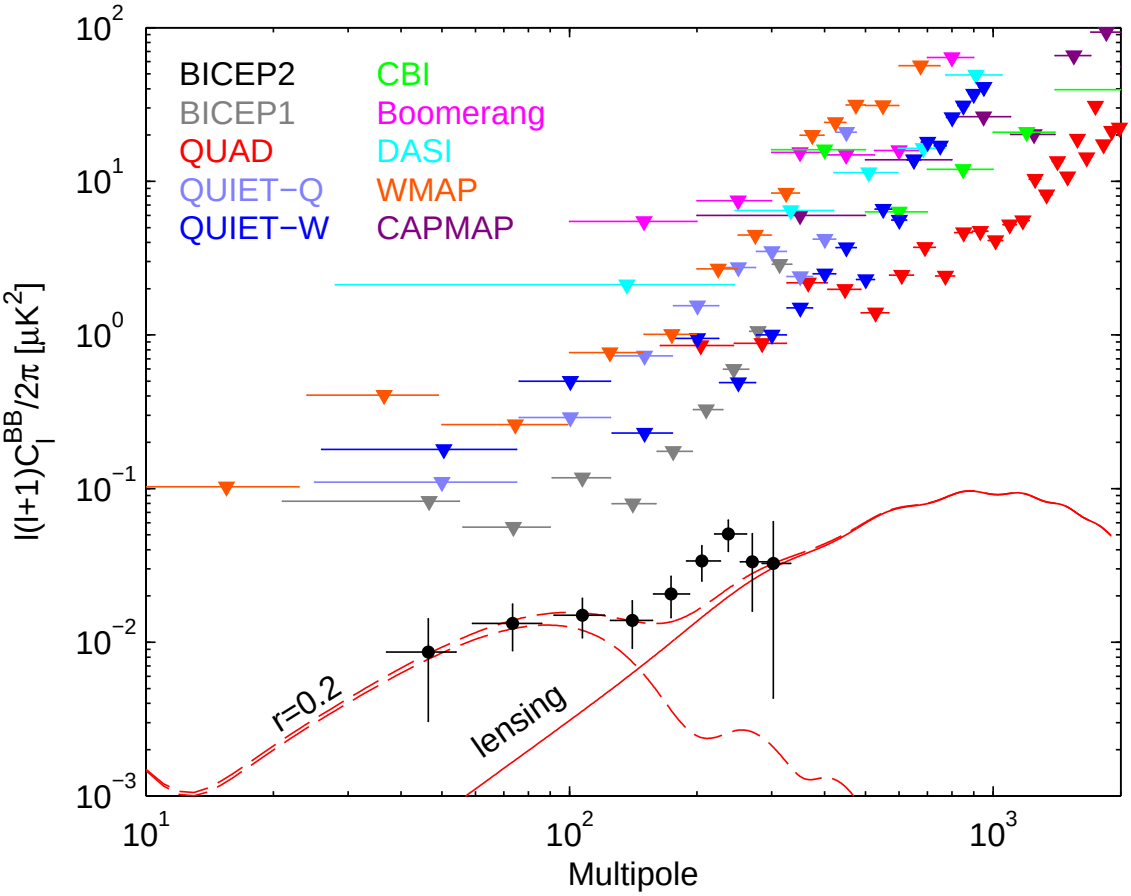

Figure 1.6: The B-mode polarization power spectrum as measured by BICEP2. The power spectrum is well fit by a primordial gravitational wave spectrum with tensor-to-scalar ratio of $r = 0.2$, with no foreground subtraction. *Figure from [2].*

been published by ACTPOL [49], measuring the E-mode polarization spectrum at $200 < \ell < 9000$.

BICEP2's measurement of the B-mode polarization at degree angular scales can be seen in Figure 1.6. The tensor-to-scalar ratio constraint set by this measurement (without any foreground removed), is at $r = 0.20^{+0.07}_{-0.05}$, with $r = 0$ disfavored at 7.0σ. I refer to [2] for a full discussion of the measurement and result.

1.5 Thesis Outline

This thesis concentrates on the optical design and manufacture as well as the beam characterization of BICEP2 and the Keck Array. We first describe the BICEP2 and Keck Array experiments in Chapter 2. Then, we describe the design and manufacture of the BICEP2 and Keck Array optics in Chapter 3. The beam calibration efforts and beam parameterizations are described in Chapter 4, while our efforts to understand the temperature-to-polarization leakage from the residual beam mismatches are presented in Chapter 5. Chapter 6 presents a summary of the BICEP2 and Keck Array results.

Chapter 2

The BICEP and Keck Array experiments

THE BICEP AND KECK ARRAY EXPERIMENTS are a series of targeted experiments focused on trying to detect the B-mode polarization pattern from inflation that peaks at degree angular scales. As such, the approach made was to maximize the sensitivity of the instrument to polarization at these scales. The experiments utilize the many advantages of small-aperture telescopes that have large throughput in order to effectively detect the B-mode polarization at degree angular scales.

The BICEP and Keck Array series of experiments began with BICEP1 [19, 39] which observed from February 2006 to December 2008. BICEP1 is a LN2 and LHe cooled cryogenic receiver containing a 250 mm diameter refracting telescope that directs incoming radiation to polarization sensitive semiconductor bolometers [69]. These bolometers are radiation coupled using corrugated feedhorns which limits the number of detectors deployed. BICEP1's focal plane can be seen in Figure 2.1. BICEP1 observed with 50 detectors at 100 GHz, 44 detectors at 150 GHz, and 4 detectors at 220 GHz, for a total of 49 polarization

pairs. BICEP1 published results from the two-year data set in 2010 [65, 19], and the full three year data set in 2014 [6]. The 95% upper limits set on B-mode polarization from BICEP1 is at $r = 0.7$ [6], which was the most stringent upper limit on the B-mode power spectrum at the time.

BICEP2 [1] follows the successes of BICEP1 by using a similar concept but taking advantage of new developments in detector technology to deploy a focal plane of 512 polarization sensitive detectors. Instead of using feedhorns, BICEP2 used photolithographed planar array antennas [12] coupled to transition-edge sensor bolometers. This allowed BICEP2 to deploy five times the number of detectors in a focal plane of nearly the same size as BICEP1. The BICEP2 focal plane can also be seen in Figure 2.1. The increase in the number of detectors as well as in the improvements in detector technology increased the mapping speed by a factor of 10. BICEP2 was deployed in December 2009, using the existing BICEP1 mount at the Dark Sector Laboratory (DSL) at the South Pole and took three seasons of data from February 2010 until it was decommissioned in December 2012.

The transition-edge sensor bolometers that BICEP2 uses are photon-noise dominated. As such, in order to increase the sensitivity of the instrument, we would need to increase the number of detectors that we were using. The Keck Array takes advantage of the technology developed for BICEP2 by deploying five times the number of receivers as BICEP2 on the DASI mount. In this chapter, we describe the Keck Array, starting with the cryogenics, before moving onto the detectors and the multiplexing and readout system. We then describe the groundshield and forebaffle and finish with a short description of the observing strategy.

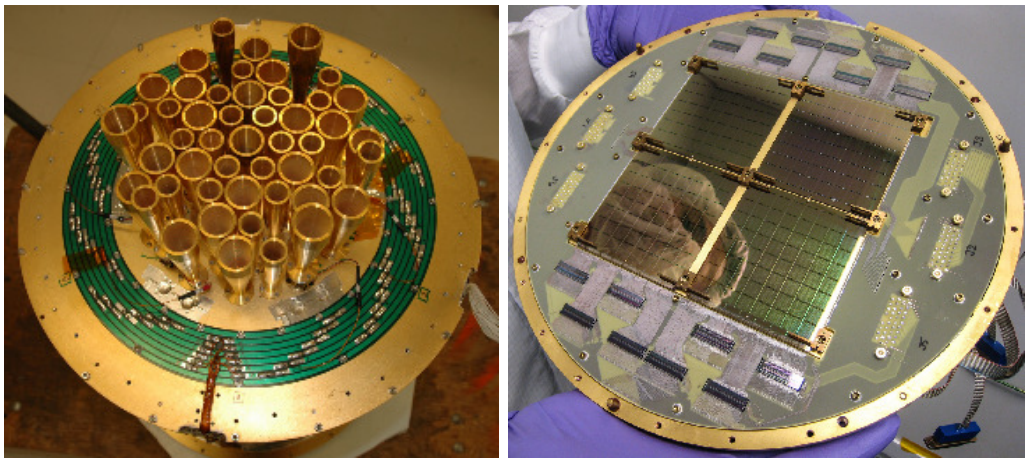

Figure 2.1: Left: The BICEP1 focal plane has 50 pixels, each pixel consisting of a feedhorn coupled to a pair of semiconductor bolometers. *Photograph from* BICEP*1 Collaboration.* Right: BICEP2 quintuples the number of pixels in its focal plane using photolithographed slot-array antennas coupled to transition edge sensor bolometers, increasing the sensitivity of the instrument. *Photograph by Anthony Turner.*

2.1 The Keck Array

The Keck Array [61, 41] deployed three receivers at 150 GHz in November 2010, and completed the full array by deploying two additional receivers in November 2011 for a total of five receivers observing at 150 GHz for the 2012 observing season. In the 2013 observing season, one tile in Receiver 1's focal plane and the entire focal plane in Receiver 4 were swapped out for improved detectors. Receiver 3's focal plane was also swapped out for BICEP2's focal plane at the beginning of the 2013 observing season. All receivers in 2013 observed at 150 GHz.

The Keck Array is situated on the existing DASI mount at Martin A Pomerantz Observatory (MAPO) at the South Pole, 200 meters away from DSL. Figure 2.2 shows all five of the Keck Array receivers in the DASI mount, with forebaffles installed. In November 2013, two of the Keck Array receivers were replaced with 100GHz detectors as part of an

Figure 2.2: A view of the Keck Array, with five of the receivers in the mount. The outer forebaffles are visible. *Photograph by Robert Schwarz.*

ongoing observation strategy to increase the frequency coverage of data in the sky.

The cryostat shells were built by Atlas Technologies. The cryostat was designed such that the pulse-tube cooler head is placed in a welded extension at the side of the main cryostat shell in order to reduce the possibility of transmitting any vibrational effects. The 50K and 4K stages are isolated from each other and from the 300K stage by using carbon-fiber thermal supports on the bottom end, and using boomerang-shaped titanium supports on the top. The pulse-tube cooler head is connected to the 50K and 4K stages with 5N aluminum foil heat straps, which has a thermal conductance of 1W/K at 4K. Twenty layers

of multi-layer insulation (MLI) are used to reduce the radiative loading and shield the 300K stage from the 50K stage, while only a single layer of aluminized mylar separates the 50K stage from the 4K stage. There is a layer of high magnetic permeability material Amuneal[1] Amumetal 4K (A4K) wrapped around the 50K shell to decrease the influence of the magnetic field within the cryostat.

The entire 4K stage sits on a copper plate which is gold-plated to increase thermal conductivity. The 4K insert holds the focal plane, the adsorption refrigerator which cools the detectors, and is connected to the optics tube. The focal plane is held thermally isolated from the rest of the cryostat with a carbon-fiber truss support. The entire focal plane system is surrounded with a niobium cylinder, which is held at 350 mK and therefore superconducting ($T_C = 9.3$K), repelling stray magnetic fields, as well as ensuring that the loading onto the focal plane is manageable.

2.2 Cryogenics

The Keck Array uses Cryomech PT410[2] two-stage pulse-tube cooled cryostats [61], unlike BICEP2 which used a liquid helium-cooled cryostat. Using a pulse-tube cooled system allowed each Keck Array receiver to be smaller than the BICEP2 receiver thus maximizing the number of receivers that we can place within the drum of the DASI mount. This was important as the approach that the Keck Array was taking was to increase the sensitivity of the instrument by deploying as many detectors as possible. Using a pulse-tube cooled cryostat also eliminated the need to ensure a continuous supply of liquid helium

[1] www.amuneal.com

[2] http://www.cryomech.com/

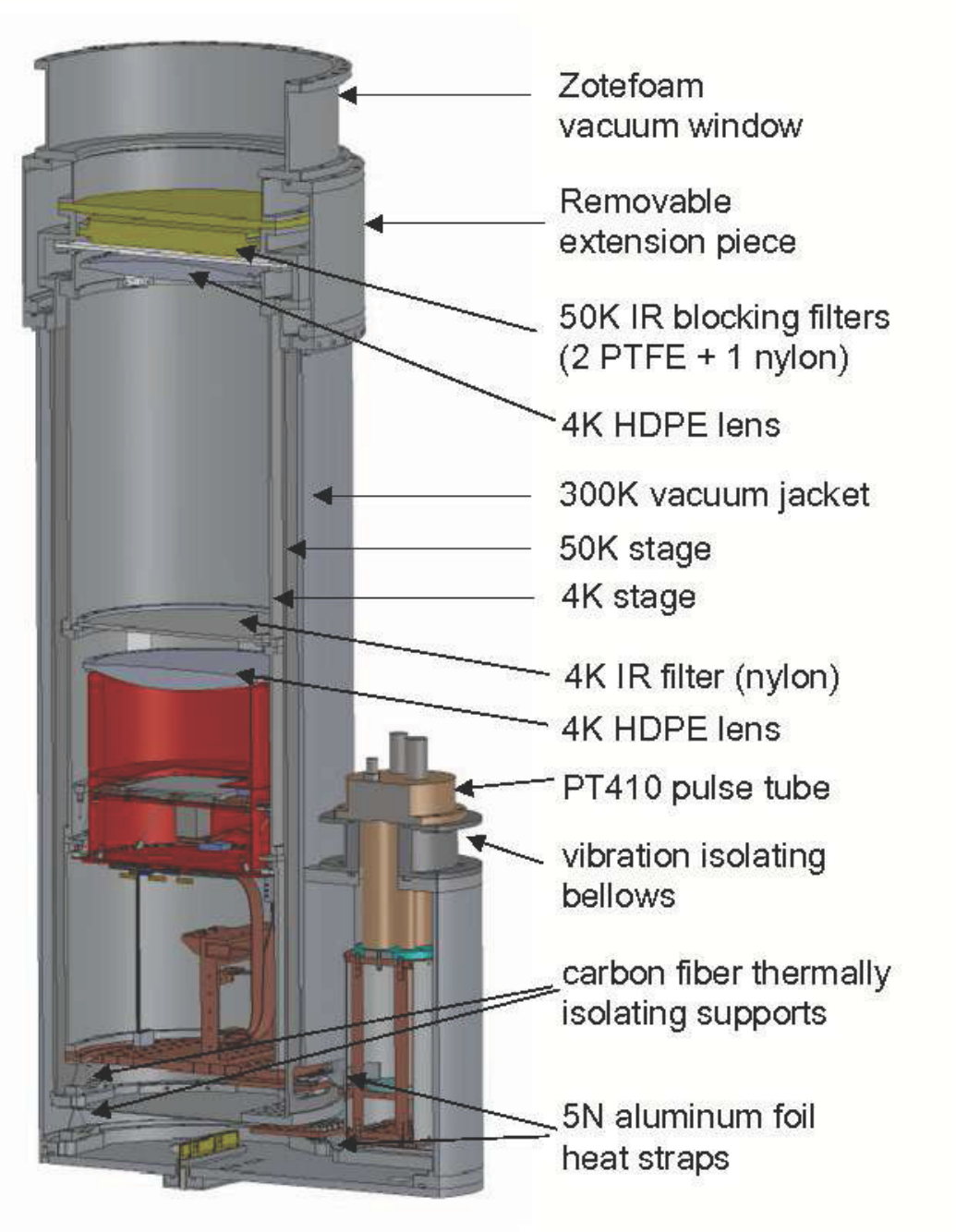

Figure 2.3: A cross section of a single Keck Array receiver. The entire receiver is cryogenically cooled with the optics tube at 4K and the focal plane at 270mK. All the major components of the cryostat are visible. *Figure from [61].*

at the South Pole. However, unlike a liquid helium stage, the pulse-tube cooler supplies limited amounts of cooling power. The PT410's cooling power is 1W at 4K, and 45W at the 50K stage. The pulse-tube coolers are operated at a pulse frequency of 1.2 Hz and are individually tuned for optimal performance.

In order to hold the detectors at their operating temperature of 270 mK, we use a 3-stage helium sorption refrigerator[22]. The fridge is bolted onto the 4K copper base plate, and has one He^4 and two He^3 reservoirs that are pumped on in turn to achieve a final cooling stage at 250 mK with which we cool the focal plane. There is an intermediate cooling (IC) stage at 350 mK that is used to cool the niobium cylinder. The total cooling energy of the intermediate 350mK cooling stage (IC) is 20 Joules while the loading on the IC is 30-60 μK, and the intrinsic loading from the fridge on the IC stage of 30 μK. This limits the fridge holding time to $\sim$2-3 days. The enthalpy of the final 250mK stage (UC) is 1.5 Joules. The loading on the focal plane is stage is ~ 1 μK, while the intrinsic loading from the fridge is ~ 1 μK.

2.3 Detectors

In order to increase sensitivity of the telescopes, BICEP2 and the Keck Array used beam-forming planar-antenna arrays coupled to transition-edge sensor (TES) bolometers[37]. The switch from feedhorn-coupled bolometers in BICEP1 to planar antenna arrays enabled the BICEP2 and Keck Array focal planes to increase the number of detectors within each receiver. Each focal plane in BICEP2 and the Keck Array has 256 co-located, orthogonally polarized detectors equally distributed on four silicon tiles.

Figure 2.4 depicts a single focal plane [1, 50] in BICEP2 or each of the Keck Array

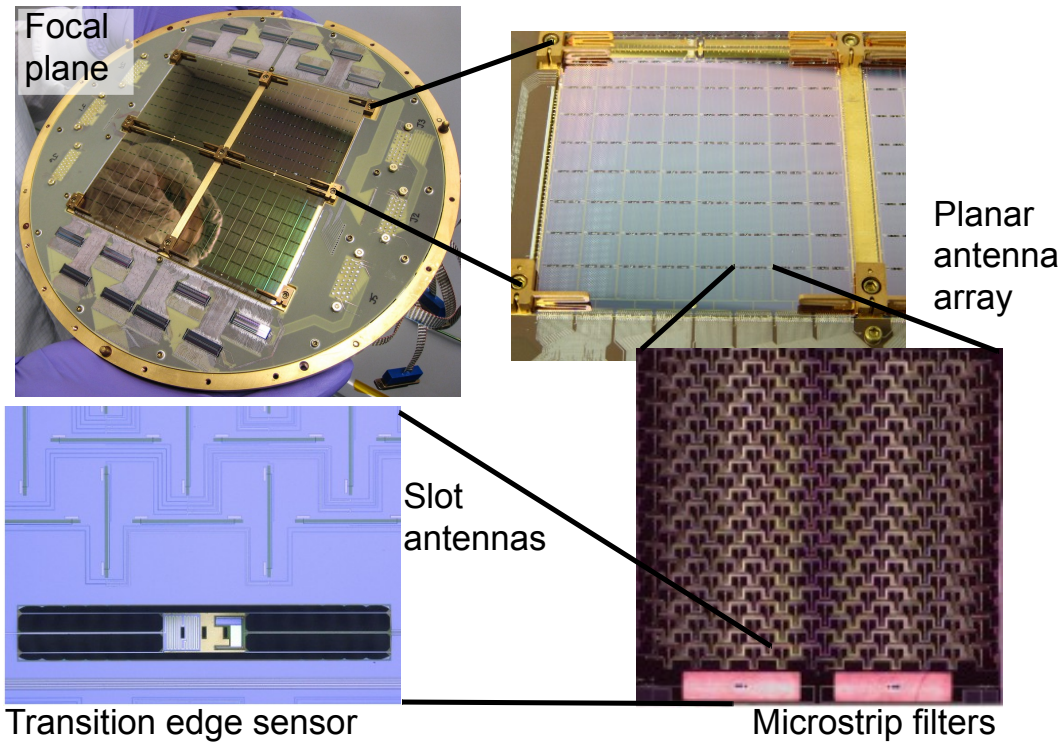

Figure 2.4: The figure on the upper left shows the copper focal plane as used in each of the BICEP2 and Keck Array receivers. Each focal plane holds four tiles, one of which is shown in the upper right. The lower right figure is a zoom in on a single pixel which consists of an array of horizontal and vertical slot antennas. The signals for each orthogonally polarized detector is terminated onto the TES which is shown in the lower left. *Figure from* BICEP2*/Keck Array Collaboration.*

receivers. Each BICEP2 and Keck Array focal plane holds four silicon tiles. Each silicon tile contains an array of 8x8 detector pairs. A single detector pair consists of an array of orthogonally polarized, interleaved dipole slot antennas etched on a superconducting niobium ground plane. In order to detect polarization, we difference the signals coming in from the orthogonally polarized detectors. The current from the planar-array of slot antennas for each polarization is separately conducted by a superconducting summing network through a bandpass filter, and onto a detector island, where the signal is terminated on a lossy gold meander.

The detector island is held thermally isolated from the the wafer on six silicon-nitride (SiN) legs. The detector island also holds the aluminum and titanium bolometers that are joined in series. The titanium bolometer is superconducting at $T_c \sim 500$ mK and is used during science observations. The aluminum bolometer has a higher superconducting temperature (~ 1.2 K) than the titanium bolometer and, as such, is used for calibration measurements in higher loading environments such as in the laboratory.

The TES bolometers are essentially thermometers. The signals that are transmitted from the array of antennas are deposited onto the detector island, which raises the temperature of the island and the bolometer, which in turn increases the resistance of the TES. The TES is joined in parallel with a shunt resistor which has a resistance much lower than the TES. The shunt resistor is current biased, which results in a voltage-bias on the TES, and holds the TES in a negative feedback loop. The TES is biased appropriately in order to hold the superconducting resistor on its transition edge [35].

A balance has to be struck between the heat capacity of the detector island and the thermal conductance of the detector island legs. Both parameters have to be finely tuned in

order to allow the perfect amount of heating of the detector island. If the power deposited is conducted away too quickly, the temperature of the island does not change significantly, and so the detectors are less sensitive. If the power deposited is not conducted away quickly enough, the detector island can easily be saturated, driving the superconducting resistors normal.

On the focal plane, there are eight detector pairs whose antennas are not joined to the detector island, creating "dark detectors" that are not optically coupled, but are integral to understanding the non-optical responsivity of the detector. The dark detectors are insensitive to signals deposited onto the antennas, but will respond in the same way to other effects such as the out-of-band loading and the external magnetic fields.

2.3.1 Detector sensitivity

The detector sensitivity is highly dependent on the bias at which the detectors are held [41, 14]. Theoretically we can bias the detectors to have resistances anywhere on the transition. In practice, a choice of too low a bias might make the electric time constant interact with the thermal time constants such that the detector becomes unstable. A choice of too high a bias reduces the responsivity of the detector, risking saturation when the weather is not optimal (during higher loading conditions). We choose the bias of the detectors appropriately to minimize the noise-equivalent temperature (NET). To do this, we estimate the noise by staring at the sky for all possible biases. There are 16 bias lines, per receiver, each of which are connected to a row of 32 detectors, and so the detector biases are optimized for the entire row of detectors at once.

The BICEP2 and Keck Array detectors are photon noise dominated [41, 14]. Phonon

noise (noise due to the thermal fluctuations of the detector) is the next largest noise component. Also contributing noise in the detectors is a small amount of Johnson noise from the TES and the shunt resistor, and amplifier noise from the cold and warm electronics. More information can be found in [14, 41]

The NET for BICEP2 is 16 $\mu\mathrm{K}_{\mathrm{CMB}}\sqrt{\mathrm{s}}$ and for Keck Array 2012 is 11 $\mu\mathrm{K}_{\mathrm{CMB}}\sqrt{\mathrm{s}}$ and for Keck Array 2013 is 9.5 $\mu\mathrm{K}_{\mathrm{CMB}}\sqrt{\mathrm{s}}$ [42].

2.3.2 Optical Efficiency

The optical efficiency of the detectors is defined to be the fraction of total incoming radiation that is absorbed by the detectors. For a blackbody source that fills the entire aperture, the power deposited on the detectors is

$$P = \eta \int \lambda^2 \tau(\nu) B(\nu, T) d\nu \tag{2.1}$$

where η is the optical efficiency, Ω is the solid angle subtended by the aperture, $\tau(\nu)$ is a function of the detector response in frequency, and $B(\nu, T)$ is the Planck blackbody spectrum. In the Rayleigh-Jeans limit ($h\nu \ll kT$), we have

$$P = \eta k T \Delta\nu \tag{2.2}$$

We measure optical efficiency by filling the aperture with a microwave absorber-lined cone at room temperature and soaked in liquid nitrogen (77K). The difference between the saturation power at the two different temperatures allows us to calculate the optical efficiency effectively without having to rely on absolute power measurements for each detector.

BICEP2 has an average optical efficiency of 38%, while the Keck Array has an average optical efficiency of 21% for 2012 and 31% for 2013 [42]. The Keck Array optical effi-

ciency varies a lot more for each receiver. The variation in the optical efficiency is a result in the variation of the detector fabrication process. As we deployed different focal planes in 2013, the Keck Array optical efficiency for these new focal planes improved.

2.4 Multiplexing and readout

In order to reduce the number of wires that lead to the focal plane, thus reducing the amount of wiring and heating of the focal plane, the detectors are read out using a three-stage time-domain multiplexing system [36, 21]. There are 16 second-stage SQUIDs (referred to as a column), each of which are inductively coupled by a summing coil to 33 first-stage SQUIDs, 32 of which are inductively coupled to the detector. The change in current running through the TES will be read out by the first stage SQUIDs sequentially (time-domain multiplexing). The 33rd SQUID is left disconnected from any detector creating 16 "dark squids", which respond only to changes in the ambient magnetic field giving us a way of understanding how the magnetic field in the receiver affects the signal from each detector. The 33 SQUID1 and single SQUID2 are on a single chip mounted onto the focal plane. We use 16 chips in order to read out the entire focal plane worth of detectors.

The SQUID2s are readout by SQUID series array (SSA) which are at 4K. The SSAs are a series of 40 squids designed to match the impedance of the room-temperature readout. The warm multiplexing electronics is read out by the multi-channel electronics (MCE) system developed by University of British Columbia [8].

2.5 Groundshield and Forebaffle

The forebaffle and groundshield are part of a system designed such that stray radiation from the ground is prevented from entering the telescope. Stray radiation from the ground has to refract at least twice (once on the lip of the groundshield, and once on the lip of the forebaffle) before entering the telescope, thus reducing the possibility of stray radiation contaminating the signal from the sky. The groundshield for the Keck Array is inherited along with the DASI mount, but rebuilt for QUAD and is completely lined with aluminum in order to reflect anything that enters the groundshield back to the sky[69].

A combination of the height and width of the forebaffle has to allow the maximum opening angle of the telescope to be unobstructed. The maximum width of the forebaffle is constrained by the position of each Keck Array receiver to the next. However, the forebaffle also has to be tall enough such that there is no direct line of sight between the window and the edge of the groundshield at any position, particularly at the lowest elevation step. This ensures that stray reflections off the lip of the groundshield does not enter the receiver.

The Keck Array forebaffle is designed to be 25 inches in diameter, and 29 inches in height (Figure 2.5) after taking into account all the constraints imposed on it. The allowed opening angle calculated from the lower edge of the window frame is 9.6° allowing clearance for the edgemost pixel which is 9.1° from the boresight. Figure 2.6 shows that the forebaffle is designed to be tall enough such that there is a 6° clearance between the top of the groundshield and radiation entering the receiver from the lip of the forebaffle at a conservative elevation offset of 50.29°

The inner surface of the forebaffle is coated with Eccosorb HR10[3] which is adhered to

[3]http://www.eccosorb.com

the aluminum using RTV 6708 silicone sealant. Once HR10 has been applied, the front surface of the absorber is covered with a weather-proofing foam called Volara[4] since the forebaffles all sit outside the telescope during winter. The forebaffles are heated to prevent snow accumulation and the reduction of the efficiency of the HR10.

BICEP1's forebaffle loading is $\sim 1K_{RJ}$ [65]. The forebaffle loading tests performed for Keck showed that the loading on the detectors for BICEP2 and the Keck Array is approximately 4 times higher. The pattern of loading on the detectors show that there is more loading on the center pixels than on the edge pixels. This seems to indicate that there is a wide angular spread in the source of the additional loading [42]. The additional loading is traced to the high incident angle reflections off the inner surface of the telescope tube. The subsequent telescope tubes have been fitted with internal baffle rings that intercept the aberrant radiation.

2.6 Observing Strategy

The BICEP and Keck Array observing strategy is to significantly and quickly increase the possibility of detecting or placing a limit on the existence of B-mode polarization at degree angular scales. There are multiple considerations which go into determining the patch of sky that is observed. The patch of sky that BICEP2 and Keck Array have chosen to observe must be large enough to encompass enough sample variance at degree angular scales. For this consideration, the larger the patch of sky observed, the smaller the error bars from sample variance are, and therefore the more sensitive BICEP and Keck Array are to polarization at degree angular scales. However, observing a larger patch of sky requires

[4]http://www.sekisuivoltek.com/products/volara1/

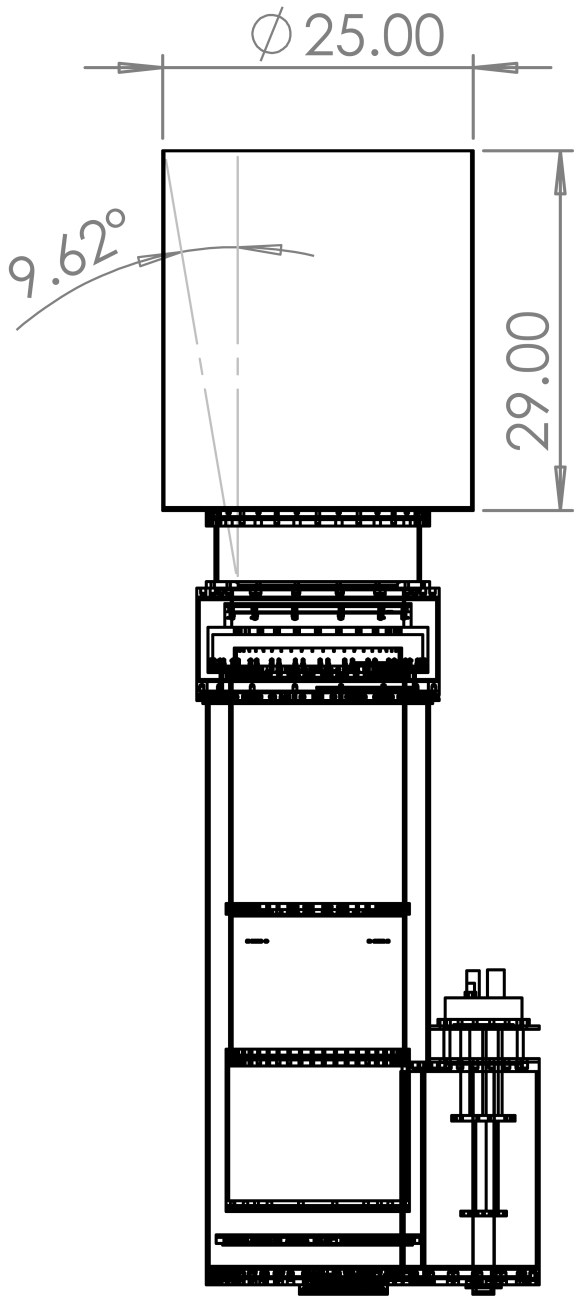

Figure 2.5: The forebaffle allows an opening angle of 9.6° which allows the edge pixels that are 9.1° from the boresight to be unobstructed. The forebaffle also prevents stray radiation 10°-18° from entering the receiver. *Figure by Michael Gordon*.

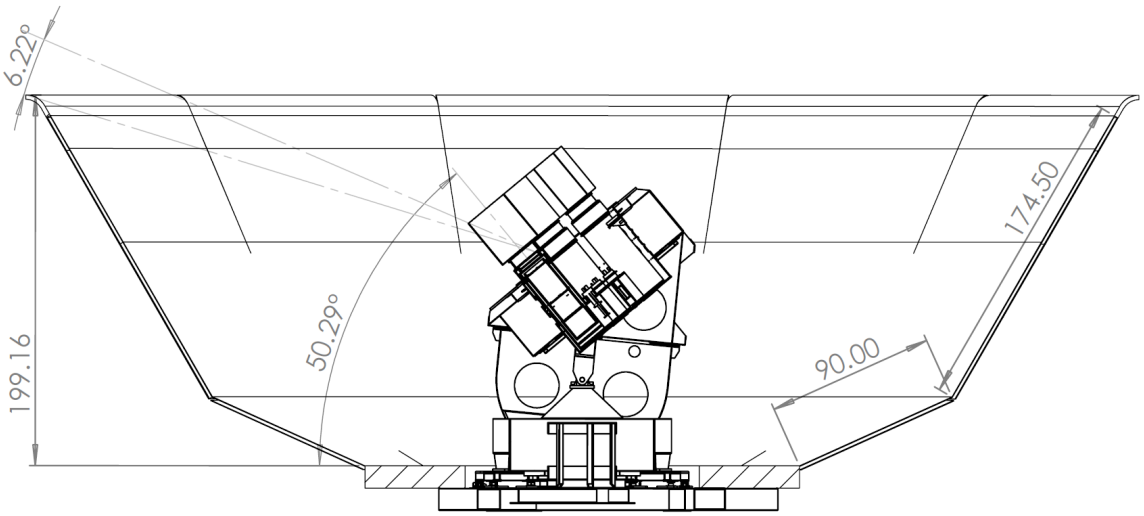

Figure 2.6: The forebaffle and groundshield configuration prevents stray radiation from contaminating the incoming signal from the sky. Stray radiation from the ground has to reflect twice (once off the lip of the ground shield, and once off the lip of the forebaffle) before any possibility of entering the telescope. There is a 6° margin between a direct line-of-sight between the top of the groundshield and the window edge. *Figure by Michael Gordon*.

more time to accumulate sensitivity compared to a smaller patch of sky. Also in play are the expected galactic foregrounds that dominate a large region of the sky particularly in the plane of the galaxy. The larger the galactic foreground signal, the less likely we are to detect primordial signals.

Taking into account all these considerations, BICEP2 and the Keck Array observes $\sim$2% of the sky in an expected low foreground region called the "Southern Hole", visible from the South Pole. The observing region is ~ 1000 square degrees, and centered on RA = 0 hr, Dec = -57.5° and is $\sim 60^\circ$ wide and $\sim 20^\circ$ high. The field is picked to be large enough to have enough sample variance, but small enough to be within the minimal foreground patch of sky.

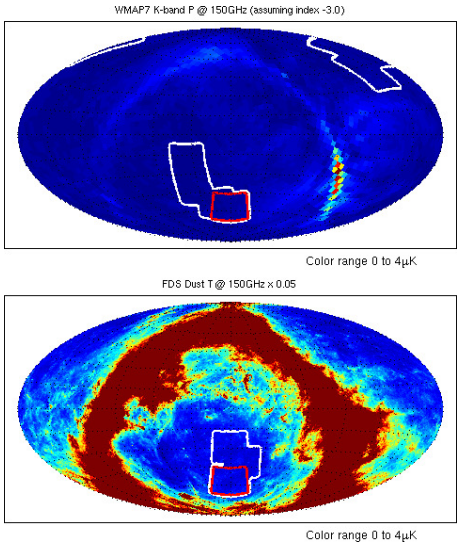

Figure 2.7: Left: WMAP K-band map scaled to 150GHz assuming a spectral index of -3.0. Right: FDS Model 8 dust map at 150GHz, assuming a polarization fraction of 5%. The white lines outline low foreground regions, the red line outlines the "Southern Hole" region that BICEP2 and Keck Array observes. *Figure from* BICEP*2/Keck Array Collaboration.*

2.6.1 Foregrounds projections

The "Southern Hole" is expected to be one of the cleanest patches of sky as it is away from the plane of the galaxy. Synchrotron emission (polarized emission from the radial acceleration of electrons in the galactic magnetic field), has a frequency emission spectrum that is characterized by a power law with $\beta_{sync} \approx -3$ [10], and is therefore bright at lower frequencies. The upper figure in Figure 2.7 shows the WMAP K-band polarized intensity map extrapolated to 150GHz. A fraction of thermal dust emission is expected to be polarized due to the spinning dust grains in the galactic magnetic field. The frequency of dust emission is expected to have power law with $\beta_{dust} \approx 1.41$ [10]. The bottom of Figure 2.7 shows the FDS[28] dust intensity map extrapolated to 150GHz, and given a 5% polarization fraction.

2.6.2 Observing Site

The observing patch is visible from the South Pole, which has a long history of CMB observations [43]. The South Pole is high in elevation and cold and so the atmosphere is rather dry, allowing for excellent observations in the microwave [17]. The atmosphere at the South Pole is stable, particularly during the winter months when most of the science observing is done. The Amundsen-Scott South Pole Station has a support structure in place to allow year-round observations.

From the South Pole, the observing patch is at a constant elevation of $\sim 50^{\circ}$ (the sky does not rotate but spins around), allowing us to raster at constant elevation scans. The observing patch is available all year, and visible at any time of the day, allowing for continuous observing for as much time as possible, maximizing the sensitivity for this observing patch.

Chapter 3

The Keck Array Optics

THE BICEP2 AND KECK ARRAY optical system follows the BICEP1 optical design, using a straightforward, on-axis refracting telescope in order to ensure the most sensitive, systematics-free instrument to detect degree-scale B-mode polarization. Figure 3.1 shows a cutout of a single Keck Array receiver. The optical elements for BICEP2 and the Keck Array consists of a vacuum window, infrared blocking filters at the 50K and 4K cryogenic stages and the lenses held in the telescope tube. In this chapter, we discuss the principles behind the design and the manufacture of each element in the optical system of the BICEP2 and Keck Array experiments.

BICEP1, BICEP2, and Keck Array were designed in order to try to detect the B-mode polarization at degree angular scales. As such, the resolution of the telescope system was chosen to have the minimum resolution needed in order to find the B-mode signal that peaks at degree angular scales. The BICEP2 and Keck Array telescopes were designed to have a resolution of $\sim 0.5^{\circ}$ which only requires a diffraction limited aperture of ~ 26cm.

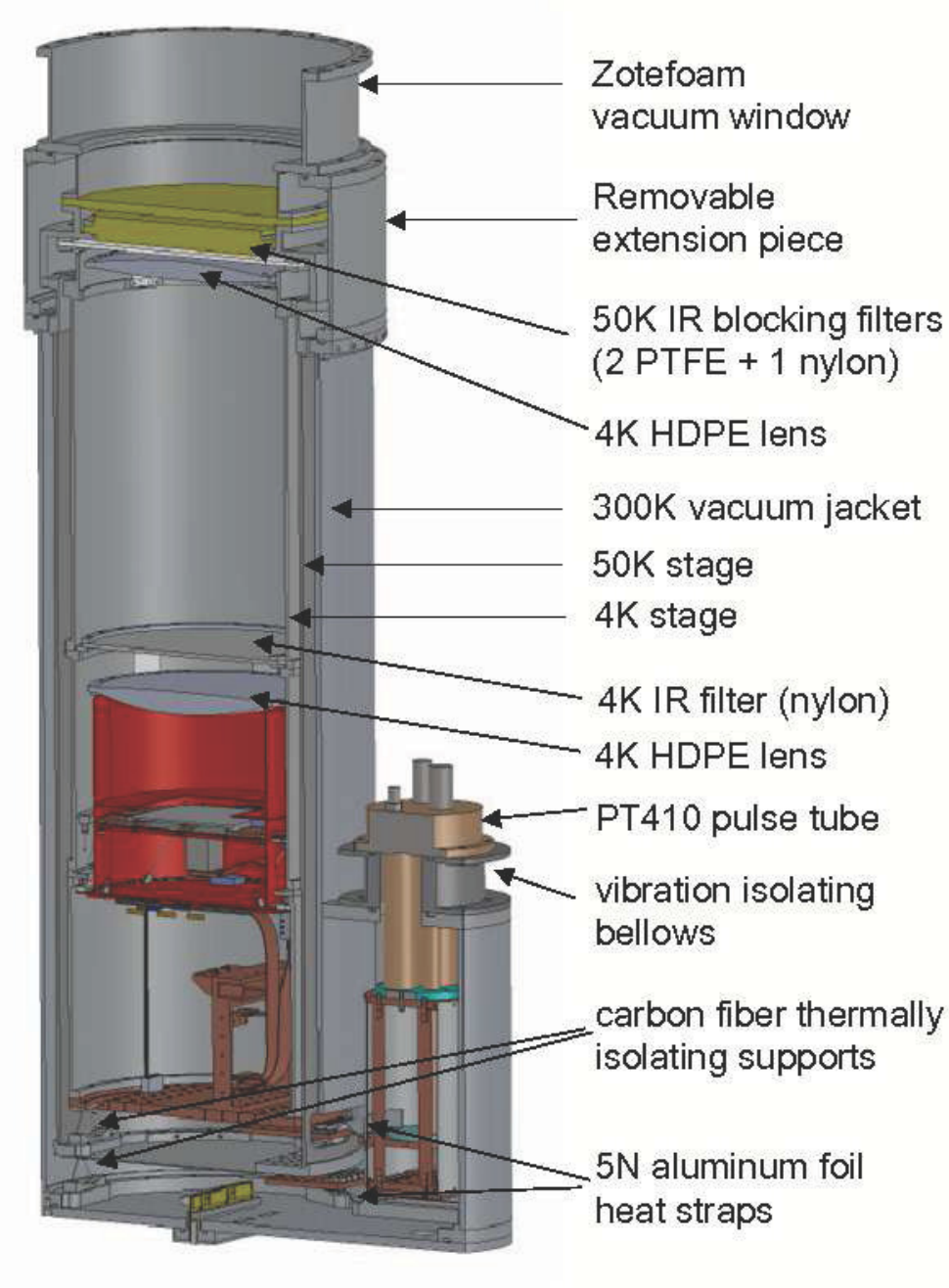

Figure 3.1: A cutout showing the placement of all the optical elements in each Keck Array receiver. The vacuum window seals the cryostat while letting in radiation. Infrared blocking filters on the 4K and 50K stages reduce the loading on the detectors and sub-Kelvin stages. The two-lens telescope focuses light using a telecentric optical design onto the focal plane. *Figure from [61].*

This results in a physically small optical system, which has many advantages. The entire system can be rotated around the boresight, which allows us to modulate the incoming polarization and measure both Q and U Stokes parameters without requiring another method of polarization modulation such as a waveplate. (The sky does not rotate at the South Pole, and we scan using constant elevation rasters, thus requiring an additional method to measure both Q and U.) The boresight rotation also helps reduce certain classes of systematics in the telescope [24].

Detecting B-mode polarization at degree angular scales also requires unprecedented sensitivity. A small optical system allows many of the optical elements to be held at low temperatures. For BICEP2 and Keck Array, both lenses in the refracting telescope are held at 4K, leaving only some infrared absorption filters to be held at 50K. The cold optical system minimizes the optical loading due to the emissivity of the optical elements onto the detectors, thus increasing their sensitivity. Nearly all optical elements except the window are anti-reflective coated to maximize the amount of transmitted radiation. The BICEP2 and Keck Array use a telecentric optical design in order to maximize the number of detectors in the telescope, thus increasing the sensitivity of the telescope, while at the same time minimizing the aberrations of the beams in the far field. Aberrant beam effects, such as a possible birefringent effect caused by stresses in the optical material, can cause temperature-to-polarization leakage and obscure the signal that we are trying to find, thus reducing the advantage our sensitivity gets us. Much care is taken in the design and manufacture of the optical elements to minimize as many possible aberrant beam effects that can be induced by imperfect optics.

3.1 Windows

As light enters the telescope, the vacuum window is the first optical element encountered. The vacuum window is part of the cryostat seal, and as such, has to be strong enough to withstand atmospheric pressure for long periods of time (at least an observing season of 9 months), but also be transparent to microwaves. Since we use a small optical design, we only need a clear aperture of 12.5 inches. This is small enough to allow us to use a foam window instead of something more sturdy such as a plastic window. A foam window reflects much less radiation and does not need to be anti-reflective coated. However, the atmospheric pressure onto the foam window is large, requiring multiple layers of foam to be laminated into a single piece in order to withstand the pressure on the window.

The windows for BICEP2 were made using 4 layers (for a height of $\sim$ 5 inches) of Zotefoam[1] PPA30, a closed-cell nitrogen-expanded polypropylene foam that had been heat laminated by Technifab[2]. The foam was glued onto an aluminum window frame in stages using Stycast 1266. In order to increase the adhesion of the foam to the epoxy, we vacuum de-air the epoxy after mixing, as well as once the epoxy has been injected into the space between the aluminum and foam (called in-situ degassing). For BICEP2, we used a two-cylinder acrylic jig to pull a vacuum on the space between the foam and the window frame walls. The in-situ degassing process allowed air bubbles created by the injection of epoxy as well as air bubbles created around the edge of the foam to be removed, resulting in a stronger adhesion of epoxy to foam. The inner walls of the BICEP2 window frame was also roughened with a file in order to increase the surface area and improve adhesion of

[1] http://www.zotefoams.com/

[2] http://www.technifabinc.com

Stycast 1266 to the wall of the frame.

The Keck Array windows are made using a different foam, Zotefoam HD30 instead of Zotefoam PPA30 since Zotefoam had stopped production of PPA30. The Keck Array windows are made from 4 layers of laminated Zotefoam HD30, a nitrogen-expanded polyethylene foam, glued with Stycast 2850.

Technifab heat-laminates the entire bun (40"x71") of foam after the skins have been cut off. In order to have the sturdiest window possible with the least number of laminated layers, we ask Technifab to minimally remove the skins. One surface of each layer of the foam to be laminated is heated and the foam is then pressed together in a roller. This is done layer by layer. For HD30, we have found that if they laminate an entire bun of 1 inch thick foam together, there tends to be delaminations in the middle, where the heat-lamination does not work. We have gotten around this by asking Technifab to cut the buns to smaller pieces, then laminating the smaller pieces together. This means less yield for each bun of foam, but also less likely for delaminations in the middle of the bun. The laminated bun is then waterjet cut into 15.8 inch diameter pucks, which are then shipped to us. Unless the waterjet cuts completely through one of the delaminated parts, we are unable to tell whether or not the window foam has delaminated pockets. Only once the window construction is finished and we vacuum test it can we see it. The delaminated pockets cause additional bulging in the foam from the pressure of the air trapped in it.

We switched from using Stycast 1266 to Stycast 2850 because, unlike for BICEP2, the Keck Array windows do not sit completely indoors and are therefore not adequately warmed. The differential thermal contraction between the aluminum window frame and Stycast 1266 causes the epoxy to tear away from the window frame. We do find that Stycast

2850 does not adhere quite as well to the window foam, and so the main failure mode of the Keck Array windows are a tear between the foam and the epoxy. We poked holes in the foam to improve adhesion. The holes in the foam are made with the length of a heated soldering iron (0.625 inches). The holes begin a quarter of an inch from the top, and are spaced apart by approximately the diameter of the soldering iron. As we move downwards, the holes are spaced wider apart (approximately 1 to 1.5 inches). The strongest forces on the window are at the top of the foam, and the closely spaced holes are meant to help hold the foam to the window frame and minimize bowing or tearing.

When making Keck Array windows, we perform in-situ degassing by placing the entire window, once the epoxy has been applied, in a large vacuum chamber. This helps remove air bubbles in the epoxy, and also helps fill in the holes in the foam with epoxy. Substantial care is taken to keep the epoxy from marring the surface of the window.

Once a vacuum window has been made, it is then placed onto a transparent acrylic cylinder and leak-checked. The transparent acrylic cylinder also allows for measurements of the amount of bowing of the bottom of the foam. Four layers of laminated HD30 is found to bow ~ 1 inches (measured from the surface of the foam).

The radiation loss in the foam window is dominated by the scattering off the lamination. Rough measurements of the foam transmission have been taken using the broad spectrum microwave source in lab settings, using either BICEP2 itself or a detector diode. Four layers of Technifab-laminated PPA30 is measured to have a transmission loss of $\sim 2\%$, while four layers of unlaminated PPA30 (held together simply by hand), is measured to have a transmission loss of $\sim 0.4\%$. The transmission loss of unlaminated HD30 is measured to be approximately the same ($\sim 0.2\%$), but the transmission loss of laminated HD30 has

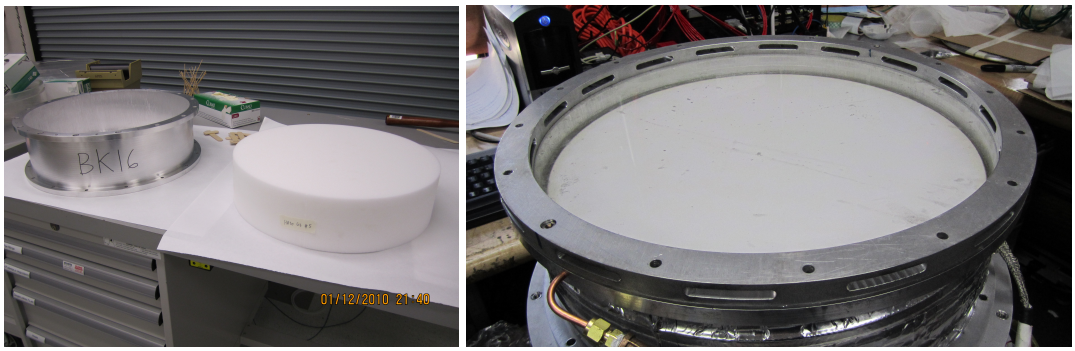

Figure 3.2: Left: An empty window frame and window foam. Right: A completed vacuum window. The vacuum window has to be strong enough to withstand atmospheric pressure while allowing radiation to pass through. The small aperture design of BICEP2 and the Keck Array allows the use of foam as the vacuum window. The Keck Array and BICEP2 windows are made from Zotefoam HD30 and Zotefoam PPA30 respectively.

not been well quantified. A simple insertion test of the transmission loss of HD30 does not give satisfying results, as inserting the sample increases the signal of the received radiation. This seems to indicate slightly increased scattering in HD30 compared to PPA30.

For BICEP2, we explored the possibility of constructing unlaminated multi-layered foam windows [18], in order to try to increase the transmission of the window. The lack of lamination of the foam, however, caused the foam layers to start peeling away from each other once under vacuum, resulting in a less robust structure unable to withstand atmospheric pressure.

3.2 Infrared Blocking Filters

The infrared blocking filters are used to reduce the infrared loading onto the 4K and sub-Kelvin stages. Without the infrared filters, the infrared loading from the sky would overwhelm the cooling power of the 4K stage of the cryocooler,and disallow the detectors

from getting on the superconducting transition. However, the infrared filters have to be highly transmissive in the microwave, so that we do not limit the sensitivity of the telescope. In BICEP2 and the Keck Array, we mainly use absorptive filters in order to reduce infrared loading. We also use a reflective filter at the 4K stage to introduce a steep frequency cutoff in order to reduce out-of-band radiation from reaching the detectors.

Absorptive filters work by capitalizing on the transmission spectrum of appropriate materials. We choose materials that are transmissive in the microwave, but rapidly become absorptive at higher frequencies, particularly in the infrared. Infrared absorption heats up the filter, however, and causes the filter to reradiate, which increases the in-band loading, resulting in the reduced sensitivity of the detectors. To counteract this, the absorptive filter has to be designed such that the heat absorbed by the filter is conducted away efficiently to the cooling stages.

We use multiple stages of infrared filtering. The Keck Array has three absorptive filters at the 50K stage in each receiver. The IR filters consists of two Polytetrafluoroethylene (PTFE) filters that are 0.5" and 1.35" thick, and one 3mm thick nylon filter. PTFE is transparent in the microwave, but becomes absorptive in the infrared [68]. The loss tangent of PTFE at 100GHz is 3×10^{-4} at 100GHz and 6.8×10^{-4} at 400GHz [46]. We include very thin nylon in our IR blocking scheme because nylon has a steeper frequency cutoff allowing us to prevent more infrared radiation from reaching the detectors. The loss tangent of nylon at 100GHz and 300K is 8×10^{-4} but steeply rises to 16×10^{-4} at 300GHz [46]. Nylon is very absorptive in the microwave at room temperature but transmissive at low temperatures. However, nylon has a lower thermal conductivity than PTFE when cold (nylon's thermal conductivity at 4K is 0.012 W/m·K, while PTFE's thermal conductivity at 4K is 0.046

W/m·K [23]) and so the in-band loading induced by the nylon would be larger if we used thicker pieces of nylon as filters. At the 4K stage, we place a 5.2mm thick nylon filter between the eyepiece and objective lens. Clamped onto this lens is a metal-mesh low-pass filter [3]. The infrared blocking system in BICEP2 is exactly the same at the 4K stage, but uses a single 1 inch PTFE filter at 100K and a second 1 inch PTFE filter and one 3mm nylon filter at 40K (since the cooling system in BICEP2 is different). The BICEP2 metal-mesh low-pass filter has a cutoff at 8.3cm^{-1}, however, the Keck Array metal-mesh low-pass filters have a cutoff at 8.5cm^{-1}. The metal-mesh low-pass filters are produced at the University of Cardiff, and coated with an anti-reflective layer before use. The metal-mesh filters were included in order to reduce the out-of-band radiation coupling to the detectors, and not primarily to reduce the loading on the focal plane.

Infrared loading from the sky is expected to be $\sim$35W, and the IR filtering design reduces the incoming loading from 35W to a few μW of loading on the detectors. The thermal modeling is taken from Jamie Bock's spreadsheet. Some of the incoming infrared radiation is absorbed by the window, which then reemits since the temperature of the bottom window foam is $\sim$260K. The amount of loading onto the 50K stage is estimated to be $\sim$20W. The bulk of the incoming loading is absorbed by the first PTFE filter which, for Keck Array is a 0.5" thick. Its thickness is chosen in order to efficiently disperse the absorbed infrared radiation onto the cooling stage while keeping the equilibrium temperature at $\sim$130K. Directly under this stage is a 1.3" PTFE filter designed to absorb the $\sim$2W of power that is reemitted by the 0.5" thick filter. Less infrared radiation is directed at this and as such it can be thicker in order to absorb more infrared radiation while still maintaining a low equilibrium temperature of $\sim$75K. The last stage of infrared filtering on the 50K stage is

a 3mm thick nylon filter. The resulting infrared loading onto the 4K stage is expected to be 30-50mW. This matches the measured optical loading onto the 4K stage (measured by a macrobolometer on the objective lens) of $\sim$90mW. The lenses and the 4K nylon filter is estimated to reduce the infrared loading to $\sim$4 μK, which also agrees with measured optical loading onto the niobium spitoon of $\sim$6 μK.

In order to reduce the in-band emission of the absorptive filters, the absorptive filter are heat-sunk to the 50K stage using aluminum clamping rings. Since the entire system is cooled to 50K or 4K, what matters is the clamping force on the filters when the system is cold. A higher clamping force increases the thermal conduction between the filter and the cooling stage, and allows heat to be dissipated more efficiently, reducing the amount of in-band emission. The thermal expansion coefficient for the PTFE (1.86% from 300K to 4.2K) and nylon (1.32% from 300K to 4.2K) filters are different from the thermal expansion of the filter holder ring, which is made of aluminum(0.415%) [23]. Therefore, slots have been made instead of holes in order to allow the filters to contract more when cold. The differential thermal expansion also means that when cold, the clamping force onto the filters will change. In order to counteract that, we use stacked belleville washers that we expect will take up the slack when the filter assembly is cold to ensure that the clamping force is constant on the filters.

Manufacturing the plastic filters start with buying appropriate plastic material. Care was taken when choosing the plastic needed to make the optical elements for BICEP2 and Keck Array. We take care to use cast or compression molded materials, as there are suspected birefringent effects in extruded materials. We used compression-molded PTFE sheets from Scientific Commodities, which sources their PTFE sheets from Interplast. We previously

bought PTFE sheets manufactured by FloroPlastics, and Industrial Plastics, but optical tests seem to indicate that these PTFE sheets induce birefringence effects. We purchased Cast Nylon 6 from Nycast to use for making the nylon filters. Nycast uses Accurate Plastics as their vendor.

The PTFE material is also annealed before machining. We anneal PTFE in order to ensure that the plastic does not move during the machining process. We also anti-reflective coat the filters using a heating process (described in Section 3.4), and the annealing mimics this process and ensures that the PTFE does not change its shape during the coating process. The material is placed onto a metal surface that has been machined flat and placed in a 60°C oven for an hour to equilibrate. The oven is then heated at 0.2°/minute to a temperature of 140°C. The temperature is held at 140°C for 10 hours in order to allow the plastic to release internal stresses, and then cooled slowly at 0.2°/minute until it reaches a temperature of 40°C, whereupon it was allowed to cool rapidly to room temperature. The slow rise and fall in temperature is to allow the entire plastic slab to warm and cool uniformly to avoid inducing heating/cooling stresses within the plastic. We find that the PTFE does change its shape very slightly after the first annealing stage. We find that cast nylon seems to be very dimensionally stable and does not need to be annealed at all.

An important aspect of the filter, once machined, is to have both surfaces lie parallel to each other, so as to not be a lens. We use a vacuum jig that holds the filters flat against it when machined in order to ensure that both surfaces are parallel to each other. Since the refractive index of PTFE is 1.44 while the refractive index of nylon is 1.72, there is a risk that if the surfaces of the filters are not parallel, the filters can act like lenses, thus throwing the telescope out of focus. To ensure that the front and back surface of each filter is parallel

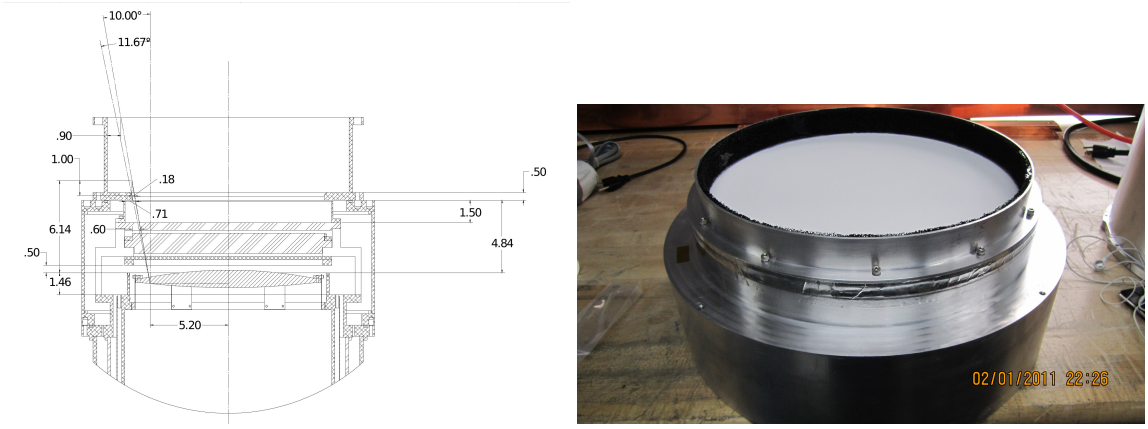

Figure 3.3: Left: A cutout of the 50K filter stack assembly on the left, illustrating the multi-layered absorptive filters used in the Keck Array, and the clearances between various parts in inches. The figure shows that there is an angle of 11.67° that allows the edge pixels that are at most 9.1° from the boresight to have a clean line of sight to the sky. *Figure by Chris Sheehy*. Right: A photograph of the completed filter stack. We use absorptive filters in order to reduce the incident loading onto the 4K and sub-Kelvin stages.

to each other, once one side has been machined flat, the filters are placed on a flat jig on which vacuum pressure is pulled, ensuring that the other side of filter remains parallel to the first side. The plastic is flipped back and forth over several iterations. In order to ensure that the PTFE and nylon do not absorb contaminants we do not use any coolants when machining the filters, and, as such, the machining has to be performed slowly using large mill bits in order to ensure no heating and no stressing of the plastic. The filters are all anti-reflective coated to reduce reflections off their surfaces as detailed in Section 3.4.

3.3 Lenses

The BICEP2 and Keck Array telescope design is an on-axis, two-lens refractor [4, 25]. The The B-mode polarization power spectrum is expected to peak at ℓ $\sim$100, at degree

Figure 3.4: Left: An anti-reflection coated 50K nylon filter. Right: A view of the slots machined into the 4K nylon filter. We machine slots instead of holes to account for the differential thermal coefficient between the plastic filters and the aluminum clamping rings, allowing the filter to slide freely when the system becomes cold.

scales, and so the Keck and BICEP2 optics, like the BICEP1 optics, uses the smallest aperture necessary to resolve this peak [68]. The BICEP2 and Keck Array optics are diffraction limited, and are designed with an aperture of 26.4 cm and, thus, a beam width, σ, of $\sim 0.22^{\circ}$.

The two-lens telecentric design was chosen to accommodate the flatness of the focal plane, and to minimize the beam distortions of the edge pixels in the far field, while maximizing the number of detectors that can be placed on the focal plane. Figure 3.5 illustrates the telecentric optical design of the BICEP2 and Keck Array telescope. The lens design was optimized for BICEP2 [4, 5] using Zemax simulations. A thorough discussion can be found in [4]. Here I present a summary. The BICEP2 and Keck Array telescopes have an objective and an eyepiece lens. The aperture is defined to be coincident at the objective lens, in order to enforce telecentricity of the optics design. First the focal length of the optical elements were defined for a plate scale of $\sim$0.1°/mm, a plate scale that was chosen to tile the beams on the sky at distances approximately corresponding to the physical pixel separation. Then, the lens curvature was optimized using two models: a time forward model in which the ob-

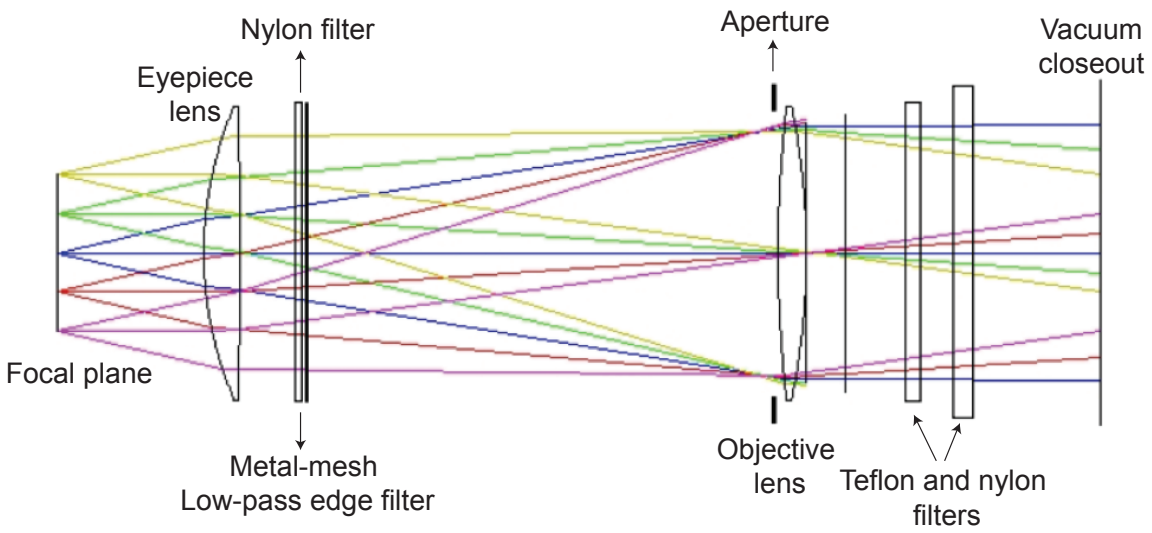

Figure 3.5: A schematic of the BICEP2/Keck Array optical chain. We use a two-lens telecentric design that allows for high throughput while minimizing the beam distortions in the far field. Infrared blocking filters in the optical chain reduce the loading on the cooling stages. *Figure from [4].*

jective lens was optimized to minimize aberrations in the focal plane, and a time reverse model in which the eyepiece lens was optimized to enforce telecentricity and to minimize aberrations in the aperture plane [4, 5]. The optical design results in a tiling of the beams in a square grid with sides that are $\sim$16 degrees across.

The lenses are manufactured out of high-density polyethylene (HDPE) which is highly transparent in the microwave (A loss tangent of 3.1×10^{-4} at 150GHz) [46]. HDPE has an index of refraction of 1.52 [46]. The advantage of using plastic is that the lenses are easily machinable, enabling us to use the same AR coating process that we used for the filters. We use compression-molded HDPE from Polymer Industries. The HDPE is machined into the shape of the lenses at the CfA machine shop. Figure 3.6 shows a slab of HDPE being machined on the lathe, and a completed and anti-reflective coated objective lens. The requested machining tolerance is $\pm$0.003" on the surface shape, and a smoothness of

0.001" on the tooling marks.

We anneal the material in a process similar to the PTFE annealing process as described in Section 3.2 before machining begins in order to relieve the stresses in the material and to ensure that the piece does not change shape during the machining. The annealing process for HDPE only raises the temperature of the HDPE to 124°C, as the HDPE has a melting point of 128°C. We repeat the annealing step once the lens has been rough cut leaving 0.1" of material on the final shape of the lens. The intermediate annealing step is performed using a circular jig that holds the flanges of the lens flat. While we do notice that the first annealing stage changes the shape of the HDPE slab by $\sim 2\%$ in length, we don't really notice any changes in the shape of the HDPE after that. However, the second annealing stage does try to relieve the stresses from machining. The lenses are annealed a final time when we anti-reflective coat them. The machining is done without any coolants (in order to avoid contamination of the material) and so the material is vulnerable to being heated up. The annealing process is important to ensure that the lenses are not warped and do not introduce aberrant optical effects.

The objective and eyepiece lenses are held along the same axis using lens flexures attached to an aluminum telescope tube. The temperature of the optics directly impacts the amount of loading on the detectors. We therefore would like to keep the lenses as cold as possible in order to allow the optics to have stable and low loading on the detectors. BICEP2's lens flexures were made of copper in order to allow better thermal conduction between the lenses and the walls of the telescope tube. However, the differential thermal contraction between HDPE (lenses) and aluminum (telescope tube) is substantial. As we cool from room temperature to 4K, HDPE contracts by 2% [23], while aluminum contracts

Figure 3.6: Left: A slab of high-density polyethylene (HDPE) on a lathe as it is being machined. *Photograph by John Kovac*. Right: An anti-reflection coated eyepiece lens. The HDPE is annealed before machining to remove stresses and machined without using coolants to prevent contamination of the material.

by 0.415% [23]. For Keck Array we wanted to ensure that the lenses were not being stressed when cooled. The lens flexure system is designed such that the lenses are able to contract more than the aluminum when cold, but also contract in such a way that it is still centered. A miscentering of the lenses can cause beam distortions for many detectors. Figure 3.7 show the design of the lens flexures. The flexures have hinges at the top and the bottom in order to allow flexibility in the radial direction. The lens flexures are rigid in the direction tangent to the tube in order to hold the lenses concentric within the tube. The aluminum lens flexures for Keck Array are thicker in the center compared to the copper lens flexures used for BICEP2 to compensate for the lower thermal conductivity of aluminum.

We also attempt to increase thermal conduction between the top and the bottom of the telescope tube using a set of 6 copper bars that run along the sides of the telescope tube. These bars are bolted to the bottom of the tube, as well as to the points at which the lenses are mounted.

To prevent stray reflections from hitting the sides of the telescope tube, the telescope

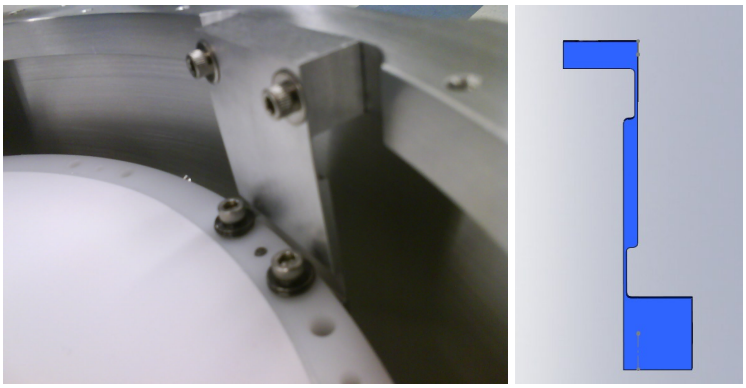

Figure 3.7: Lens Flexures. Left: A view of one of the six aluminum lens flexures installed on the eyepiece lens. Right: A model of the lens flexures. The lens flexures are flexible in the radial direction to allow the lenses to contract freely radially when cold, but rigid in the tangential direction.

Figure 3.8: Left: A view of the inside of the blackened telescope tube, with the objective lens and the aperture stop visible. Right: An assembled telescope tube with copper bars on the sides to increase thermal conduction from the bottom to the top.

tube is blackened with carbon-loaded HR10 glued onto the inside of the tube with Stycast 2850. For high angles of incidence, the measured reflectance of carbon-loaded HR10 on an aluminum sheet is $\sim$1.5-2%. However, we did not consider shallow incidence reflectance, which turned out to be slightly higher. We discovered this after mapping the far sidelobes for Keck Array and found ring-like structures that correspond perhaps to the four-sided detector lobes reflecting off the inside of the telescope tube and making its way onto the sky. In order to resolve this issue, additional baffling was installed inside the telescope tube in December 2013.

3.3.1 Romer Arm Measurements

We perform a check on the shape of the lenses by comparing the shape of the lenses to a model using a Romer Arm[3].

First we align the flat flanges of the lenses (where we mount the lenses) to the flanges of the model. Then, we record the deviation of the shape of the lens from the model. Measurements of each of the lenses are made after machining, after AR coating, and after the lenses have been assembled into the telescope tube. After machining, the deviation of the surface of the lens from the model has been found to be accurate to 0.2 ± 0.2mm. When comparing the AR coated lenses to the model, we have to take into account the additional ~ 0.4 mm thickness of the AR coating on the lens shape. Deviations from the shape of the lenses after AR coating has been measured to be the same (0.2 ± 0.1 mm). Interestingly, the entire lens surface after AR coating seems to have been raised 0.4 ± 0.2 mm on the curvier side of the lens compared to the rim of the lens; however, the shape of the lens itself

[3] www.romer.com

does not seem to be affected. While 0.2 mm exceeds the requirements we requested for the surface accuracy, we have found that the telescopes still seem to be in focus.

Measurements of the placement of the lens in the telescope tube assembly was also made to ensure that the telescope was in focus. Since the telescope tube is rather large, the alignment and consistency of the measurements are more difficult to get right. On the whole, we find that the placement of the lens from the top of the tube is accurate to 0.2 ± 0.2mm. The lens looks to be placed levelly to 0.2 mm as well.

3.3.2 Aperture Stop

In the BICEP2 and Keck Array optical system, the aperture is defined to be coincident with the objective lens. BICEP2 and the Keck Array telescopes use a "soft" aperture made from absorber and tapered to an edge to prevent ringing caused by a hard aperture [4]. The average amount of power expected to be truncated at the aperture stop for a pixel is $\sim 20\% \pm 1\%$ [4].

The aperture stop is 264mm in diameter and is cut with a 40deg taper using a scroll saw, which is then glued onto the bottom of the objective lens. The aperture stop is made from Eccosorb[4] AN74, an absorber that was chosen because of its thickness and density. While Eccosorb HR-10 is more often used as an absorber for higher frequencies, it is difficult to cut HR10 into a specific shape, whereas AN74 holds its shape easily and does not disintegrate as easily as HR10 does. The aperture stop is glued onto the lens with Stycast 1266. There is also a stop placed above the top of the objective lens to prevent stray reflections from making it into the telescope tube. This stop is made from Eccosorb AN73

[4] www.eccosorb.com

Figure 3.9: Aperture Stop. The aperture stop is made from Eccosorb AN74 with a 40 degree taper and glued onto the bottom of the objective lens. A second stop to prevent stray reflections is glued onto the top of the lens. The power truncated on the aperture is designed to be $\sim$20%.

and has an inner diameter of 274mm. AN72 and AN73 has about a $\sim$2% reflectance at 100GHz source.

3.4 Anti-reflective coating

We anti-reflective coat nearly all the optical elements in BICEP2 and Keck Array receivers in order to maximize the sensitivity of the telescope, as well as reduce stray reflections off the surfaces of the optical elements. The throughput of the telescope plays a large role in the sensitivity of the detectors. We would like to reduce the amount of radiation reflecting off each optical element's surface in order to increase the amount of radiation collected onto the detectors. The reflections off the lenses and filters can also cause ghost beams that can contaminate the polarization signal we are seeing. All the lenses and filters are coated with anti-reflective coating in order to reduce the intensity of the ghost reflections as well as to increase the sensitivity of the detectors.

Anti-reflective coating works by applying a layer of material that has index of refraction

$\sqrt{n}$ and a thickness of $\lambda_{\sqrt{n}}/4$ onto a material with an index of refraction n [31]. This way, the light that is reflected off the material interferes destructively with the light that is reflected off the anti-reflective coating, reducing the total amount of reflected light and increasing the transmittance through a material. Single layer anti-reflective coatings are optimized for a specific frequency. BICEP2 and each receiver in the Keck Array have been designed for a single frequency band, allowing us to optimize the anti-reflective coating for BICEP2 and Keck Array for a center frequency of 150GHz.

The anti-reflective coating we use is an expanded porous PTFE sheet manufactured by Porex[5]. Given the filling factor of a sheet of porous PTFE, we can calculate the expected index of refraction using Equation 3.1.

$$\text{Filling factor} = \frac{\text{Density of Porous PTFE}}{\text{Density of PTFE}} = \frac{\text{n}_{\text{porous PTFE}} - 1}{\text{n}_{\text{PTFE}} - 1} \tag{3.1}$$

The index of refraction of PTFE, n_{PTFE} is 1.44, and the density of Teflon = 2.2 g/cm3. We calculate the expected index of refraction for standard porous PTFE sheets manufactured by Porex, and purchase materials cut to the required thickness.

The index of refraction of HDPE is 1.52 [46], and therefore the most effective index of refraction of the AR layer is 1.23. For the AR layer we use Porex PM23DR that has a filling fraction of $\sim 57\%$(density of 1.25 g/cm^3) and therefore an index of refraction 1.25, which is the closest we can obtain from the available products. Since the index of refraction of PTFE is 1.44 [46], and the most effective AR layer for PTFE would have an index of 1.2, we use the same material, PM23DR, to AR coat our PTFE filters. For 150GHz, $\lambda_{\sqrt{n}}/4$ is 0.016", and the material has been cut with a tolerance of 0.001" thickness.

[5] www.porex.com

The index of refraction of nylon is 1.72 [46], and so the most effective index for the AR layer is 1.31. We use a denser material as an AR coat for nylon, PM23JR, that has a filling fraction of $\sim 74\%$ (density of 1.62g/cm^3) and an expected index of refraction of 1.33. The material thickness is 0.015" for 150GHz.

In order to adhere the anti-reflective coating onto the lenses and the filters, we heat bond the expanded PTFE onto the lenses and filters with 0.002" thick low-density polyethylene (LDPE). To ensure uniform pressure on all surfaces that is being AR coated, we use atmospheric pressure to facilitate uniform adhesion on all parts of the optical surfaces using a vacuum bagging system. LDPE is sandwiched between the AR coating material and plastic surface and the entire setup is placed on an appropriate metal jig that either accommodates the curvature of the lens or the flatness of the filters. A silicone bag is placed onto the jig and clamped into place with a metal ring. Vacuum pressure is pulled and the entire system is placed into an oven. Figure 3.10 shows the anti-reflective coating setup.

The AR coating heating cycle is designed to be similar to the annealing cycle. The oven is heated up at 0.2°C/minute until it reaches a soak temperature to ensure uniform heat throughout the entire plastic piece. The melting temperature of LDPE is $\sim$120°C, and so we hold the lenses at 124°C, just hot enough to melt LDPE, but not hot enough to melt the lenses. Teflon and nylon have higher melting temperatures, and so we AR coat PTFE at 140°C and nylon at 130°C. The plastic is held at the soak temperature for a period of 10 hours in order to allow the LDPE to gradually melt and adhere to both the plastic as well as to the porous PTFE. Once the soak time is over, the temperature of the oven is slowly ramped down at 0.2°C/minute until room temperature to allow uniform cooling of the lenses or filters to avoid stressing the material and to allow the adhesion to hold.

Figure 3.10: The anti-reflective layer of porous PTFE is heat-bonded onto the surface of the optical element using low-density polyethylene as glue. The plastic is vacuum-bagged during the process to ensure uniform pressure on the entire surface.

On the whole, the adhesion works very well. The lenses particularly have had no delamination problems. It helps that the LDPE and HDPE are closely related, and that there are visible grooves on the lenses as a result of the machining process that helps adhere the anti-reflective coating onto the lenses.

We have had, however, problems with adhesion on the nylon and PTFE filters. Once the filters had been through a thermal cycle and been cooled to 50K within the cryostat, the anti-reflective coating adhesion would occasionally peel off. As a result, we have scored the nylon using Scotch-Brite, and PTFE using 180-grit sandpaper in order to improve the adhesion. The improved adhesion was tested by dunk testing coated test pieces of nylon and PTFE in a liquid nitrogen bath.

Chapter 4

Beam Characterization

THE BEAM OF THE TELESCOPE describes the angular response of detectors on the sky. The beam modulates the signal that each detector sees and, as such, we would like to fully understand the characteristics of the beam shapes for every detector in the telescope.

We start by mapping the near-field beam shapes by placing a chopped heat source very close to the aperture of the telescope. Studying the details and imperfections of the near field beam response will allow us to understand the detectors' response at the beginning of the optical chain.

Understanding the detectors' response on the sky, however, requires us to map the detectors in the far-field. We take advantage of BICEP2's and the Keck Array's large angular resolution of half a degree and therefore relatively close far field ($\sim$ 70 m) to fully map out the far field beam response for every single detector in our telescope. We then fit each detector's beam as a two-dimensional elliptical Gaussian and extract beam parameters for each of the 512 detectors in BICEP2, and 2560 detectors in the Keck Array.

In this chapter, we will discuss briefly the near field beam measurements and the effects of beam steer on the optical efficiency. We detail the far field beam map measurements and the parameterization of the BICEP2 and Keck Array beams. Finally, we close with a short description of the sidelobe measurements, the ghost beams and polarization angle calibrations.

4.1 Near Field Beam Characterization

In order to understand the shape and characteristics of the beam illumination of the aperture, we map the response of the detectors in the near field. The near field beam response maps the phase of the electric field in the focal plane and is a probe of the beam vignetting.

We place a heated ceramic source on an x-y stage which is then hoisted into place above the receiver. The source is placed as closely as possible to the aperture, which, for BICEP2 and Keck, is directly above the window. Ideally, we would place the source at the plane of the aperture in order capture the response of the detectors without the influence of the optical chain. The source is moved in a raster across a 12 inch by 12 inch scan throw in 0.25 inch steps.

The near field beam maps for BICEP2 were taken during two summer calibration seasons. For each Keck Array receiver, near field beam maps are taken as soon as an assembled receiver is cooled down successfully, as a first check on the optical performance of the receivers. (We have found peeling aluminum tape inside the receivers as a result of seeing aberrant near field beam maps.) The near field beam maps are taken using the detector's aluminum transition which allows for higher loading conditions in lab.

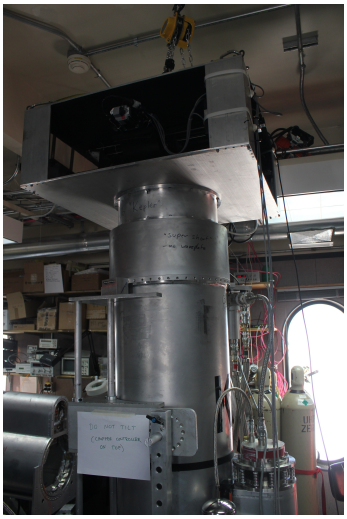

Figure 4.1: Near field beam mapping setup at Pole. A heated ceramic source is placed as closely as possible to the aperture, and rastered back and forth in order to form a map of the near field beam response. *Photograph by Jamie Tolan*.

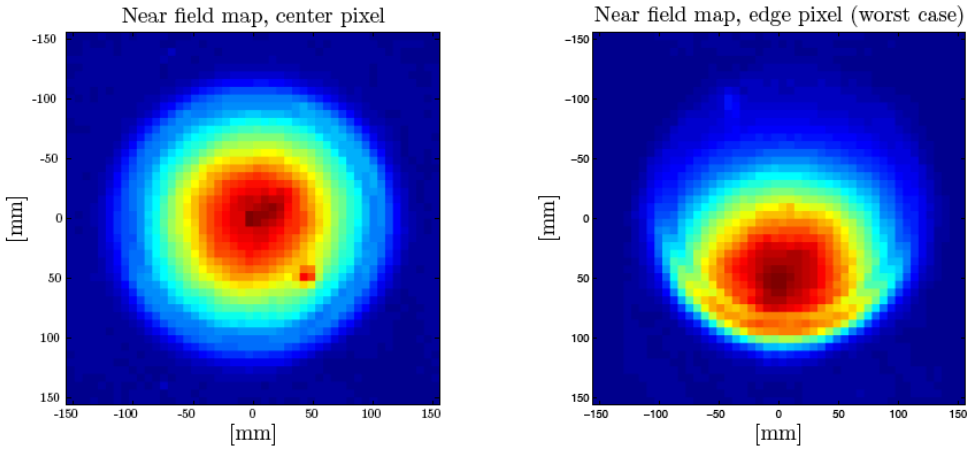

Figure 4.2: Left: An example of the near field beam map of a detector close to the center of the focal plane. Right: A near field map of a detector close to the edge of the focal plane. Both maps display example near field maps for BICEP2. The beam steer effect (described in Section 4.1.1) results in a non-centered illumination of the aperture, truncating the beam and causing the beam to have higher ellipticities in the far field. *Figure from [25].*

The resulting map can be seen in Figure 4.2. The figure on the left shows the near field beam map of a typical pixel close to the center of the focal plane. The figure on the right shows the near field beam response of a pixel that is closer to the edge of the focal plane.

4.1.1 Beam Steer

In Figure 4.2, we show that the detectors closer to the edge of the focal plane show a beam steer effect, where the beam of the detector is not completely centered on the aperture. Unlike the beams of detectors at the center of the focal plane, the beams of detectors at the edges of the focal plane do not illuminate the aperture evenly and are truncated somewhat severely on one side of the aperture. This effect is suspected to have been caused by a variation in the index of refraction of the inner layer dielectric towards the edges of each tile.

We can quantify this effect and understand the distribution of the amount of beam steer across the focal plane by determining the displacement of the center of the beam from the center of the aperture. Figure 4.3 shows the amount of beam steer (the distance between the center of the beam and the center of the aperture) at the plane at which the map was taken. The center of the aperture is calculated based on the expected angular displacement of the pixel from the boresight on the sky, and the distance of the mapper from the aperture. The center of the beam is obtained by fitting a two dimensional Gaussian. Figure 4.2 shows that the steered beams are not very Gaussian, and so the fit doesn't completely capture the exact center of the beam. As a result, the distance of the beam center from the center of the aperture is a lower limit on the amount of beam steer. We quote the beam steer in inches measured at the plane at which we take the beam map.

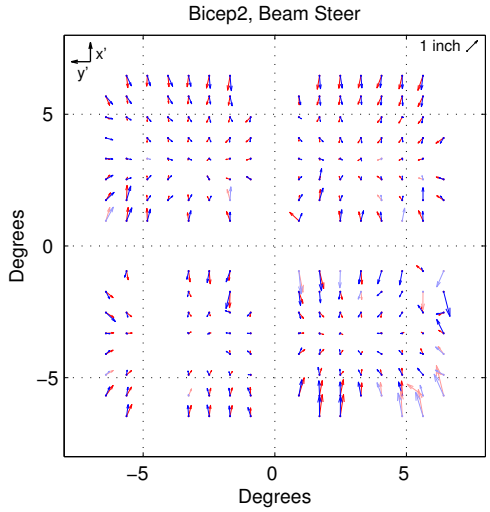

Figure 4.3: Beam steer in BICEP2. The arrows show the distance between the center of the near field beam compared to the center of the aperture. The pattern is repeatable from tile to tile, and shows a tendency for the beam at the edges of the tile to be steered towards the center of the tile. This beam steering effect causes the beams to be more elliptical in the far field.

The beam steer effect occurs along all four edges of the tile, but is most prominent along the top and bottom edges of the tile, and is negligible at the center of the tile. The beams along the top and bottom edges of the tile are the most vertically displaced from where they should be. The right and left edges of the tile are also affected, as you can see a slight displacement of the beams towards the center of the tile, but this effect is less dominant.

BICEP2's beam steer is 0.9 ± 0.4 inches around the edges of each tile, with the largest beam steer occurring on the top and bottom of each tile. The Keck Array beam steer for the 2012 observing season is 0.8 ± 0.4 inches around the edges of the tile. On the whole, the magnitude and pattern of beam steer look about the same from tile to tile, as well as from receiver to receiver.

The beam steer effect causes parts of the beam to be truncated at the aperture. This

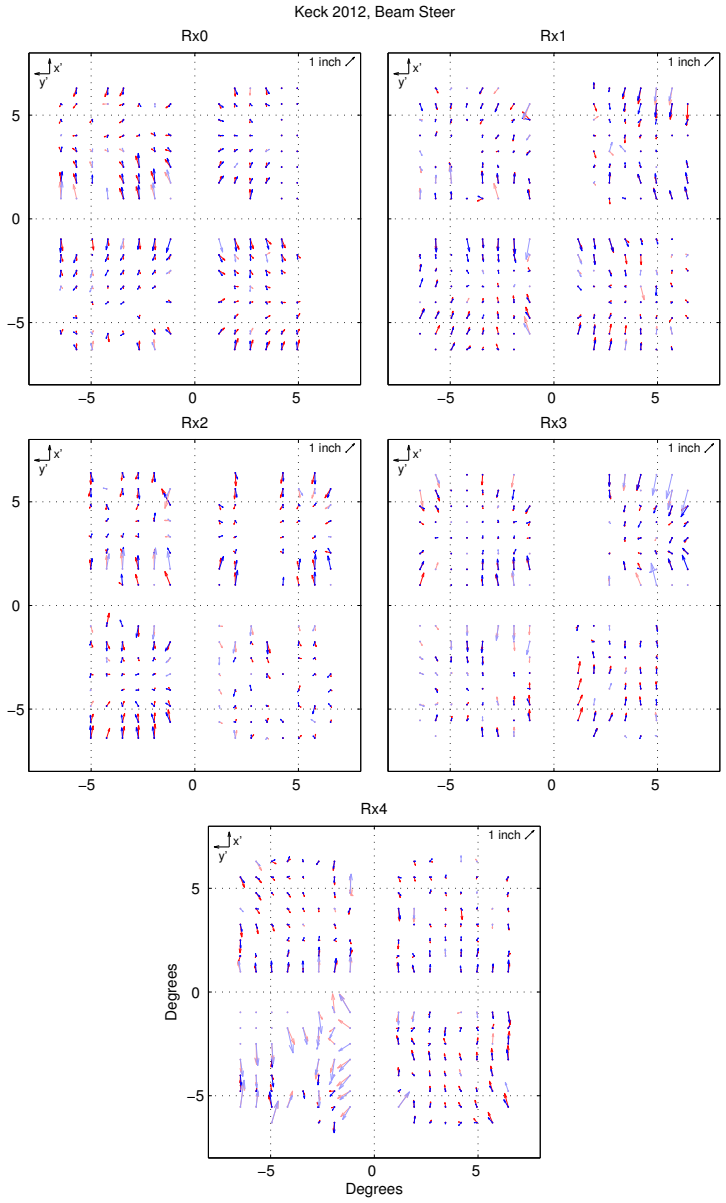

Figure 4.4: Beam steer in the Keck Array for the 2012 observing season. The arrows shows the difference between the center of the near field beam compared to the center of the aperture. The pattern is repeatable from tile to tile, and shows a tendency for the beam at the edges of the tile to be steered towards the center of the tile. The beam steer pattern looks very similar from tile to tile, and receiver to receiver.

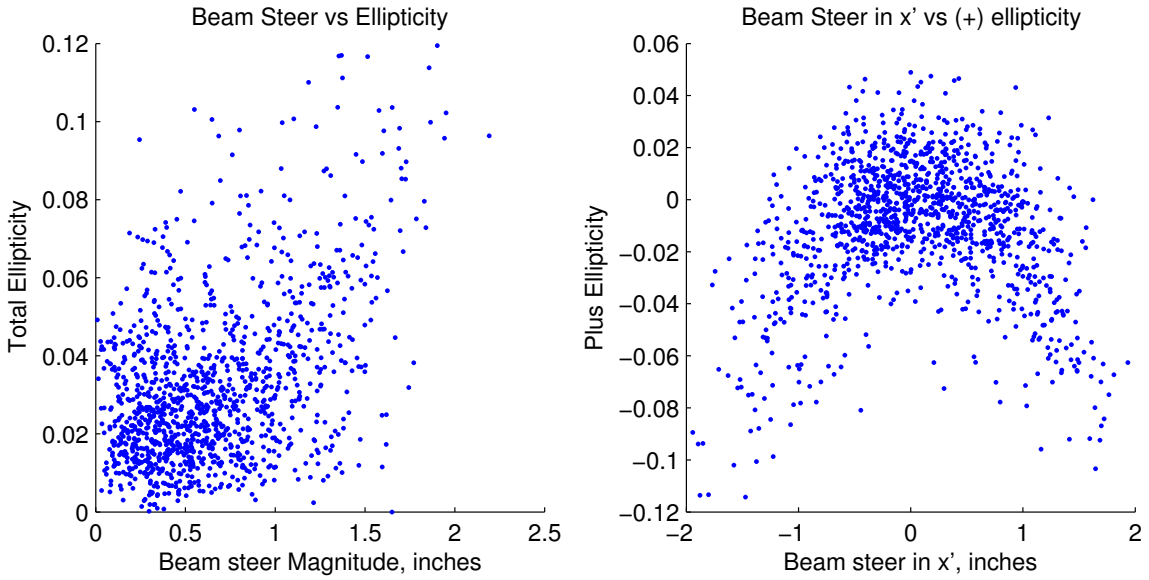

Figure 4.5: Left: The correlation between the magnitude of the per-detector beam steer and per-detector ellipticity for the Keck 2012 observing season. Right: The correlation between beam steer in the vertical direction, and ellipticity along the x'-axis (negative plus ellipticity). The correlation between the magnitude of beam steer and beam ellipticity is not strong but does confirm the hypothesis that detectors with large amounts of beam steer have larger ellipticities. The ellipticity component that is primarily affected is the negative plus ellipticity component (ellipticity along the vertical direction).

causes the projection of the beam on the sky to be more elliptical. Figure 4.5 shows a scatter plot of the ellipticity of the beams compared to the amount of beam steer. We find a weak correlation between the amount of beam steer and the magnitude of the beam ellipticity, particularly for detectors with large beam steer effects. Much of the beam ellipticity is uncorrelated with the beam steer. However, detectors with large beam steer effects do show a large ellipticity. The plus ellipticity (described in Section 4.2.3) which describes an ellipse oriented along the horizontal y' axis (positive plus ellipticity) and vertical x' axis (negative plus ellipticity) direction is ellipticity component which is primarily affected. The beam steer in the vertical component (along the x' axis as shown) correlates strongly with ellipticity that is vertical.

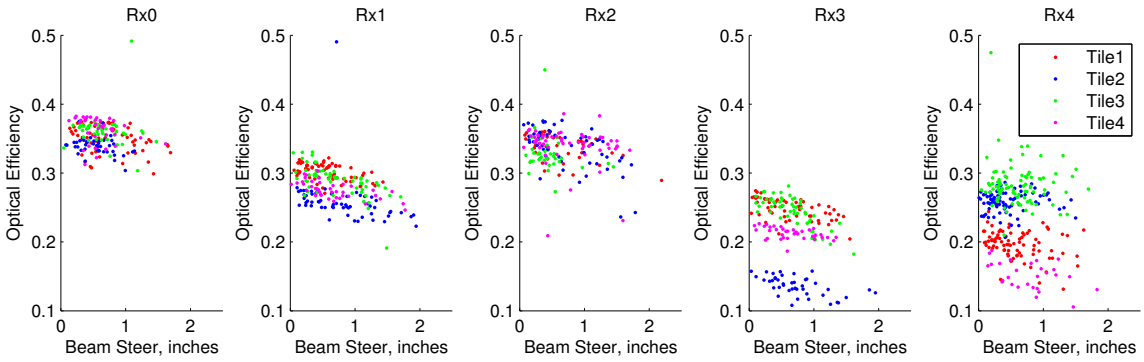

Figure 4.6: The correlation between per-detector beam steer and per-detector optical efficiency for Keck in the 2012 observing season. As the beam is more steered away from the center of the aperture, more of the beam is getting truncated, and so the optical efficiency for beams that are highly steered are the lowest for the tile.

Since the beam steer effect truncates parts of the beam at the aperture, the beam steer effect plays a role in the optical efficiency of the detectors. Figure 4.6 shows that on average, the higher the magnitude of beam steer, the lower the optical efficiency of the detector. We also explored the possibility of correlation between the beam steer and the pointing offset, as well as the correlation between the beam steer and the noise-equivalent-temperature (NET), but did not find any correlation.

4.1.2 Near Field Pointing Mismatch

The near field beam maps for BICEP2 and Keck also show a pointing mismatch between orthogonally polarized, co-located detectors. Figure 4.7 shows an example of the pointing mismatch in one detector pair in the near field.

The near field pointing mismatches are generally consistent from detector to detector for the BICEP2 focal plane, as well as the early Keck Array focal planes. The pointing mismatches are generally along one axis of the summing tree network. In the early focal

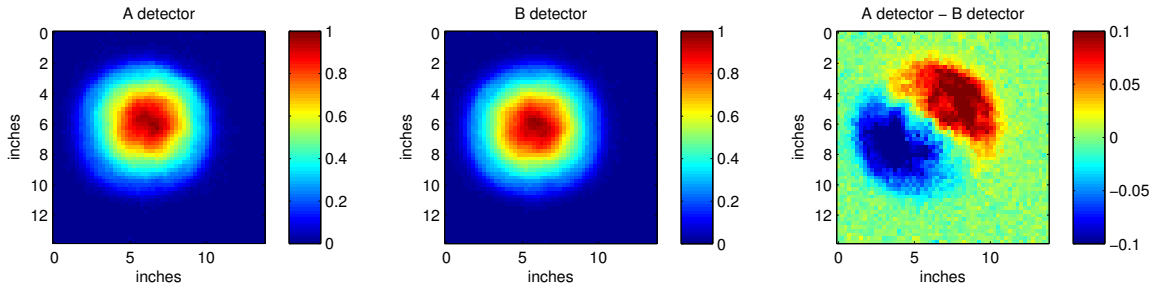

Figure 4.7: An example of the pointing mismatch for a single detector in Receiver 0 in the near field. The near field pointing mismatch alone is not expected to translate to the far field. However, a complicated interaction between the near field pointing mismatch and any imperfections in the optical elements result in a far field pointing mismatch. The near field pointing mismatch has been mitigated in the fabrication process for newer focal planes [26]. *Figure after [4].*

planes, the magnitude of the differential pointing mismatch is consistent across the focal plane.

Ideally, this pointing mismatch in the near field will not be the cause of any mismatch in the far field. However, the non-idealities of the optical elements in the optical path interacts with the near-field pointing mismatch in the detectors resulting in a pointing mismatch between co-located, orthogonal detectors in the far field. Improvements in detector technology, specifically the adding of a lag in the appropriate direction of the summing tree, and a spacing out of the feed lines in the summing network to reduce interference effects, succeeded in improving the pointing mismatches in the near field. The focal planes deployed in the Keck Array in the 2012 and 2013 observing seasons has improved pointing mismatches in some detectors. A full description of the improvements in detector technology can be found in [26]. A more thorough discussion of the resulting far field pointing mismatch can be found in Section 4.2.3

4.2 Far Field Beam Characterization

In order to understand the response of the detector to optical signals, we want to thoroughly understand the beam response of each detector. An advantage of being a small-aperture telescope is the ability to fully characterize the optical performance of the telescope from the ground. The aperture of the telescope is 264 mm, and the designed resolution of the telescope is about half a degree. So the far field of the telescope is $\sim$70 meters. We can place a microwave source at a distance $>$ 70 meters, and map out the far field response of the telescope. We are, therefore, capable of understanding our entire beam response using microwave sources on the ground.

During the summer calibration seasons, we map the beam response for every BICEP2 and Keck Array array detector in the far field. Using these maps, we extract elliptical Gaussian beam parameter fits for every detector's beam. This allows us to characterize, as a whole, the behavior of the 512 BICEP2 detectors, and 2560 Keck Array detectors. These high signal-to-noise maps are also used to understand the parts of the beams that are not captured in the elliptical Gaussian fits. We use these beam maps in order to try and probe the temperature-to-polarization leakage from the beam mismatches.

4.2.1 Method: Mapping the far field beam response

In order to map out the far field response of the BICEP2 and Keck Array detectors, we place a microwave source in the far field, and then map out the response of the beams.

At the South Pole, the Martin A Pomerantz Observatory (MAPO) (where the Keck Array is housed), and the Dark Sector Laboratory (DSL) (where BICEP2 is situated) are approximately 200m apart. On the roof of each building, we place a mast that is about 40

feet tall. The distance from the Keck Array to the DSL mast is 211 meters, and the distance from BICEP2 to the MAPO mast is 193 meters. At the top of the mast, we bolt calibration sources pointed towards the experiment which we are calibrating.

The calibration sources that we use include broad spectrum noise sources (BSNS) centered at the observing frequencies as well as thermal sources. The BSNS are powerful point sources with amplitudes that can be adjusted. The BSNS can be linearly or circularly polarized. The BSNS have primarily been used to determine the polarization angle for each detector as well as the cross-polar response of the detectors in the far field. Since the BSNS can have a large amplitude, they are also used to map dim sidelobe features at large angles away from the center of the beam.

In order to characterize the unpolarized far field beam response, however, we use unpolarized thermal sources. The thermal sources have an aperture open to a 45° mirror that is placed to redirect signals from the sky through the aperture. An Eccosorb covered fan-blade spins at a tunable frequency and chops the signal between ambient temperature ($\sim$250 K) and cold sky ($\sim$ 15 K). We use "ze-choppa", a thermal source with an aperture of about 20 cm in diameter as well as the "uber-chopper", a thermal source with a 45 cm aperture. We use a chop frequency of 18 Hz for the smaller aperture source, and a chop frequency of 10 Hz for the larger aperture source. The thermal source is relatively unpolarized across much of the source aperture, but is partially polarized at the edges of the aperture. The aperture of the source is smaller than the beam width, and so any polarization from the edge of the aperture is smeared out by the beam as the telescope scans across the source. The sources are shown in Figure 4.8.

The BICEP2 and Keck Array telescopes sit in a reflective groundshield (Section 2.5)

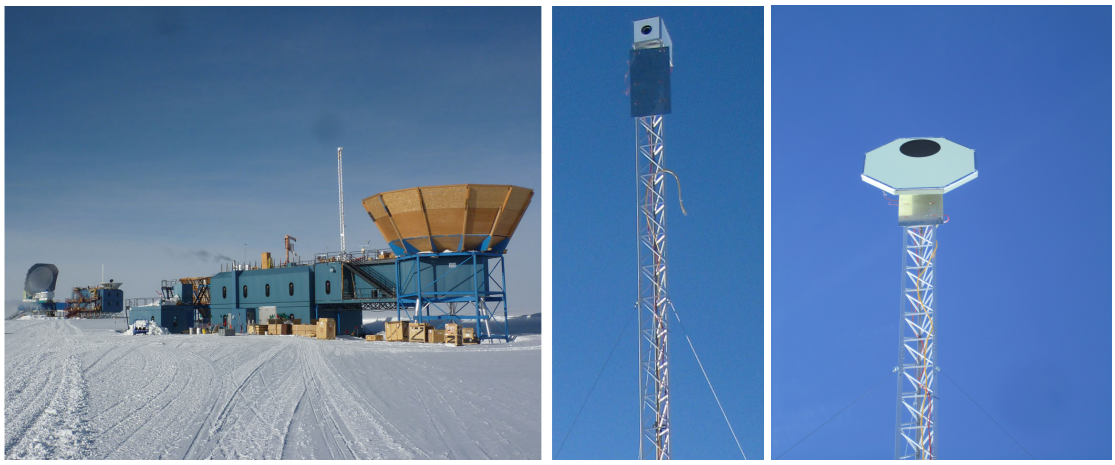

Figure 4.8: Left: DSL and MAPO, where BICEP2 and the Keck Array resides, are ∼200 meters apart. Center: The broad spectrum noise source on top of a mast. Right: The 45 cm aperture thermal source placed on a mast for mapping. Using the sources placed on buildings ∼200 m away, we can thoroughly map the far field response of the beams. We use two thermal sources, one with a 20 cm aperture, and another with a 45 cm aperture. *Figure from [25].*

that is designed to shield the telescope from any stray incoming radiation from the ground. The groundshields are permanent structures that extend a few feet above the top of the telescopes. The Keck Array groundshield can be seen in Figure 2.6 and is visible in Figure 4.8.

To allow BICEP2 and the Keck Array to see over their groundshields, we place a flat aluminum mirror at ∼40 deg angle above the telescope. We call this the "far field flat". The BICEP2 far field flat is a 1.6 m x 1.1 m honeycomb aluminum sheet, hexagonal in shape, sized and placed appropriately to ensure that all the beams coming out of the telescope at any boresight angle (also called deck angle) is redirected by the mirror. The Keck Array far field flat is a 1.8 m x 2.7 m sheet of honeycomb aluminum backed with three box-beams. The mirror is held above the Keck Array telescope with 4.3 m long carbon-fiber rods in a hexapod-like structure attached to the mount. We use the telescope itself to raise the mirror above the instrument, and a pulley system to raise the mirror high enough to see

Figure 4.9: The far field beam mapping setup for BICEP2 on the left, and the Keck Array on the right. BICEP2 and the Keck Array uses a flat honeycomb aluminum mirror in order to look over the groundshield towards the microwave source located on the opposite building. *Figure from* BICEP2*/Keck Array Collaboration*.

over the groundshield. Unlike for BICEP2, the Keck Array far field flat does not redirect all the individual Keck Array receivers' beams towards the source. The size of the mirror is limited by the scope of the lifting operation; it would be difficult to place an even larger mirror on top of the mount. The Keck Array far field flat allows at most two receivers worth of detectors to be mapped at the same time. Since the mirror for BICEP2 and the Keck Array is mounted onto the the parts of the mount that only move in azimuth and elevation, we can freely rotate the boresight (deck angle) of BICEP2 and the Keck Array. For the Keck Array, rotating the deck angle allows us to move the receivers under the mirror in succession. The mirror only has to be flatter that 2 mm across the length of the beam aperture of 264mm. The repeatability of the beam parameter measurements is evidence that the mirror is flat enough. Figure 4.9 shows the far field flat mirrors above BICEP2 and the Keck Array.

We take far field beam maps for BICEP2 and the Keck Array by rastering in azimuth

at a scan rate of 2° per second and at 0.05 degree elevation steps. The BICEP2 maps last $\sim$4 hours and are are taken at four deck angles (0°, 90°, -90°, -180°) in order to take advantage of the symmetry of the focal plane. The Keck Array maps take $\sim$7 hours. The Keck maps are taken at 10 different deck angles, which are 36° apart. This ensures that we obtain multiple maps at multiple deck angles for every detector.

We take data at multiple deck angles in order to understand the consistency of the beam shapes, and as a check that a rotation of the receiver does not affect the results of the measurement. As the effective position of the source is $\sim 2^\circ$ above the horizon, we are unable to avoid mapping the mast and building that the source is on. Multiple boresight angles will allow more thorough mapping of the far field beam response to wider radial distances away from the center of the beam.

The chop rate of the sources are detected with an optical sensor that is placed close to the aperture, and sent via optical fiber between buildings, from MAPO to DSL or vice versa where the generic control program (GCP) records it. We do this in order to pick out the signal of the chopper as well as to reduce the noise. During beam mapping runs, we take data at a fast data-rate (150Hz) as the low-pass filtering used in regular data taking will filter the chop frequency. The raw timestreams allow us to see the world at the South Pole in the microwave, and with a resolution of half a degree. Figure 4.10 show a map made from the undemodulated timestreams for a single pixel. The thermal source can barely be seen at all.

In the processing of the data, the raw timestreams for BICEP2 have been filtered to match the readout system filtering while the raw timestreams for Keck Array are deconvolved to account for readout system filtering. The chop frequency is then moved by hand

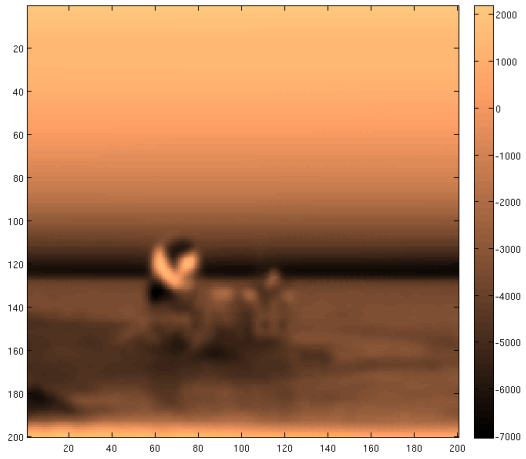

Figure 4.10: Binning the undemodulated timestream data for a single pixel displays a view of DSL and the South Pole Telescope in the microwave at a resolution of $0.5°$. The ground and the South Pole telescope is clearly seen to be bright, while the chopped source signals are not visible at all.

to match the chop of the source in the timestreams. The timestreams are demodulated using the recorded chop frequency.

The pointing of each detector is then calculated. The parallax of each detector as well as the reflection off the mirror is taken into account using a complicated pointing model that describes the BICEP2 and Keck Array mount system as well as the position of the mirror. Using each detector's pointing information, the demodulated timestream for that detector is then binned into a map that shows the far field beam response of each detector. For each detector, we have deep, high signal-to-noise maps of the beam response. Figure 4.11 shows the far field beam response for BICEP2 and the Keck Array. The maps of each detector's response to the chopped thermal source is rotated to the same coordinate system before being centered and coadded. The stacked beams clearly shows the main beam features, as

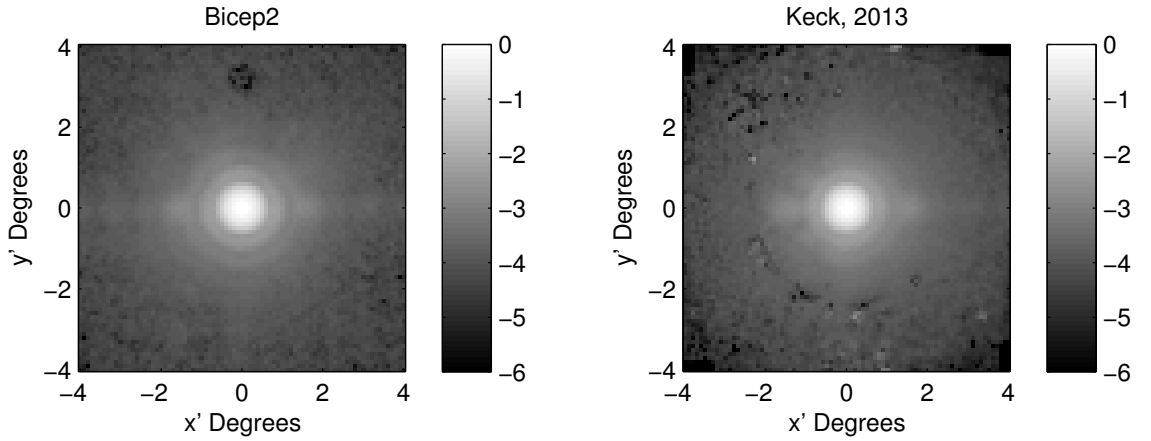

Figure 4.11: Left: The far field beam response for BICEP2, built from all good channels in BICEP2. Right: The far field beam response for Keck Array. The maps included here have been rotated to the same coordinate system before being centered and coadded. The maps have been taken using the 45 cm aperture thermal source. The high signal to noise of these maps clearly display the Airy ring structure as well as inductive cross-talk beams on either side of the beam. *Figures from [25].*

well as Airy ring structures, as well as inductive cross talk beams that appear at 1.6 degrees away from the main beam. Figure 4.12 shows the beam profile for the BICEP2 and Keck Array detectors centered and coadded across all detectors that are used in the final science analysis.

From these maps, we extract the per-detector beam parameters which are then used in

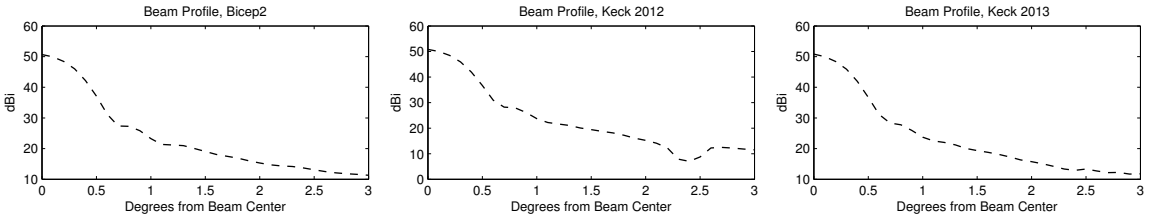

Figure 4.12: Left: Beam profile for BICEP2. Center: Beam profile for Keck 2012. Right: Beam profile for Keck 2013. The beam profiles have been made from map that has been coadded over all detectors used in the final science analysis. *Figure after [25].*

the determination of the channel cuts, as well as in the subtraction of predicted temperature-to-polarization leakage. These beam maps are also used to determine the residual level of temperature-to-polarization leakage after deprojection of the dominant mismatch modes, as described in Chapter 5.

4.2.2 Beam Parameterization

In order to facilitate the parameterization of the beams, we first define a coordinate system that is fixed to the focal plane as projected onto the sky. Figure 4.13 shows the coordinate system defined for a pixel, P, that is a distance (r, θ) away from position of the boresight, B. The $\theta = 0$ line is defined with respect to the focal plane and is the great circle that divides tile 1 from tile 2. K is the angle of boresight rotation, also called the deck angle. K' is the drumangle for each receiver which describes the rotation of each receiver with respect to the $K = 0$ line. Note that for BICEP2, the drumangle, K', is 0, but for each Keck receiver, the drumangle is 72° apart from each other. For each pixel, P, we define the (x', y') coordinate system locally. The positive x' axis is defined to be pointed along the great circle that passes through point P that is an angle of $-\theta$ away from the $\hat{r}$ direction of the pixel. The y' axis is defined to be the great circle that is $+90^\circ$ away from the x' axis. The (x', y') coordinate system is then projected onto a flat surface at P. The pixel position, P, is also defined to be the common pair centroid of each detector pair. This coordinate system is independent of the position of the deck angle, K, or the drumangle, K'.

We parameterize the BICEP2 and Keck Array beams as elliptical Gaussian. A 2-d elliptical Gaussian is parameterized with six parameters, one parameter that describes the gain, two parameters that describe the position of the center of the beam, and three parameters

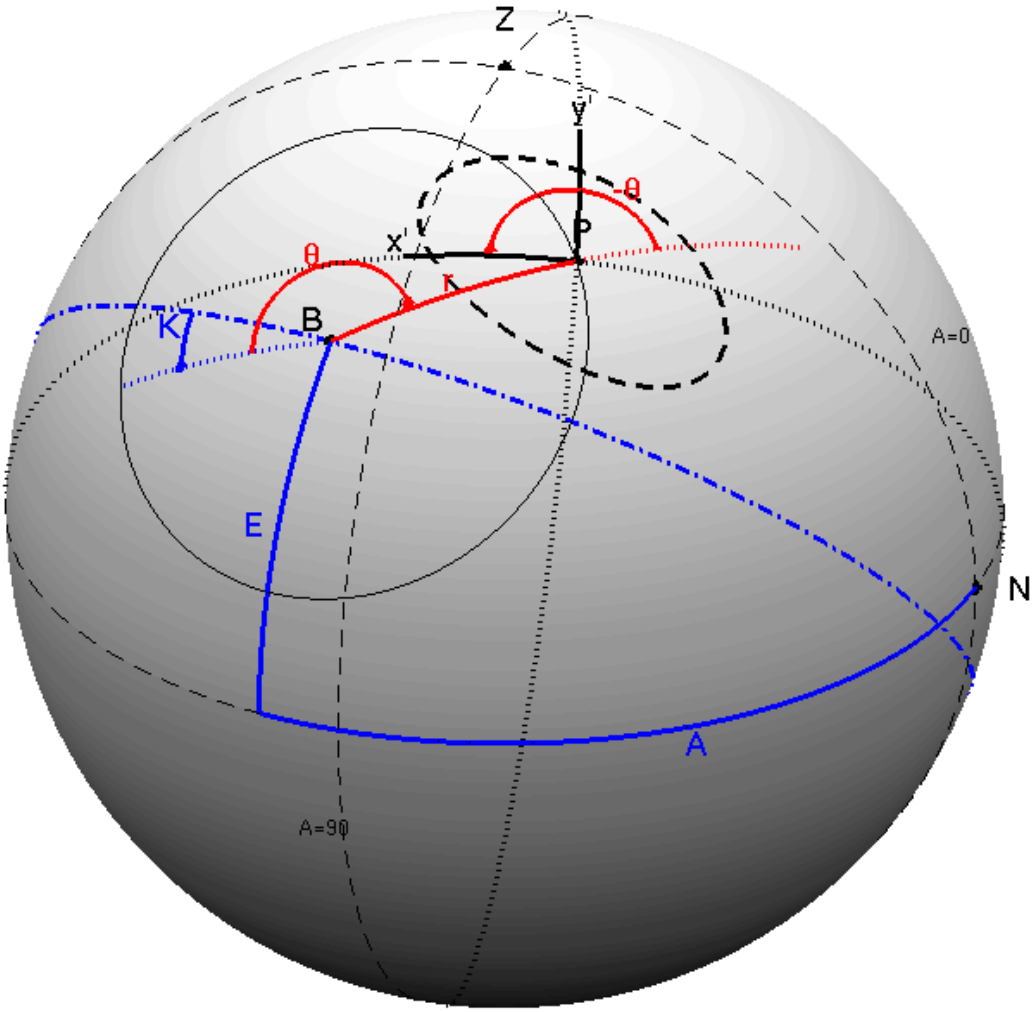

Figure 4.13: The coordinate definitions for the beam parameter basis. For each pixel, P, which is located a distance (r, θ) from the boresight, B, we define an (x', y') coordinate system locally. The positive x' axis is defined to be along the great circle that passes through the point P that is an angle $-\theta$ from the $\hat{r}$ direction of the pixel. The y' axis is defined as the great circle that is $+90°$ away from the x' axis. The (x', y') coordinate system is then projected onto a flat surface at P. K is the deck angle of the telescope, and K' the drumangle of each receiver. *Figure by Stefan Fliescher.*

that together describe the beam width and the ellipticity. Mathematically, we can describe a 2-d elliptical Gaussian as

$$f = \frac{1}{\Omega} e^{-\frac{1}{2}(\vec{x}-\vec{\mu})^T \Sigma^{-1} (\vec{x}-\vec{\mu})} \tag{4.1}$$

where Ω is the beam normalization, and $\vec{x}$ is the position vector of the beam center, and $\vec{\mu}$ is the position of the origin. The covariance matrix, Σ, can be parameterized in various relevant bases. In our calculations, we switch between a few bases, and I will outline them here.

We start with a parameterization that describes the beam width in the x and y axes for a given beam map that is binned in x and y axes.

$$\Sigma = \begin{pmatrix} \sigma_x^2 & \rho\sigma_x\sigma_y \\ \rho\sigma_x\sigma_y & \sigma_y^2 \end{pmatrix} \tag{4.2}$$

σ_x is the beam width in the x-direction, σ_y is the beam width in the y-direction, ρ is the correlation coefficient.

From this basis, we can rotate the basis into a more common parameterization that describes the 2-d Gaussian beam by the beam width in the major and minor axes, as well as the rotation angle, α, away from the x-axis.

$$\Sigma = R^{-1} C R \tag{4.3}$$

where R is the rotation matrix and the beam width in the major axis, σ_{maj}, as well as the beam width in the minor axis, σ_{min}, is encoded in

$$C = \begin{pmatrix} \sigma_{maj}^2 & 0 \\ 0 & \sigma_{min}^2 \end{pmatrix} \tag{4.4}$$

The rotation matrix, R, is described as

$$R = \begin{pmatrix} \cos\alpha & \sin\alpha \\ -\sin\alpha & \cos\alpha \end{pmatrix} \tag{4.5}$$

where α is the angle from the x-axis to the major axis (counterclockwise).

In these parameterizations, we can see that the ellipticity of the Gaussian beam is not intrinsically defined. We can define the ellipticity as

$$\epsilon = \frac{\sigma_{maj}^2 - \sigma_{min}^2}{\sigma_{maj}^2 + \sigma_{min}^2} \tag{4.6}$$

However, this definition of ellipticity does not intrinsically encode the direction of the major or minor axis. We require both ϵ and α in order to fully capture the magnitude as well as orientation of the ellipse. Moreover, in this coordinate system, the differential ellipticity is difficult to define. It has to encode not only the difference in the magnitude of the ellipticity defined in 4.6 but also describe the difference in the orientation of the ellipticity.

There is, however, an equivalent parameterization of Σ that completely describes the magnitude and the direction of the ellipticity of a given beam in an orthogonal basis. This basis encodes not only the magnitude of the ellipticity but also the direction at which the ellipse is pointed. We introduce the parameters p and c to describe the ellipticity in the 'plus' (+) and 'cross' (x) directions respectively. Here we have

$$\Sigma = \begin{pmatrix} \sigma^2(1+p) & c\sigma^2 \\ c\sigma^2 & \sigma^2(1-p) \end{pmatrix} \tag{4.7}$$

The relation between σ, p and c and σ_{maj}, σ_{min} and α is as follows:

$$\sigma^2 = \frac{\sigma_{maj}^2 + \sigma_{min}^2}{2} \tag{4.8}$$

$$c = \sin 2\alpha \frac{\sigma_{maj}^2 - \sigma_{min}^2}{\sigma_{maj}^2 + \sigma_{min}^2} \tag{4.9}$$

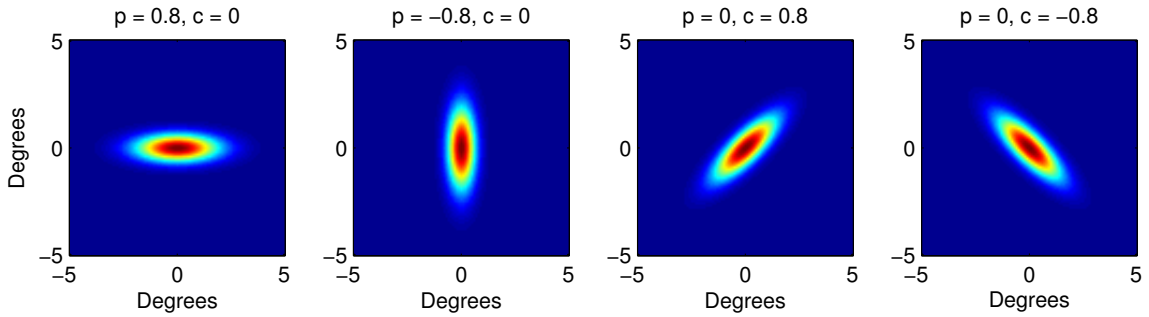

Figure 4.14: The orientation of ellipses with positive and negative p and c. All ellipses here have a beam width (σ) of 1°. Plus ellipticity, p is oriented along the x-axis or the y-axis, while cross ellipticity, c, is oriented diagonally. This definition encodes the magnitude and orientation of the ellipticity. *Figure after Stefan Fliescher.*

$$p = \cos 2\alpha \frac{\sigma_{maj}^2 - \sigma_{min}^2}{\sigma_{maj}^2 + \sigma_{min}^2} \tag{4.10}$$

Here we have magnitude of ellipticity to be defined as

$$\epsilon = \sqrt{p^2 + c^2} \tag{4.11}$$

The p and c parameters completely describe the magnitude and orientation of an ellipse with a set of bases which are orthogonal to each other. More importantly, a differential ellipticity can now be described very simply as the difference between the p and c parameters of each ellipse. The definitions of p and c are shown in Figure 4.14. Positive p is oriented along the x axis and negative p is oriented along the y axis. Positive c is oriented along the $y = x$ line and negative c is oriented along the $y = -x$ line.

Thus, we can completely describe the elliptical Gaussian using 6 parameters, the normalization, Ω, the x and y position of the beam, the beam width, σ, and the ellipticity in the 'plus', p, and 'cross', c, directions.

Since our observing strategy for detecting polarization requires us to difference the timestreams for a pair of co-located, orthogonally-polarized detectors (See Section 2.3), it

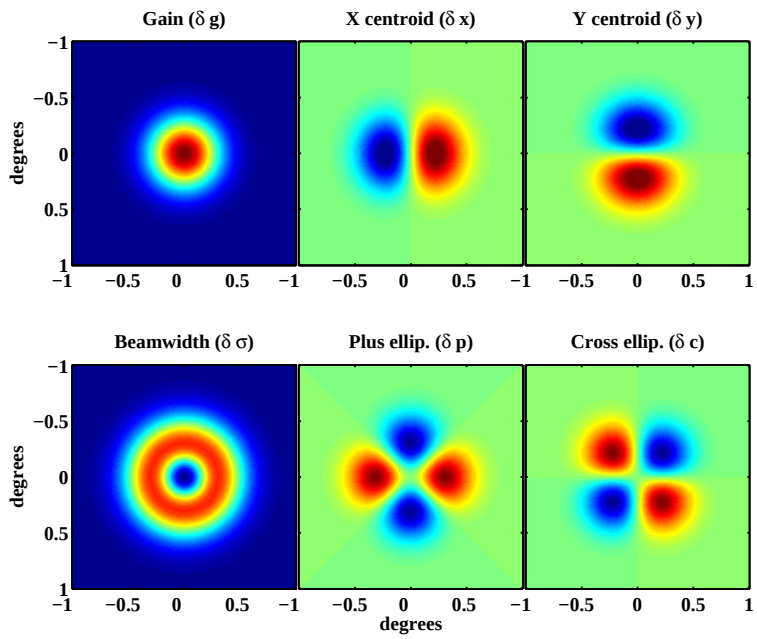

Figure 4.15: Differential mismatch modes for elliptical Gaussian with mismatched gains, X pointing, Y pointing, beam width, plus and cross ellipticities. These mismatch modes are directly related to the deprojection basis used to remove the temperature-to-polarization leakage from beam mismatches in CMB data. *Figure from [24].*

is critical that we understand the properties of our differenced beams. This parameterization allows us to describe the difference beams of a co-located, orthogonally polarized pair of detectors as a simple subtraction of the per-detector beam parameters as shown in Table 4.2.

The difference beam mismatch modes, in this parameterization, can directly be related to the first order terms of a linear basis that is built by perturbing a circular Gaussian. This ensures that the parameterization of the beam is directly related to the deprojection basis used in the timestream deprojection, allowing us to easily compare the modes that we are deprojecting to the difference beam parameters [24, 25]. Figure 4.15 shows the differential modes of two elliptical Gaussian beams with mismatched gains, pointing, beam widths and ellipticities.

4.2.3 Measured Beam Parameters

Using this basis, we can now extract the relevant beam parameters for every detector. For every detector's beam map, we fit a two dimensional elliptical Gaussian and extract the pointing parameters (x and y), the beam width (σ), and the ellipticity parameters (p and c). Each measurement of the main beam parameters must pass a set of checks in order to be included in the final beam parameter estimation. These checks include a check on the amplitude of the beam, the beam width, and ellipticity in order to ensure that the elliptical Gaussian fit hasn't failed, or that a bad beam map with spurious artifacts isn't dominating the elliptical Gaussian fit. For Keck, a check is also made to ensure that the detector's beam is bouncing off the mirror towards the source and is unaffected by the edge of the mirror. The per-detector beam parameters are calculated as the median across all measurements to reduce the impact of bad measurements on the final beam parameters. The error is taken to be the standard deviation across the number of measurements.

From the beam maps, we can characterize every working detector's beam width (σ) and ellipticity (p and c). Since the beam maps are taken using the aluminum transition, and we do not perform gain calibration procedures during beam mapping runs, we are not able to determine the relative gain of the detectors using the beam maps. Also, a gain calibration using the aluminum transitions in high loading conditions might not accurately reflect the gain of the detectors on the titanium transition during science observations. The absolute calibration of the detector gains are determined by cross-correlating the final CMB maps made using each detector, with the Planck 143 GHz map [1]. Since the beam mapping procedure involves a mirror and a complicated pointing model, we also do not determine the absolute pointing measurements of each detector. The absolute pointing of the detectors are

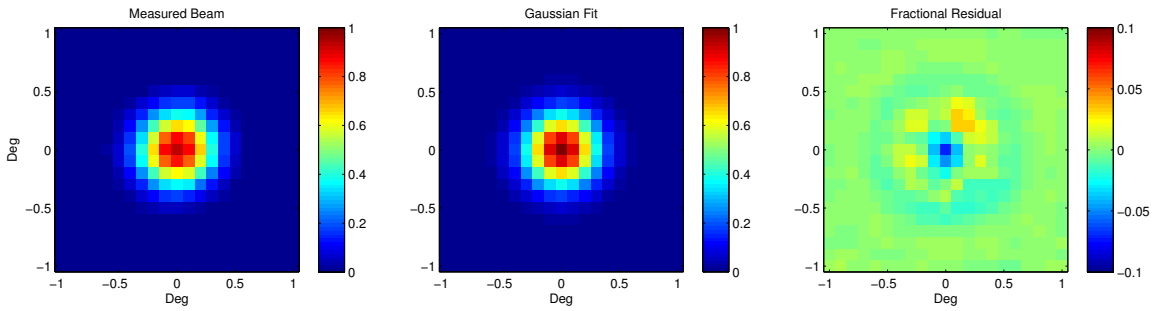

Figure 4.16: Left: Representative far field beam map for a single detector in BICEP2. Middle: The Gaussian fit to the beam. Right: Residual after subtracting the fit from the map. As we can see, the residual after the fit is small, however, the entirety of the BICEP2 and Keck Array beams are not perfect elliptical Gaussian. *Figure from [25].*

also obtained by cross-correlating per-detector maps of the CMB with the Planck 143 GHz map.

Figure 4.16 shows an example map for a single detector in BICEP2, the elliptical Gaussian fit, and the residual after subtracting the fit. As we can see, much of the power in the beam is captured by the elliptical Gaussian fit, resulting in a small residual.

Average beam widths and ellipticities across all good detectors used for BICEP2 and the Keck Array are shown in Table 4.1. Also listed is the standard deviation across the focal plane as well as the median measurement error on each detector's beam parameter. For the Keck Array, we list also the average beam parameter for all good detectors in the array of five receivers. The BICEP2 beam parameters were obtained using a set of 24 beam maps, 12 taken with the "ze-choppa" source in November and December 2011, and 12 taken with the "uber-chopper" source in November 2012. The measurements of the beam parameters using the different sources have been found to be consistent across the two years, and so we choose to combine the two data sets to obtain the final beam parameters for BICEP2. The Keck Array beam parameters for 2012 and 2013 are obtained from an independent

set of beam maps taken in February 2012 and February 2013 respectively. The data taken in February 2012 uses the "ze-choppa" source while the data taken in February 2013 uses the "uber-chopper" source. The primary reason we choose to separately characterize each Keck Array receiver for each year is due to the changes in the configurations of three out of the five receivers going from the 2012 to the 2013 observing season. In going to the 2013 observing season, we removed the focal planes of Receiver 3 and 4 and swapped out one tile (Tile 1) in the Receiver 1 focal plane. A completely new focal plane was placed into Receiver 4. Since BICEP2 was decommissioned at the end of the 2012 observing season, we placed the BICEP2 focal plane into Receiver 3. The changes in configuration increased the sensitivity of the Keck Array.

Receiver		Beam Parameter		
		Beam width, σ_i (Deg)	Ellipticity Plus, p_i $(+)$	Ellipticity Cross, c_i $(\times)$
BICEP2		$0.221 \pm 0.005 \pm 0.002$	$0.013 \pm 0.03 \pm 0.02$	$0.002 \pm 0.03 \pm 0.01$
Keck 2012	Rx0	$0.216 \pm 0.004 \pm 0.003$	$0.011 \pm 0.03 \pm 0.02$	$0.007 \pm 0.03 \pm 0.02$
	Rx1	$0.215 \pm 0.004 \pm 0.003$	$0.009 \pm 0.03 \pm 0.02$	$0.021 \pm 0.02 \pm 0.02$
	Rx2	$0.217 \pm 0.004 \pm 0.003$	$0.015 \pm 0.03 \pm 0.02$	$0.011 \pm 0.03 \pm 0.03$
	Rx3	$0.216 \pm 0.004 \pm 0.003$	$0.010 \pm 0.03 \pm 0.02$	$0.006 \pm 0.02 \pm 0.02$
	Rx4	$0.217 \pm 0.004 \pm 0.003$	$0.009 \pm 0.02 \pm 0.02$	$0.017 \pm 0.02 \pm 0.02$
	All	$0.216 \pm 0.004 \pm 0.003$	$0.011 \pm 0.03 \pm 0.02$	$0.013 \pm 0.02 \pm 0.02$
Keck 2013	Rx0	$0.218 \pm 0.004 \pm 0.003$	$0.008 \pm 0.03 \pm 0.02$	$0.008 \pm 0.02 \pm 0.02$
	Rx1	$0.214 \pm 0.004 \pm 0.003$	$0.006 \pm 0.03 \pm 0.03$	$0.014 \pm 0.02 \pm 0.02$
	Rx2	$0.217 \pm 0.004 \pm 0.003$	$0.009 \pm 0.03 \pm 0.03$	$0.009 \pm 0.03 \pm 0.03$
	Rx3	$0.218 \pm 0.005 \pm 0.003$	$0.009 \pm 0.03 \pm 0.02$	$0.004 \pm 0.02 \pm 0.02$
	Rx4	$0.211 \pm 0.002 \pm 0.003$	$-0.001 \pm 0.02 \pm 0.02$	$0.006 \pm 0.03 \pm 0.02$
	All	$0.216 \pm 0.005 \pm 0.003$	$0.006 \pm 0.03 \pm 0.02$	$0.008 \pm 0.02 \pm 0.02$

Table 4.1: Measured detector-pair beam parameters for BICEP2 and Keck Array. The mean and scatter across all good detectors are shown, along with the median measurement error. The Keck Array has smaller beam sizes than BICEP2 due to a difference in the placement of the objective lens. *Table from [25].*

The average beam width (σ) over the focal plane is $0.221 \pm 0.006^{\circ}$ for BICEP2, $0.216 \pm$

0.004° averaged over the Keck Array receivers in 2012, and $0.216 \pm 0.005^\circ$ for the Keck Array receivers in 2013. A slight difference in the placement of the objective lens is theorized to explain the difference in the beam widths between Keck Array and BICEP2.

We can see this by looking at the average beam widths for BICEP2, and comparing it to the average beam width for Receiver 3 in the Keck Array 2013 season. Recall the BICEP2 focal plane was moved from BICEP2 into Receiver 3 in 2013. Note that the beam widths for Receiver 3 in the Keck Array season in 2013 are smaller than what is measured in BICEP2. The beam widths for each Keck Array receiver are very repeatable from one receiver to the next. An exception is Receiver 4 during the Keck Array 2013 observing season, which shows a slightly smaller average beam width.

A graphical representation of the beam widths of each detector across the focal plane can be seen for BICEP2 in Figure 4.17. Equivalent focal plane layout figures for each Keck Array receiver can be seen in Figure 4.18 for the Keck Array's 2012 observing season, and Figure 4.19 for the Keck Array's 2013 observing season. The beam widths have been exaggerated for effect, but we can note a pattern of beam width sizes as we move radially along the focal plane. The beams at the center and at the edge of the focal plane have slightly larger beam widths than the detectors at the centers of the tiles. We use a telecentric lens design to accommodate our flat focal plane; however, the optimal plane of focus of the optical system is not precisely flat. Thus for a flat focal plane, the optimal focus is neither at the center of the focal plane nor at the edges, but at a radius containing the maximal number of detectors, thus maximizing the number of detectors in focus.

This pattern of non-optimal focus at the edges and center of the focal plane also results in a radial pattern of ellipticity across the focal plane. Figure 4.20, 4.21 and 4.22 plots the

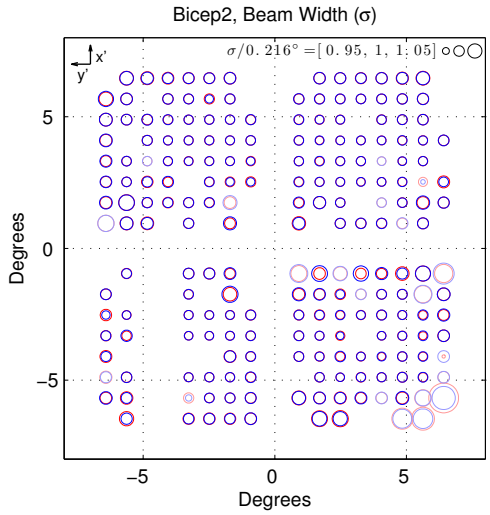

Figure 4.17: BICEP2's per-detector beam widths plotted in focal plane layout, with tile 1 in the upper left. Red and blue colors indicate A and B detector beam widths respectively. Light colors indicate detectors that have been excluded in the science analysis. The beam widths have been exaggerated for effect. The telecentric lens design places the optimal focus on an annulus of detectors that span the center of the tiles in order to maximize the number of detectors in focus. *Figure from [25].*

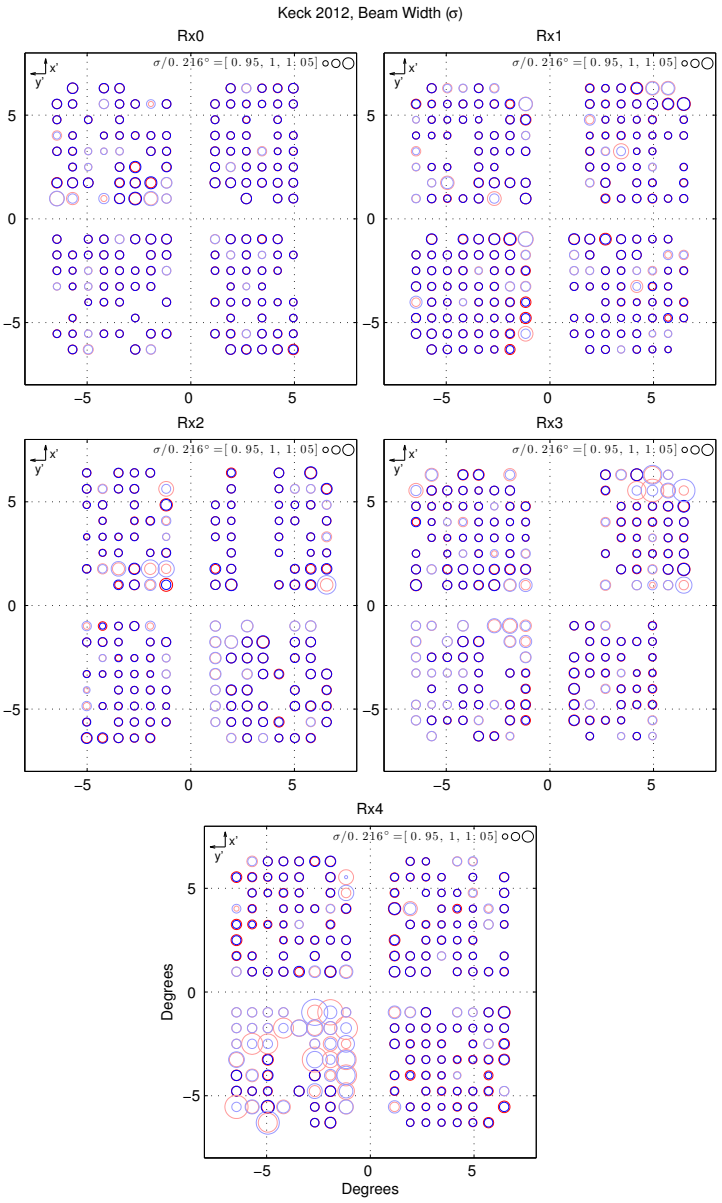

Figure 4.18: Keck 2012 per-detector beam width plotted in focal plane layout for all Receivers in the Keck Array. Red and blue colors indicate A and B detector beam widths. Light colors indicate detectors that have been excluded in the science analysis. The beam widths have been exaggerated for clarity. The Keck Array beam widths are consistent between receivers. *Figure from [25].*

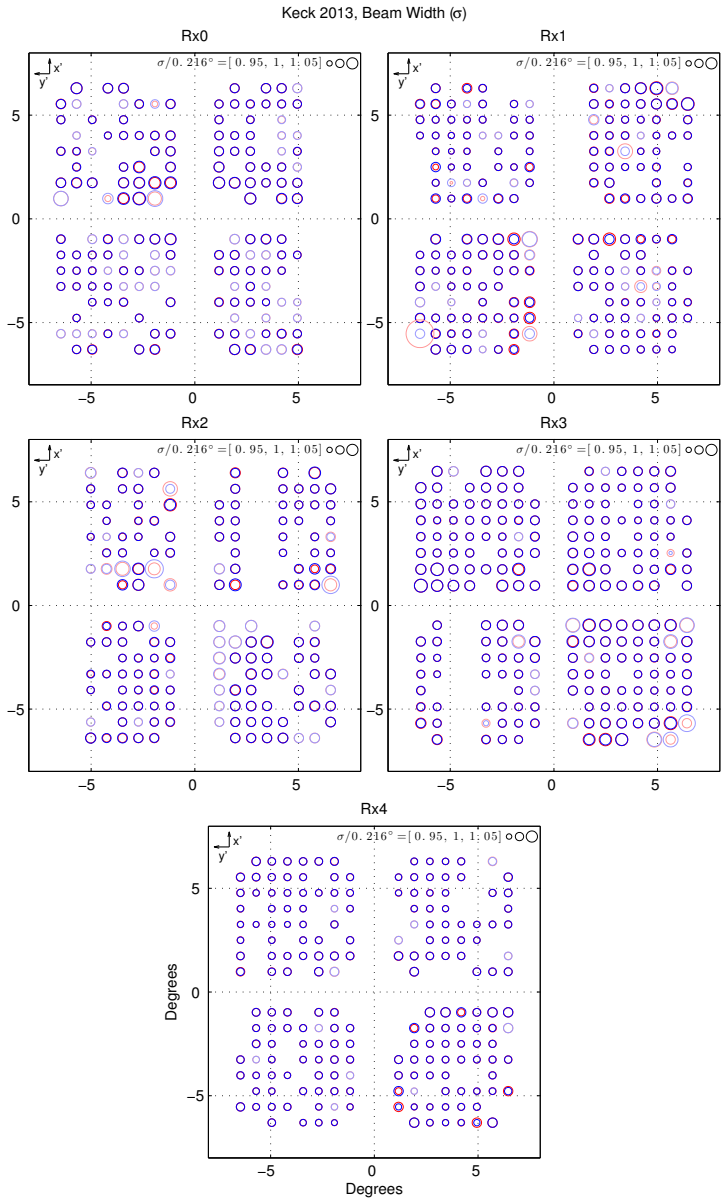

Figure 4.19: Keck 2013 per-detector beam widths plotted in focal plane layout for all Receivers in the Keck Array. Red and blue colors indicate A and B detector beam widths. Light colors indicate detectors that have been excluded in the science analysis. The beam widths have been exaggerated for clarity. Receiver 4 in 2013 shows smaller beam widths than the other receivers. *Figure from [25].*

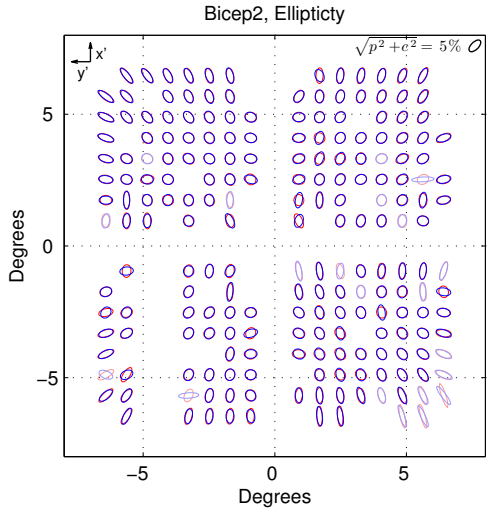

Figure 4.20: A view of BICEP2's per-detector ellipticity in the focal plane, as projected onto the sky. A and B detectors are indicated by red and blue respectively. Light colors indicate detectors that have been excluded from the final analysis. BICEP2's ellipticity clearly shows a pattern across the focal plane. The beams have larger ellipticities as we move towards the edges of the tile and, more obviously, towards the edges of the focal plane. This is expected from the optical design, which places the ideal focus on an annulus with the maximum number of detectors. The beam steer effects which we describe in Sec 4.1.1 also causes higher ellipticities in the edges of the tile in the far field. However, despite the large per-detector ellipticity variation across the focal plane, the differential ellipticity for each detector pair is still quite small. *Figure from [25].*

ellipticity of each detector's beams across the focal plane for BICEP2, and the Keck Array in the 2012 and 2013 observing seasons. The detectors at the edge of the focal plane, and, to some extent, at the edges of the tiles, show a larger ellipticity than the detectors in the centers of the tiles. The beam steer effect (described in subsection 4.1.1) which is observed at the edges of the tiles, steers the center of the beams away from the center of the aperture, also causes higher ellipticities.

We calculate the differential beam parameters for a pair of co-located, orthogonally-polarized detectors by taking the difference between the main beam parameters for each

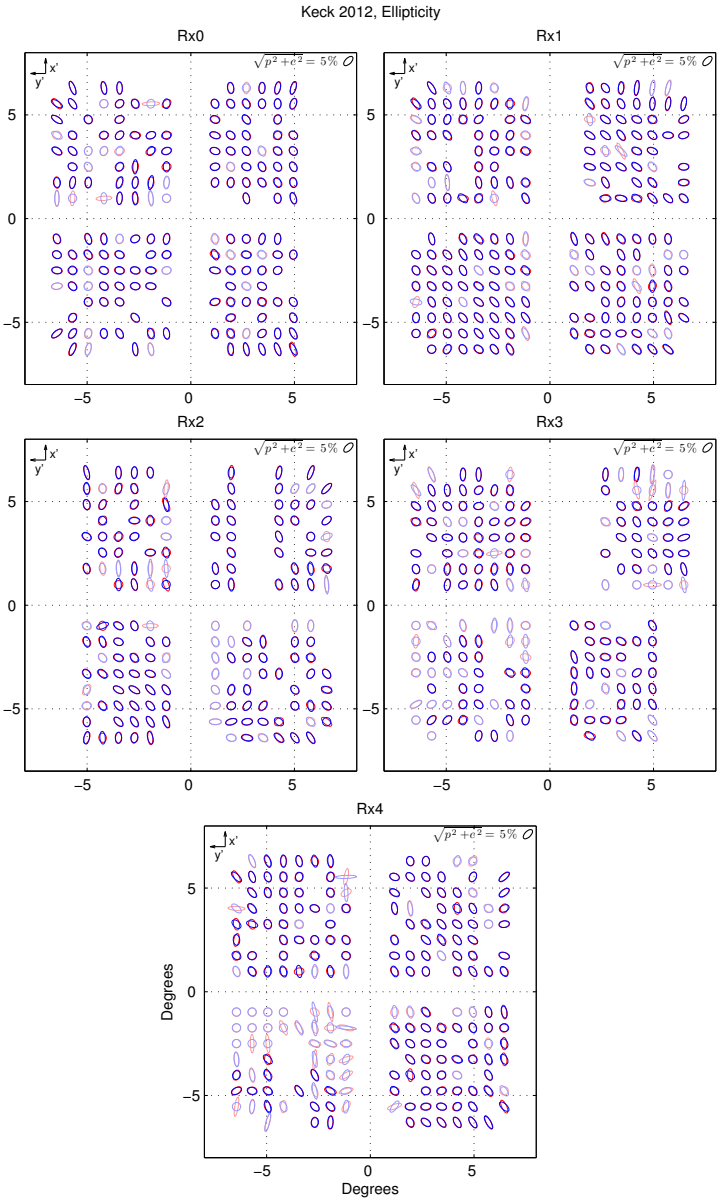

Figure 4.21: A view of the Keck Array per-detector ellipticity in the focal plane, as projected onto the sky for every receiver for the 2012 observing season. A and B detectors are indicated by red and blue respectively. Light colors indicate detectors that have been excluded from the final analysis. The pattern of ellipticity across the focal plane is similar from receiver to receiver. Although the per-detector ellipticity varies widely across the focal plane, the differential ellipticity for each detector pair is small. *Figure from [25].*

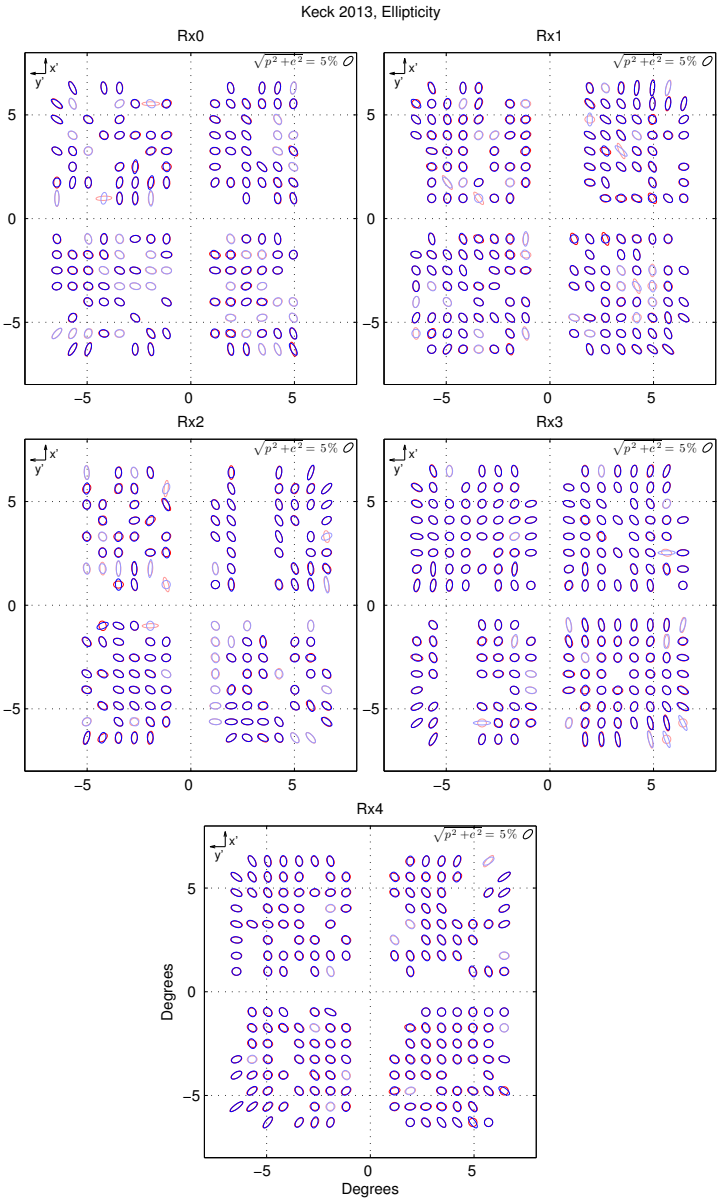

Figure 4.22: A view of the Keck Array per-detector ellipticity in the focal plane, as projected onto the sky for every receiver for the 2013 observing season. A and B detectors are indicated by red and blue respectively. Light colors indicate detectors that have been excluded from the final analysis. The pattern of ellipticity across the focal plane is similar from receiver to receiver. Although the per-detector ellipticity varies widely across the focal plane, the differential ellipticity for each detector pair is small. *Figure from [25].*

detector within the pair, as shown in Table 4.2. The differential beam parameters are measured for each beam map measurement. We present a table of differential beam parameters in Table 4.3. While we are unable to determine the absolute pointing information for each detector, we are capable of ascertaining the differential pointing within a detector pair. The differential pointing measurements are presented in Table 4.4. The scatter is dominated by the variations between pairs in the focal plane, not measurement repeatability. The measurement error on the differential beam parameters is smaller than for per-detector beam parameters.

Parameter	Definition
Differential gain (δg)	$g_A - g_B$
Differential X Pointing (δx)	$x_A - x_B$
Differential Y Pointing (δy)	$y_A - y_B$
Differential Beam Width ($\delta \sigma$)	$\sigma_A - \sigma_B$
Differential Plus Ellipticity (δp)	$p_A - p_B$
Differential Cross Ellipticity (δc)	$c_A - c_B$

Table 4.2: Difference beam parameter definitions.

Receiver		Differential beam parameters		
		Differential Beam Width $\delta\sigma_i$ (degrees)	Differential Plus Ellipticity δp_i (+)	Differential Cross Ellipticity δc_i (×)
BICEP2		$-0.0002 \pm 0.001 \pm 0.001$	$-0.002 \pm 0.016 \pm 0.016$	$-0.003 \pm 0.014 \pm 0.008$
Keck 2012	Rx0	$-0.0002 \pm 0.001 \pm 0.001$	$-0.011 \pm 0.013 \pm 0.004$	$-0.004 \pm 0.009 \pm 0.004$
	Rx1	$0.0007 \pm 0.002 \pm 0.001$	$-0.007 \pm 0.014 \pm 0.004$	$-0.009 \pm 0.008 \pm 0.003$
	Rx2	$-0.0006 \pm 0.002 \pm 0.001$	$-0.006 \pm 0.019 \pm 0.004$	$-0.003 \pm 0.011 \pm 0.004$
	Rx3	$0.0012 \pm 0.002 \pm 0.001$	$-0.007 \pm 0.015 \pm 0.004$	$-0.007 \pm 0.010 \pm 0.004$
	Rx4	$0.0015 \pm 0.003 \pm 0.001$	$-0.002 \pm 0.023 \pm 0.004$	$-0.009 \pm 0.009 \pm 0.003$
	All	$0.0006 \pm 0.002 \pm 0.001$	$-0.006 \pm 0.017 \pm 0.004$	$-0.007 \pm 0.010 \pm 0.004$
Keck 2013	Rx0	$-0.0002 \pm 0.002 \pm 0.001$	$-0.011 \pm 0.014 \pm 0.003$	$-0.003 \pm 0.009 \pm 0.003$
	Rx1	$0.0007 \pm 0.002 \pm 0.001$	$-0.010 \pm 0.013 \pm 0.002$	$-0.008 \pm 0.006 \pm 0.002$
	Rx2	$-0.0006 \pm 0.002 \pm 0.001$	$-0.006 \pm 0.018 \pm 0.003$	$-0.003 \pm 0.011 \pm 0.003$
	Rx3	$-0.0001 \pm 0.001 \pm 0.001$	$-0.007 \pm 0.014 \pm 0.005$	$-0.002 \pm 0.009 \pm 0.005$
	Rx4	$0.0004 \pm 0.001 \pm 0.0004$	$-0.020 \pm 0.005 \pm 0.002$	$-0.002 \pm 0.003 \pm 0.002$
	All	$5 \times 10^{-5} \pm 0.002 \pm 0.001$	$-0.011 \pm 0.014 \pm 0.003$	$-0.004 \pm 0.008 \pm 0.003$

Table 4.3: Measured differential beam parameters for BICEP2 and the Keck Array. The mean and scatter across all good detectors are shown, along with the median measurement error. *Table from [25].*

Receiver		Differential beam parameters	
		Differential X Pointing δx (arcmin)	Differential Y Pointing δy (arcmin)
BICEP2		$0.80 \pm 0.38 \pm 0.23$	$0.80 \pm 0.42 \pm 0.23$
Keck 2012	Rx0	$0.60 \pm 0.42 \pm 0.09$	$-0.26 \pm 0.57 \pm 0.14$
	Rx1	$-0.02 \pm 0.95 \pm 0.08$	$-0.48 \pm 0.42 \pm 0.06$
	Rx2	$-0.24 \pm 0.68 \pm 0.15$	$0.14 \pm 0.63 \pm 0.13$
	Rx3	$-0.39 \pm 1.35 \pm 0.09$	$-0.12 \pm 0.34 \pm 0.06$
	Rx4	$-0.04 \pm 1.11 \pm 0.11$	$-0.06 \pm 0.35 \pm 0.06$
	All	$-0.003 \pm 1.01 \pm 0.10$	$-0.18 \pm 0.52 \pm 0.08$
Keck 2013	Rx0	$0.59 \pm 0.47 \pm 0.10$	$-0.26 \pm 0.61 \pm 0.09$
	Rx1	$0.03 \pm 0.93 \pm 0.07$	$-0.57 \pm 0.45 \pm 0.06$
	Rx2	$-0.26 \pm 0.71 \pm 0.13$	$0.10 \pm 0.63 \pm 0.13$
	Rx3	$-0.09 \pm 0.40 \pm 0.16$	$-0.08 \pm 0.43 \pm 0.15$
	Rx4	$0.21 \pm 0.41 \pm 0.04$	$-0.14 \pm 0.30 \pm 0.03$
	All	$0.08 \pm 0.66 \pm 0.09$	$-0.19 \pm 0.53 \pm 0.08$

Table 4.4: Measured differential pointing for Keck Array. The mean and scatter across all good detectors are shown, along with the median measurement error. While we do not determine absolute pointing from the far field beam maps, we can characterize the relative differences in the pointing centers of co-located orthogonally polarized beams. *Table from [25].*

Figure 4.23, 4.24 and 4.25 displays the orientation of the differential pointing mismatch for BICEP2, and the Keck Array for the 2012 and 2013 observing seasons. The average magnitude of differential pointing in the Keck Array receivers are smaller than the average magnitude of the differential pointing in BICEP2. The scatter in the differential pointing parameters for the Keck Array receivers are of the same magnitude as the scatter for BICEP2, with the exception of Rx1, Rx3, and Rx4 in 2012. These receivers show a large scatter in the differential pointing in the X component. The focal planes for Rx3 and Rx4 were swapped out for the 2013 season, and show an overall smaller differential pointing mismatch than in other receivers. It is interesting to note that while BICEP2's focal plane was placed into Receiver 3 for the Keck Array 2013 season, the average beam width as well

as the average differential pointing has changed. The differential pointing has improved in Receiver 3 compared to BICEP2.

The interactions between the imperfections in the optical elements and the near field detector pointing mismatch turn out to be complicated and not straightforward. We have found that the far field pointing mismatches does not clearly correspond to the near field pointing mismatch.

A significant effort was made in order to understand how the optical elements interacted with the near field pointing mismatch to induce a far field pointing mismatch. One of the most obvious culprits is the possibility of a defocus that can be induced from machining or assembly flaw. To test this hypothesis, we mounted a corrective lens with a long focal length above the window and mapped the far field beams. We mounted concave and convex lenses with 10 m focal lengths on the test setup in the Harvard high bay, as well as a lens with a 20 m focal length at Pole. The additional lenses changed the focus of the optical system, and drastically affected the pointing mismatch in the far field. The amount of improvement of differential pointing for this particular receiver is at best $\sim 30\%$. However, this defocus also caused the beam shapes to be distorted. The distortions of the beam shapes, particularly the changes in the beam shapes of the detectors at the edges of the focal plane, is especially persuasive in convincing us that the telescope was in focus. The annulus of optimum focus on the focal plane is $\sim 80\%$ towards the edge of the detectors, where we have the maximum number of detectors.

The other possible optical defect that would translate the near field beam pointing mismatch into a far field beam pointing mismatch is birefringence in the optical elements. While care was taken in buying cast or compression molded materials, it appears that dif-

ferent manufacturers produce different plastics of different optical quality. In 2010, we deployed with filters made with PTFE that were manufactured by Industrial Plastics. In the process of understanding how the optical elements interacted with the near field pointing mismatch in order to affect the far field pointing mismatch, we placed slabs of PTFE and nylon in front of the telescope, and observed the change in the differential pointing mismatch without the plastic slab, with the plastic slab, and once the plastic slab has been rotated. We find that PTFE sourced from Interplast to be less birefringent than the PTFE sourced from Industrial Plastics. We swapped out the PTFE IR filters and so the PTFE IR filters used in the 2012 and 2013 observing seasons are sourced from Interplast and show negligible birefringence effects. We also started annealing PTFE in order to reduce the stresses within the material. Nylon filters show no sign of affecting the differential pointing at all.

Differential beam width for all receivers are small and do not have an observable pattern across the focal plane. Figure 4.26 shows the distribution of differential beam widths for BICEP2 and the Keck Array in 2012 and 2013. Figure 4.27, 4.28, and 4.29 shows the differential beam width across the focal plane for BICEP2 and the Keck Array in 2012 and in 2013.

While there is a large spread of per-detector ellipticities across the focal plane, each detector pair's ellipticities are relatively well matched, and so the range of differential ellipticities for each detector pair is smaller than the scatter in the ellipticities for each detector. The pattern of differential ellipticity varies from receiver to receiver; however, the spread on the measured differential ellipticities are very similar. The differential ellipticity for BICEP2 and Keck Array are still larger at the edges of the focal plane as well as around

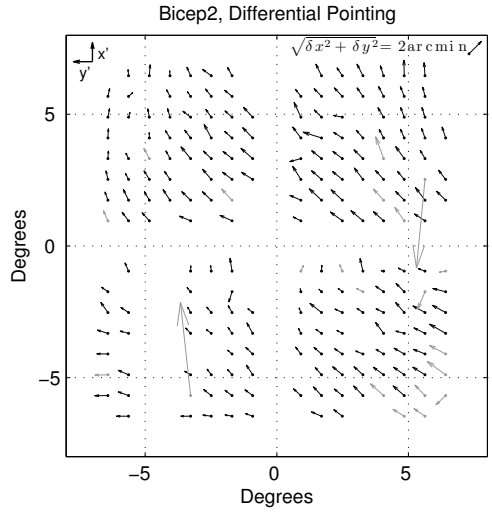

Figure 4.23: BICEP2 Differential pointing between each orthogonally-polarized detector pairs in a focal plane layout. The arrows point from the A detector's location to the B detector's location. Light colors indicate detectors that have been excluded from the final analysis. BICEP2's differential pointing mismatch shows a diagonal pattern across the focal plane. *Figure from [25].*

the edges of the tile, as shown for BICEP2 in Figure 4.30, and for the Keck Array receivers in 2012 (Figure 4.31) and 2013 (Figure 4.32).

As described in the beginning of this section, the configuration of three receivers changed between the 2012 and 2013 observing seasons for the Keck Array. Receiver 3 and Receiver 4's focal planes were completely changed, and one tile in Receiver 1 was swapped out. We can consider the consistency of the measurements of the receivers that stayed the same between the two observing seasons, which are Receiver 0 and Receiver 2, as well as three tiles in Receiver 1.

Figures 4.33, 4.34 and 4.35 shows a comparison between the beam parameters obtained from the two different observing seasons for detectors that are unchanged from one season to the other. Figure 4.33 compares the beam parameters between Receiver 0 as measured in

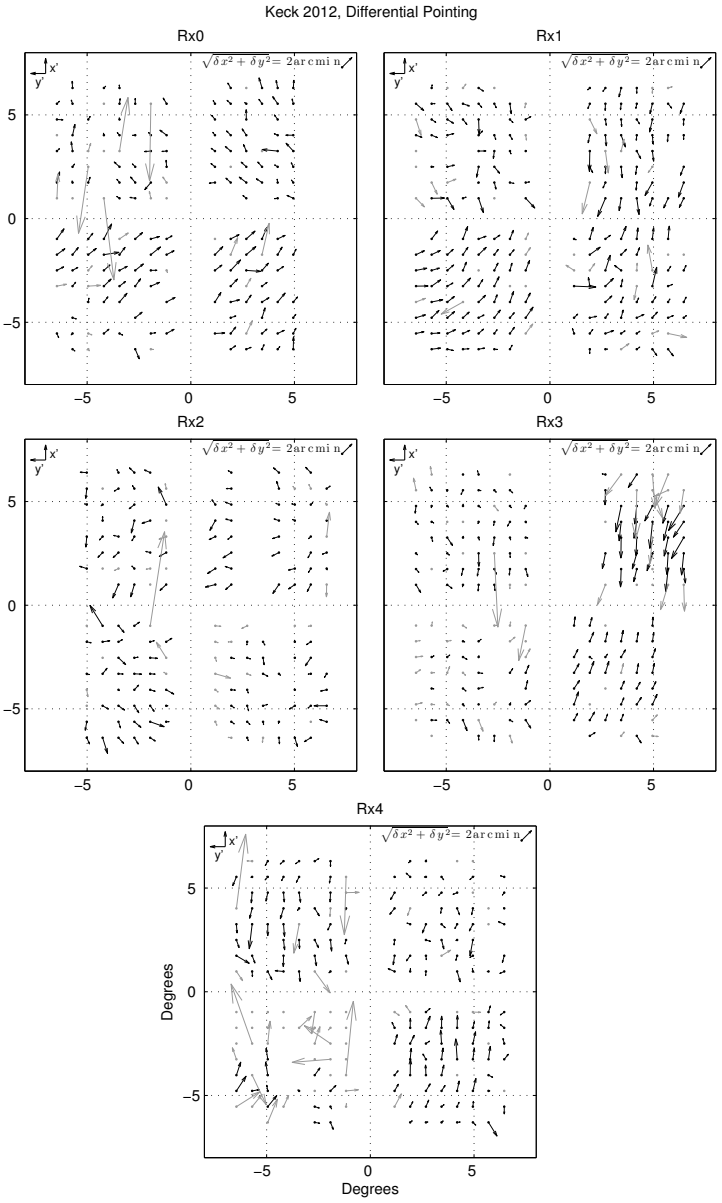

Figure 4.24: Differential pointing between each orthogonally-polarized detector pairs displayed in each of the Keck Array receivers for the 2012 observing season. The arrows point from the A detector's location to the B detector's location. Light colors indicate detectors that have been excluded from the final analysis. In general, each Keck Array receiver does not show a uniform pattern across the focal plane. Receiver 1, 3 and 4 have tiles with large X direction offsets. *Figure from [25].*

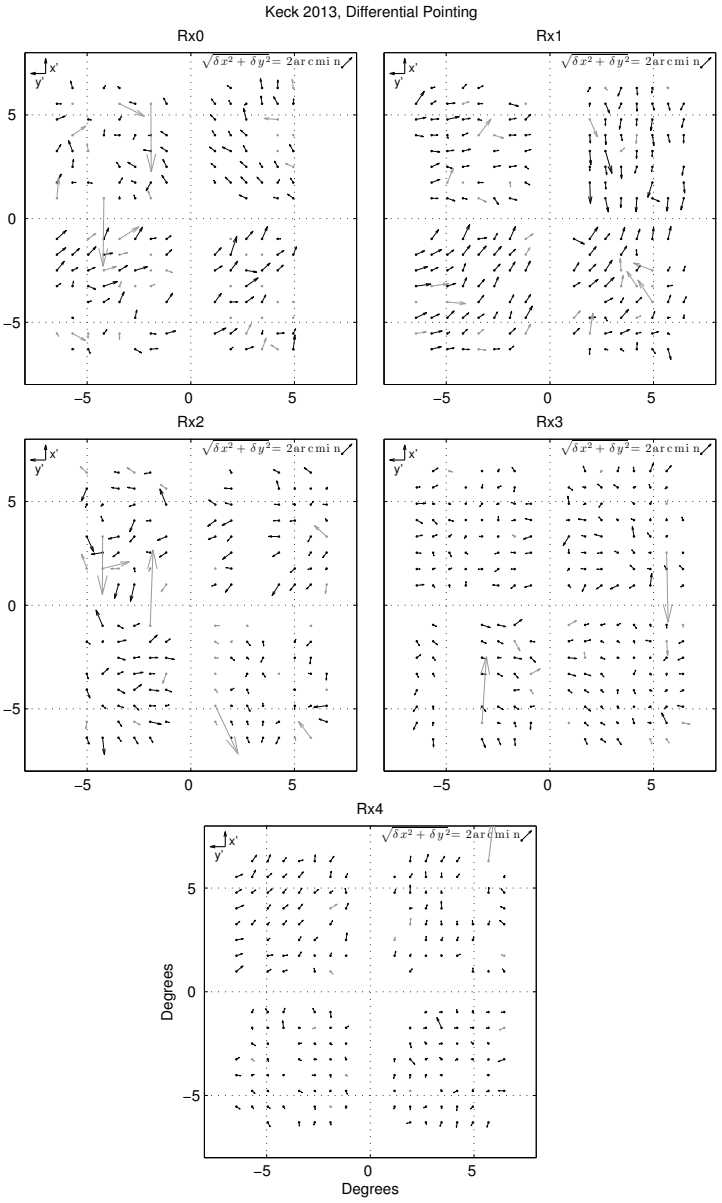

Figure 4.25: Differential pointing between each orthogonally-polarized detector pairs displayed in each of the Keck Array receivers for the 2013 observing season. The arrows point from the A detector's location to the B detector's location. Light colors indicate detectors that have been excluded from the final analysis. Receiver 3 and 4 shows much smaller differential pointing mismatches than in the other receivers or in the previous year. *Figure from [25].*

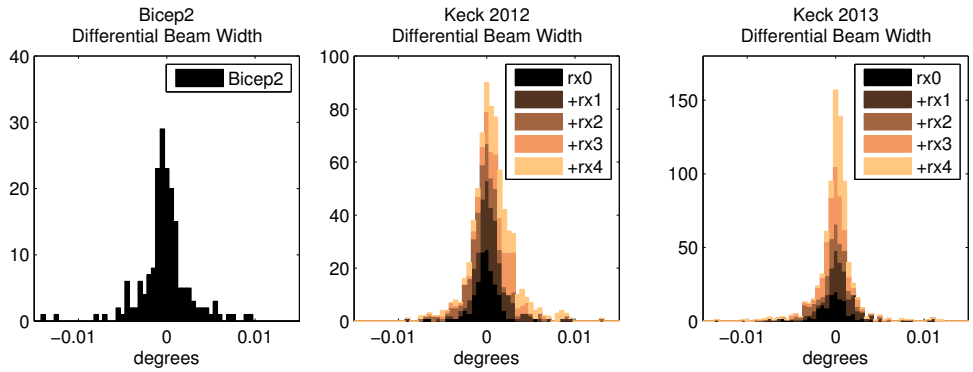

Figure 4.26: The differential beam widths for BICEP2 (left), the Keck Array in 2012 (center) and the Keck Array in 2013 (right). Measured differential beam width is small and does not show large variations for receiver to receiver. *Figure from [25].*

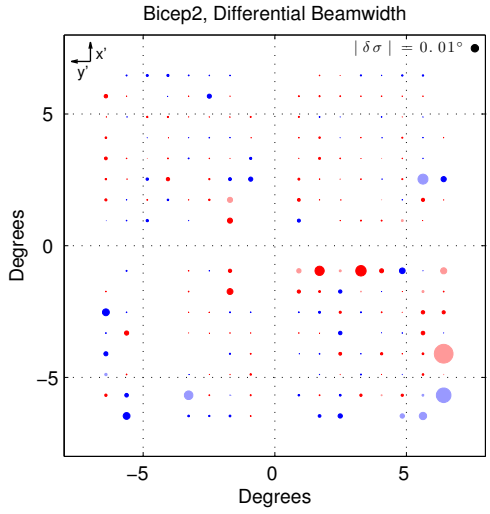

Figure 4.27: BICEP2's differential beam width plotted in focal plane layout. Blue and red indicate positive or negative differential beam width. Light colors indicate detectors that have been excluded from the final science analysis. The differential beam widths do not show a pattern across the focal plane. *Figure after [4].*

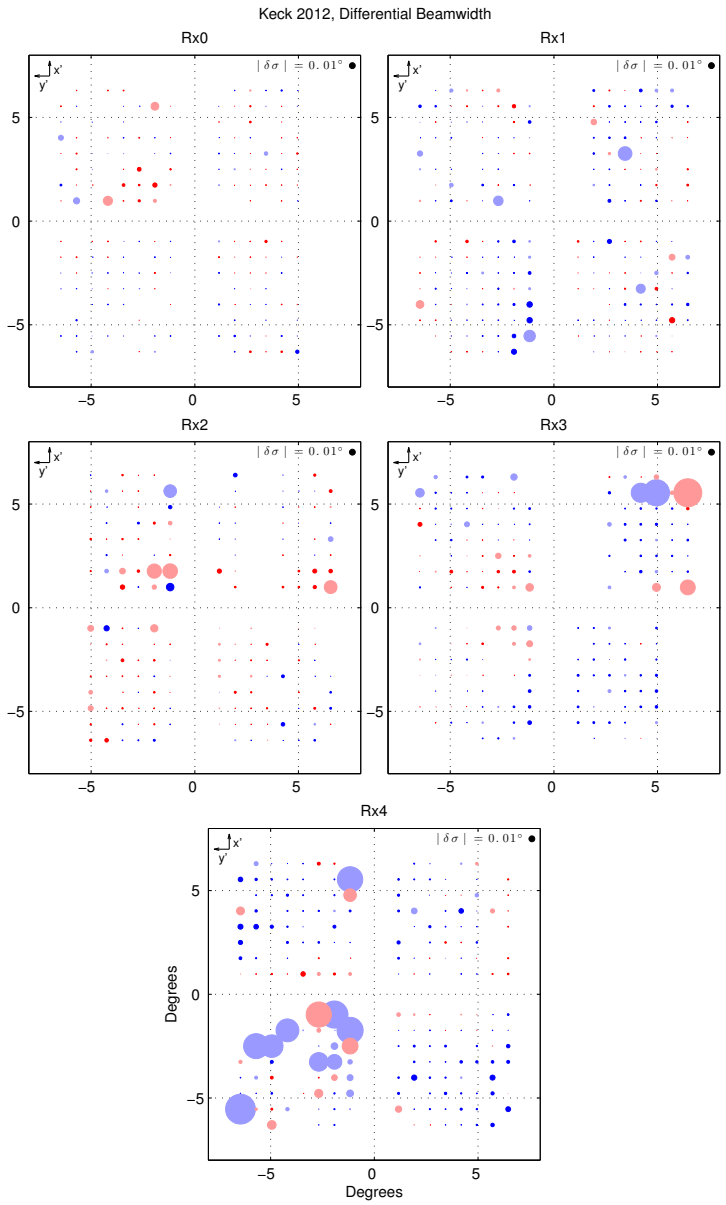

Figure 4.28: Differential beam width plotted for all receivers in the Keck Array for the 2012 observing season. Blue and red indicate positive or negative differential beam width. Light colors indicate detectors that have been excluded from the final science analysis. The differential beam widths do not show a pattern across the focal plane. *Figure after [4].*

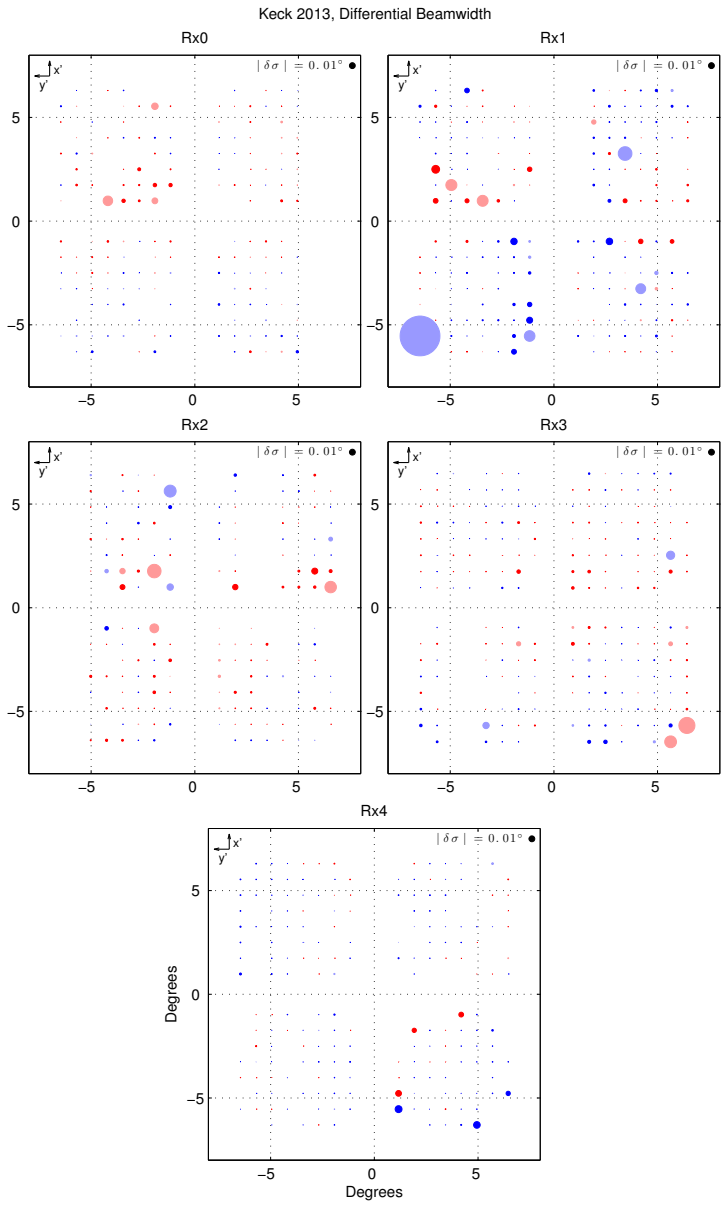

Figure 4.29: Differential beam width plotted for all receivers in the Keck Array for the 2013 observing season. Blue and red indicate positive or negative differential beam width. Light colors indicate detectors that have been excluded from the final science analysis. The differential beam widths do not show a pattern across the focal plane. *Figure after [4].*

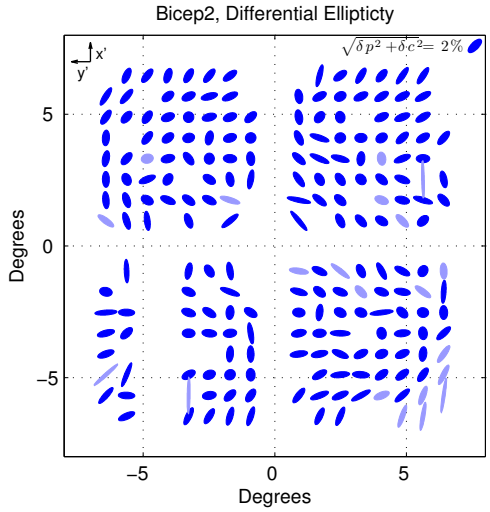

Figure 4.30: BICEP2 differential ellipticity as seen across the focal plane. The orientation of the ellipse indicates the orientation of the difference beam quadrupole. The light colored ellipses indicate detectors that have been cut from the final analysis. The differential ellipticity has been exaggerated for clarity. The differential ellipticity is higher at the edges of the tile, as well as at the edges of the focal plane. *Figure from [25].*

2012 and in 2013, Figure 4.34 compares the measurements for Receiver 2, and Figure 4.35 compares the measurements for the 3-tile subset of detectors which stayed the same in Receiver 1. The observed beam parameters are very consistent from one year to another, despite the change in source we used for mapping. The dashed lines show the median per-detector measurement error for each receiver indicating the accuracy to which we expect the correlation to be. For the most part, the correlation between measurements in 2012 and 2013 are within the expected errors, except for differential pointing. There appears to be higher scatter in the correlation between the measured differential pointing in 2012 and 2013 for all three receivers despite the high accuracy with which we measured the differential pointing. Nonetheless, it is reassuring to note that the measurements of the beam parameters in different years for the same detectors are very well correlated.

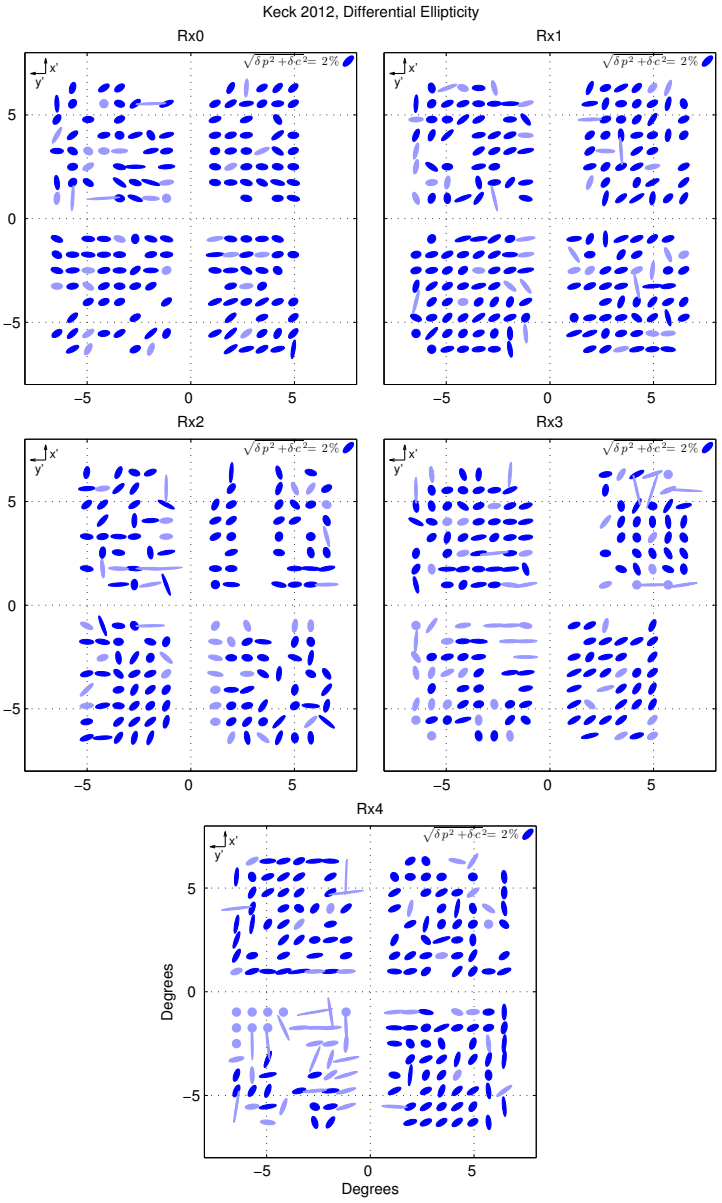

Figure 4.31: Differential ellipticity as seen for all receivers in the Keck Array for the 2012 observing season. The orientation of the ellipse indicates the orientation of the difference beam quadrupole. The light colored ellipses indicate detectors that have been cut from the final analysis. The differential ellipticity has been exaggerated for clarity. The differential ellipticity is higher at the edges of the tile, as well as at the edges of the focal plane. *Figure from [25].*

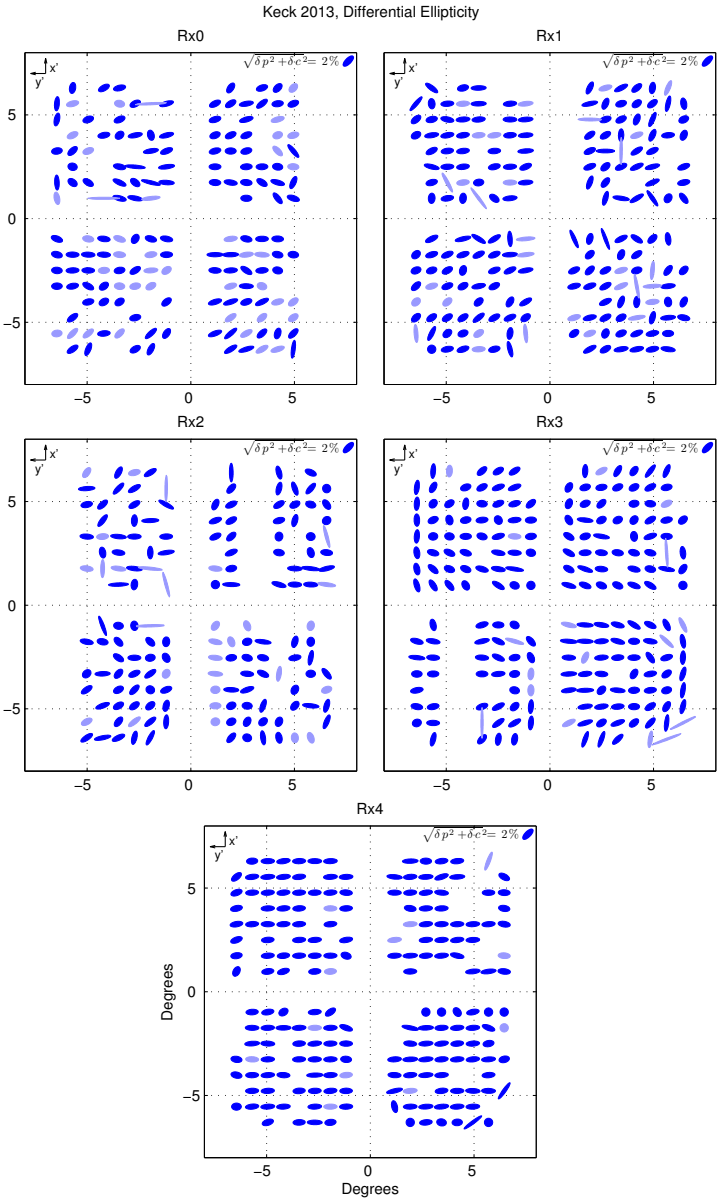

Figure 4.32: Differential ellipticity as seen for all receivers in the Keck Array for the 2012 observing season. The orientation of the ellipse indicates the orientation of the difference beam quadrupole. The light colored ellipses indicate detectors that have been cut from the final analysis. The differential ellipticity has been exaggerated for clarity. The differential ellipticity is higher at the edges of the tile, as well as at the edges of the focal plane. *Figure from [25].*

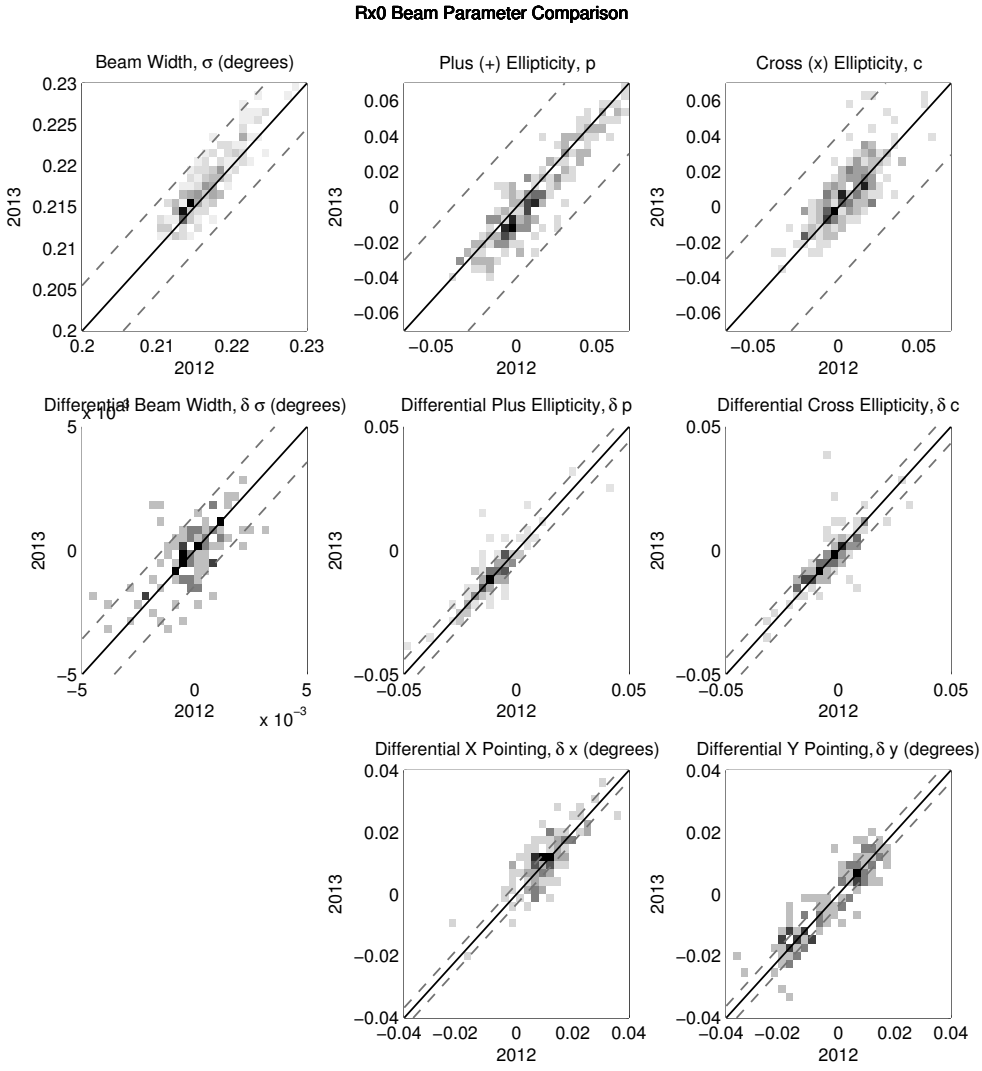

Figure 4.33: A comparison of the beam parameters measurements between 2012 and 2013 for Rx0. The solid line has a slope of 1, while the dashed lines indicate the median per-detector measurement error. All beam parameters and differential beam parameters are measured to be the same (within errors) in the two different years.

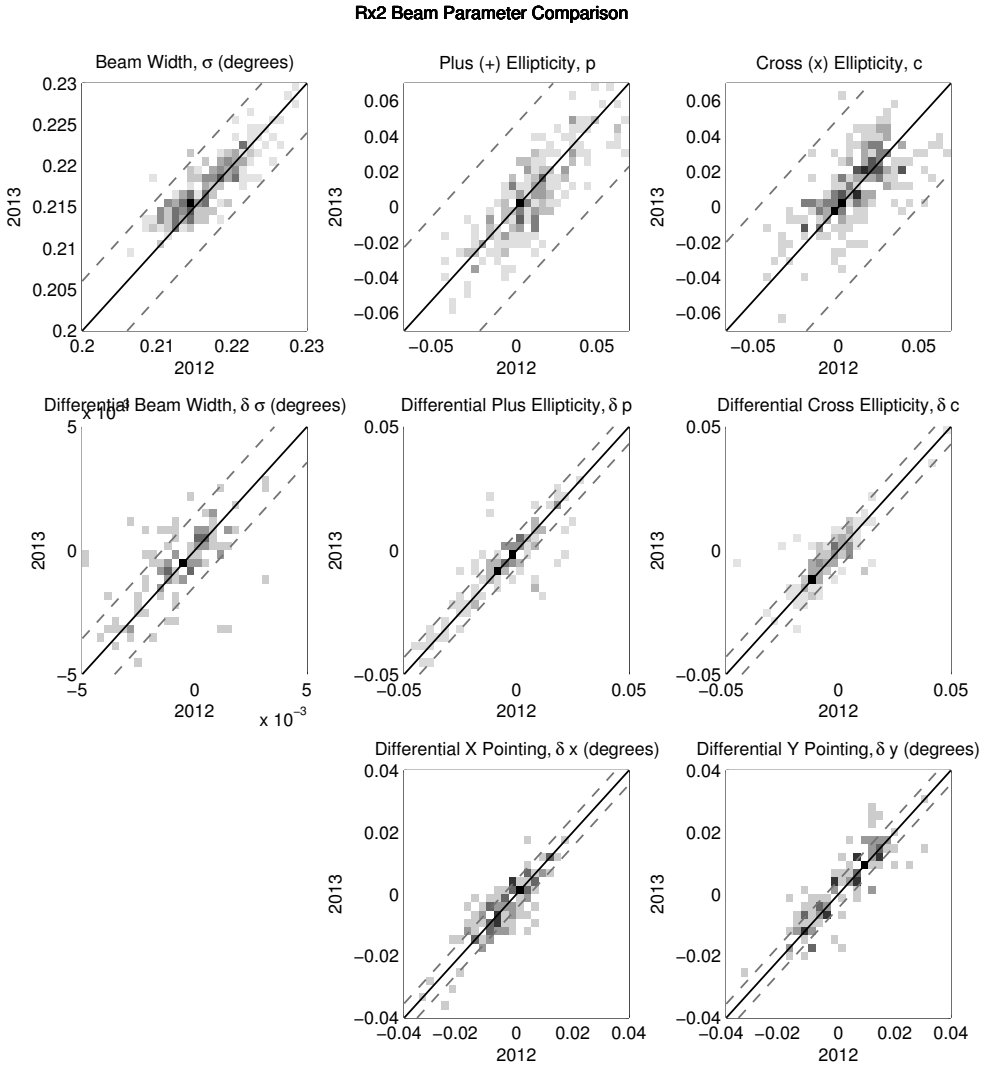

Figure 4.34: A comparison of the beam parameters measurements between 2012 and 2013 for Rx2. The solid line is a line with a slope of 1, while the dashed lines indicate the median per-detector measurement error. All beam parameters and differential beam parameters are measured to be the same (within errors) in the two different years.

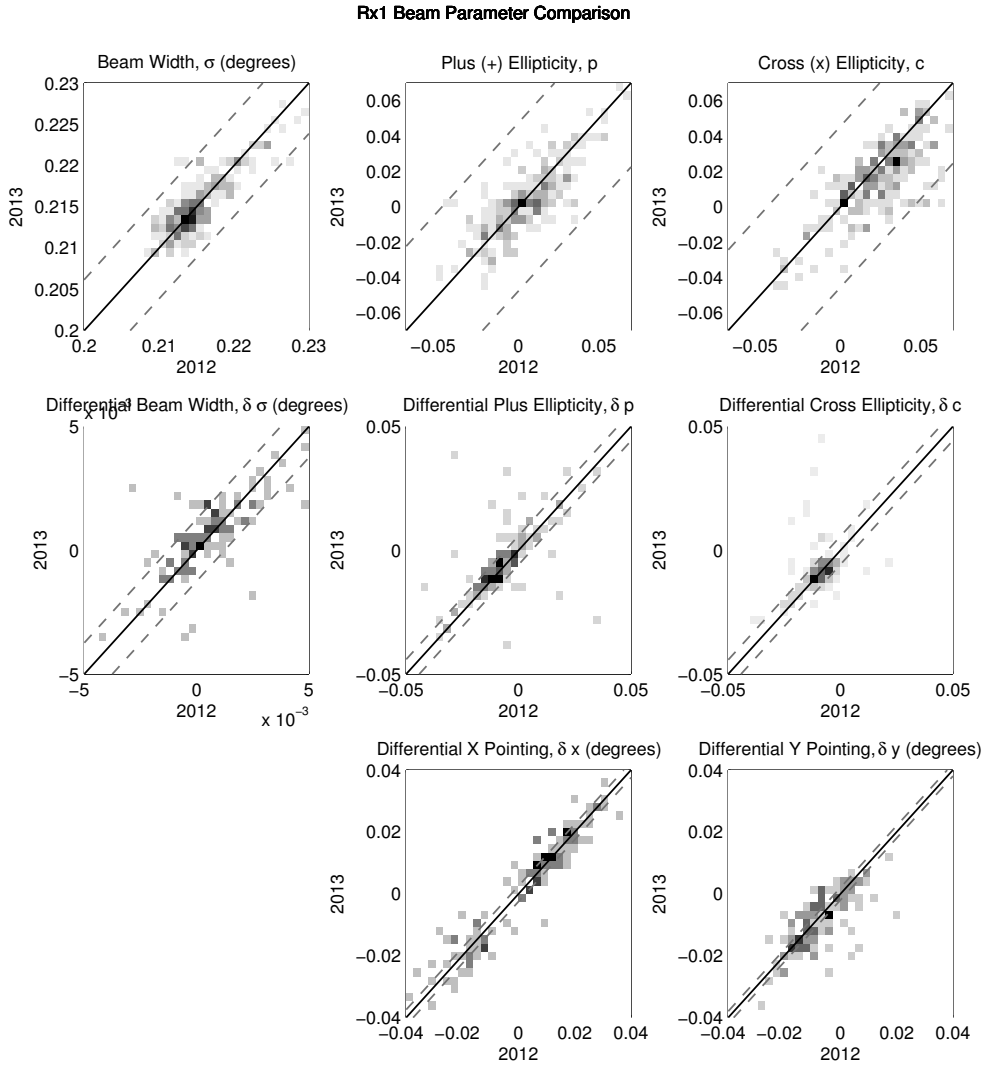

Figure 4.35: A comparison of the beam parameters measurements between 2012 and 2013 for the detectors in Rx1 that did not change between the observing seasons. The solid line is a line with a slope of 1, while the dashed lines indicate the median per-detector measurement error. All beam parameters and differential beam parameters are measured to be the same (within errors) in the two different years.

Since we placed BICEP2's focal plane into Receiver 3 in 2012, we should be able to compare the measured beam parameters. We note that the beam widths for this focal plane in Receiver 3 looks smaller than the beam widths for this focal plane measured in BICEP2. Interestingly, the differential pointing parameters have also become smaller when the focal plane was placed in Receiver 3, but still show a correlation. The optical design for BICEP2 and the Keck Array are very similar in the shape of the lenses and the expected focus. However, BICEP2's objective lens was placed 10 mm lower than in the Keck Array. This is theorized to account for the lower beam widths in Keck Array, and perhaps also the lower differential pointing in Receiver 3. Looking at the differential pointing correlation, it does seem that the far field differential pointing is caused by some interaction between the optics of the instrument and the existing near field differential pointing. A change in the focus of the telescope results in a change in the magnitude of the far field pointing mismatch, but still shows a correlation in the pattern.

Fitting our beams to an elliptical Gaussian allows us to quickly understand the characteristics of the beams in all the detectors. We use these beam parameter fits in the channel cuts, and remove beams that are too wide, or have too large a value of differential beam widths or differential ellipticity.

4.3 Further optical characterization

4.3.1 Ghost Images

Since the far field beam maps extend across the range of the entire focal plane field of view, for each detector, we map the response of the beam far outside the angular extent of

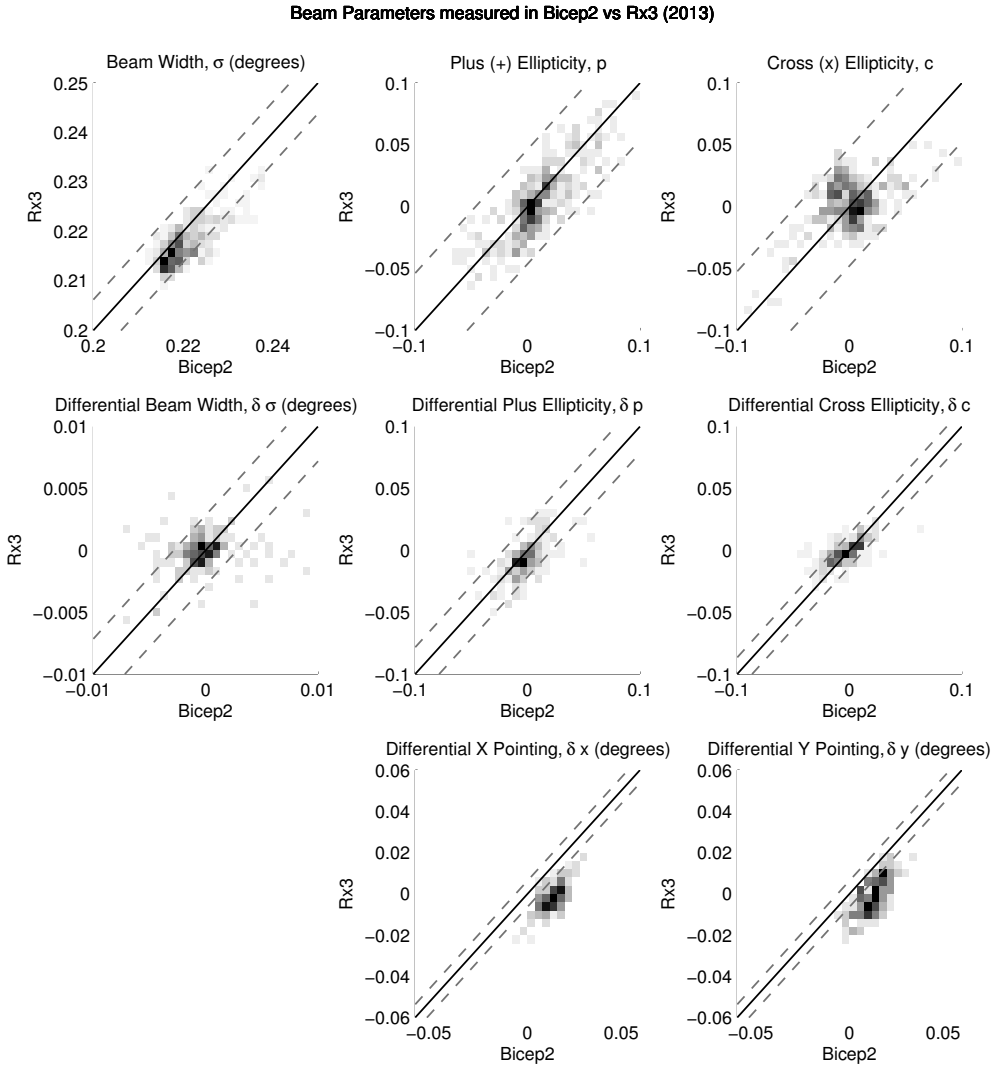

Figure 4.36: A comparison of the beam parameters measurements between BICEP2 and Receiver 3 in the Keck Array for 2013. The solid line has a slope of 1, while the dashed lines indicate the median per-detector measurement error. A difference in the placement of the objective lens between BICEP2 and the Keck Array is theorized to explain the difference in the beam widths and differential pointing between the two measurements.

the main beam. This allows us to notice ghost beams which are reflections of the incoming radiation on the 50K IR filters and back out onto the sky. These reflected beams appear on the mirrored position of the detector around the boresight.

We anti-reflective coat all the optical elements in the line of sight with the exception of the window in order to reduce the amount of ghost beam reflections. However, the reflectance off the window foam is small. This anti-reflective coating reduces the amplitude of the ghost beams, ensuring a low level of contamination in the timestream of the detector.

The amplitude of the ghost beams is estimated to be $\sim 4 \times 10^{-4}$ of the amplitude of the main beam for BICEP2, and the beam width is twice the beam width of the main beam. On the whole, the various differential beam systematics are worse in the ghost beam, but the amplitude of the ghost beam is small. A simulation of the temperature to polarization leakage has been studied and is further explained in [24] and found to be almost negligible.

4.3.2 Sidelobes

We would like to understand the far sidelobe response of our detectors. While we do mitigate and control the response of our detectors at large angles with the forebaffle and groundshield, we would like to understand if the far sidelobes are strong enough to pick up extraneous contamination from external sources such as emission from the ground, the galaxy or the moon.

The far sidelobe response is much smaller than the response of the main beam, and as such, we use high powered sources like the Broad Spectrum Noise Source (BSNS) to map the response of the far sidelobes. The BSNS consists of a $50\ \Omega$ resistor connected to microwave amplifiers and multipliers. The BSNS has two attenuators to control the ampli-

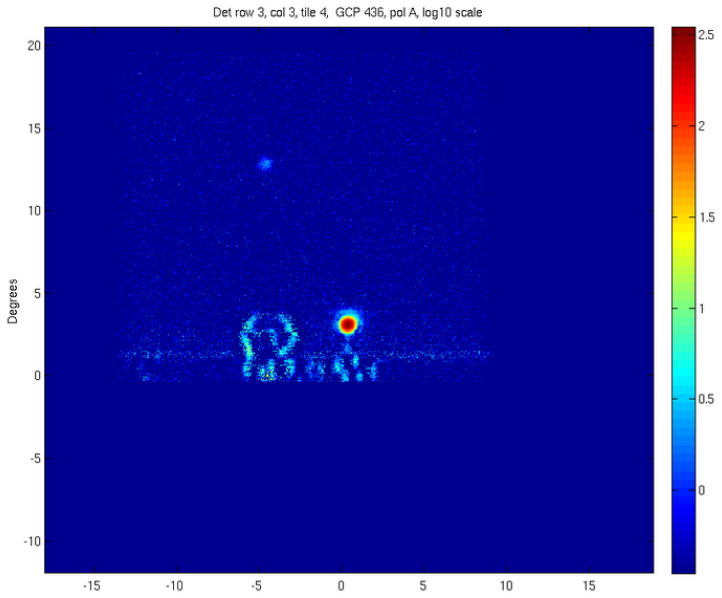

Figure 4.37: An example of a ghost beam in the far field. The ghost beams are reflections off incoming radiation of the 50 K IR filters back onto the sky, and appear on the mirrored position of the detector around the boresight.

tude of the signal. A bandpass filter that restricts the output frequency to the frequency of interest (140-160GHz). The BSNS is a linearly polarized source. We do occasionally use a circular polarizer on the end of the source in order to allow both orthogonally polarized detectors to see the source.

For far sidelobe mapping, we place the source on the mast that is on the same building as the telescope that is about 10m away. This close to the telescope, the masts are easily above the height of the groundshield and we do not need to use the far field flat mirror in order to see it. We are able to map the very faint far sidelobe responses using a highly amplified setting. This setting unfortunately saturates when in the main beam. We take data at multiple attenuation settings in order to understand the wide angle response of the beam with respect to the gain of the main beam. For BICEP2, we note that there are no sharp features in the sidelobes, although the Keck Array receivers do demonstrate some ring-like sidelobe structure.

Much of the power in the sidelobes are truncated at the forebaffle, which is designed to intercept radiation at angles $> 15^{\circ}$. Integrating the power in the beam profile, we find that for BICEP2, the total integrated power is 0.1% outside 25° from the main beam [24, 4].

We map the sidelobes of BICEP2 and the Keck Array with and without the forebaffles on to ensure that we are correctly understanding the power outside the beam. For BICEP2, the power intercepted by the forebaffle is 0.7% consistent with the measured forebaffle loading of $\sim 3\mathrm{K}_{\mathrm{CMB}}$ [24].

4.3.3 Polarization Angle Measurements

In order to be able to measure the polarization of the CMB, we must first determine the polarization angle, ψ and the cross-polarization response, ϵ of our detectors. The accuracy to which we determine the absolute polarization angle of our detectors directly impacts the accuracy to which we measure E-mode and B-mode polarization of the CMB. An error ($\Delta\psi$) in the orientation of the detector pairs will result in the leakage of E-mode polarization to B-mode polarization by a fraction of $\sin 2\Delta\psi$ [65].

Following [65], we find that an induced BB spectra is $\sin^2 2\Delta\psi$ times the EE power spectrum, thus giving us a limit on the accuracy with which we are expected to know the polarization angle of our detectors. We require the error on the polarization angle to be $\Delta\psi < 0.7^\circ$ if we would like the induced BB spectra to be at a level of $r < 0.01$. Measuring the EB and TB power spectrum requires a more stringent limit on $\Delta\psi$, since false power leaked into the EB or TB spectrum only depends on $\sin 2\Delta\psi$ giving us a constraint on $\Delta\psi < 0.2^\circ$.

We use a self-calibration method [40] that estimates the overall rotation angles of the detectors by minimizing the EB and TB spectra. We then apply this overall rotation to our detectors in the analysis.

The cross-polarization response, ϵ, defined to be a polarized detector's response to orthogonally polarized radiation, directly informs the polarization efficiency, $\frac{1-\epsilon}{1+\epsilon}$ [65] of the detectors. A pair of detectors which are not orthogonal to each other affects the amplitude scaling of the power spectrum but does not produce inaccurate polarization patterns. In [65], we find that the cross-polarization response ϵ has to be better than ± 0.026 in order to ensure that the amplitude of the power spectrum is at least 10% accurate. For BICEP2 and

Keck, the cross-polarization response ϵ has to be $\sqrt{10}$ smaller, that is 0.8%.

In order to determine the polarization angle of our detectors, BICEP2 used two methods. A dielectric sheet calibrator (DSC) was placed above the window at an angle. As the telescope was rotated around the boresight, the DSC was held fixed, and the response of detectors to incoming radiation that transmitted and polarized through the dielectric sheet is modulated. A more thorough discussion of the DSC can be found [4, 25].

We also use a rotating polarized source in the far field. The rotating polarized source[13] consists of the BSNS placed on a rotating stage. The BSNS is linearly polarized, but in order to ensure more stringent linear polarization, there is a wire grid placed on the rotating stage in front of the BSNS. A tiltmeter was placed parallel to the face of the wire grid in order to allow for the leveling of the source when the source was placed on the mast. We place the rotating polarized source on the mast on the building 200m away. Since this measurement is a far field measurement, we use the far field flat mirror above the receivers.

The measurement is made by setting the source to a particular polarization orientation, and then rastering across the source to make a beam map for a row of detectors at a time. The elevation step size is 0.2°. We thus map the polarization response for every detector that falls in that area of the map for a given orientation of polarized light. We then rotate the source polarization angle in 15° steps, for a full 360° rotation mapping the response of the detectors at every step. This is to ensure that any source amplitude drifts are on longer time scales, allowing us to measure the response of the detectors to radiation at various polarization angles accurately. When the source is rotated back to its starting position, we move on to map the next row of detectors. This method allows us to map the response of each detector to radiation that is polarized at various angles from the polarization of the

detector.

We obtain the detector's response to the angle of polarized light by fitting an elliptical Gaussian to each map at each source position. The polarization response of each detector for each angle is then fit to a five-parameter model described as

$$A\left(\cos(2(\theta+\psi))-\frac{\epsilon+1}{\epsilon-1}\right)(C\cos(\theta+\phi)+1) \tag{4.12}$$

where θ is the angle of the source, ϵ is the cross polar response, ψ is the polarization angle of the detector, A is the amplitude of the source, C and ϕ are the amplitude of a cross collimation term.

The cross polar response of BICEP2 is $\sim 0.4\%$. This is well within the limit needed to ensure that the amplitude of the power spectrum is accurate to 10%. While the analysis for Keck is in progress, since the detector technology used in BICEP2 and the Keck Array are similar, we expect that the cross-polar response of the Keck Array detectors will be about the same as for BICEP2.

Chapter 5

Residual Temperature to Polarization Leakage

IN SEARCHING FOR THE FAINT B-MODE POLARIZATION signal from inflation, we must not only maximize the sensitivity of the instrument, but also ensure that the systematics of the telescope are well enough controlled and understood in order to trust that the signals we detect are real and not falsely induced. Since we detect polarization by differencing the signals from two orthogonally polarized detectors, any mismatches in the performance of either detector in the pair will result in a false polarization signal, even when there is no input polarization signal. We must be careful that the behavior of these detectors are well-matched enough so that any mismatches do not induce a false signal that overwhelms the B-mode polarization signal that we are searching for.

My work has been primarily concerned with the beam systematics of BICEP2 and the Keck Array, and how the beam response of the detectors governs the performance of the

telescope. This chapter is primarily focused on the beam systematics of BICEP2 and the Keck Array, and the level of induced temperature-to-polarization leakage by the beams. Since BICEP2 and the Keck Array detect polarization by differencing the signal in a pair of co-located orthogonally polarized detectors, any mismatch in the response of the two detectors will induce a polarization signal even when the incoming radiation is unpolarized. The optical response of the detectors is largely governed by the beam shape of the detectors, and so any difference in the beam shapes of each detector in a pair of co-located orthogonally polarized detectors will leak the temperature signal into the polarization signal. We defer the broader discussion on the telescope systematics in general to [24].

The degree of induced false polarization signal is determined by the strength of the non-polarized anisotropy, as well as the level of imperfections of the telescope. The CMB temperature is uniform to a level of 1 in 10^{-5}. The CMB E-mode polarization is 10 times lower than the amplitude of the CMB temperature anisotropy. The B-mode polarization signal at a tensor-to-scalar ratio, $r = 0.1$ is a factor of 10 smaller than the level of E-mode polarization. Since the temperature anisotropy of the CMB is so much higher than that of the expected polarization signals, we must be careful to ensure that the systematics of the telescope are low enough to not induce a temperature-to-polarization leakage signal that is large enough to overwhelm the faint B-mode polarization signals we are looking for.

We parameterize our beam using an elliptical Gaussian and, for the most part, the main mismatch modes are captured relatively well with this approximation (See Chapter 4). Using this parameterization, we are able to predict the temperature-to-polarization leakage from the main beam mismatch modes. As we will discuss in this chapter, the leakage from the main beam mismatch modes is well understood and can be removed in the analysis.

However, as discussed in the Chapter 4, not all the power in the beam is captured by the elliptical Gaussian beam fit. In this chapter, we study leakage induced by the higher order beam mismatches.

We take advantage of the fact that our telescope is a small-aperture telescope with a relatively close far field to make detailed, high signal-to-noise maps of each detector's beam response using thermal and amplified microwave sources on the ground in order to characterize our beams. Using these deep maps, we strive to fully understand the higher-order features in the beams and how they affect the temperature to polarization leakage by using them in our simulation pipeline. We start with a description of the simulation pipeline, in order to facilitate the discussion on using the beam maps in a simulation to predict the temperature to polarization leakage. We then discuss the results of the leakage predicted by simulation, and try to understand the residual temperature-to-polarization leakage from the residual beam mismatches.

5.1 Data Analysis Pipeline

We start with a description of the analysis pipeline that is used in BICEP2 and the Keck Array analysis, which is critical to understanding the temperature-to-polarization leakage that is predicted from the beam systematics in the telescope. The simulation pipeline is built in order to generate timestreams that behave like the detectors during CMB observations. We then run the simulated timestreams through the analysis pipeline that takes both the real and simulated timestreams and turns them into maps from which we then extract power spectra and the final results.

5.1.1 Observation schedules

A thorough description of the observing schedules for BICEP2 can be found in [1, 2]. The building blocks for BICEP2 and Keck Array observing schedules are constant elevation scans. A half-scan is a single raster $\sim 60^\circ$ in azimuth at constant elevation. The scan speed is 2.8° per second, slower at the beginning and the end of the scan, as the telescope ends a raster and begins the next. A scanset is ~ 45 minutes long and consists of 53 scan repetition, going back and forth in azimuth at constant elevation. Before every scanset, an elevation nod (elnod) which moves the telescope up in elevation by 0.6°, down in elevation by 1.2°, and up again in elevation by 0.6° is performed. The elnod is used to measure and calibrate the gain of each pixel for a given change in airmass as well as to remove detectors that show anomalous behavior. The elnod is followed by a partial load-curve, where the detectors are heated until they are warm enough to be non-superconducting and the bias voltage is slowly lowered in steps to the operating bias. The end of the scanset is bracketed by an elnod moving downwards, upwards, then downwards and another partial load curve. A set of 10 scansets at 0.25° steps in elevation for each scanset make up a 9 hour phase for CMB observations, while a set of 7 scansets make up a 6 hour phase for galactic plane observations.

The observation cycle of BICEP2 and Keck Array is set by the sub-Kelvin refrigerator hold time. BICEP2 used a schedule of phases that repeated every three days, whereas Keck Array's schedule repeated every two days. Each schedule was taken at a single boresight angle, called the deck angle. For all three seasons of BICEP2 observations, and for the Keck Array observing season in 2012, we used 4 different boresight angles (68° , 113° , 248° , and 293°). Two boresight angles separated by 45° are sufficient to measure both Q

and U on the sky. The other two sets of boresight angles offer redundancy as well as an automatic reduction of systematics that have a 180° symmetry. Keck Array 2013 increased the number of boresight angles to eight, (68°, 113°, 248°, 293°, 158°, 203°, 338°, and 23°). The increased number of boresight angles now includes boresight angles separated by 90° in order to reduce systematics induced by monopolar beam mismatches [24].

5.1.2 Data reduction and analysis

A more thorough discussion of the data reduction pipeline can be found in [2].

The raw timestream data from the South Pole is transferred to the North, and then low-level reduction on the data is performed. The low-pass filter that is applied to the data is deconvolved, and glitches in the data are flagged and removed. The gain for all the detector timestreams are roughly calibrated to be the same using the elnods. The absolute gain calibration is performed against the Planck 143 GHz temperature map once as much data has been accumulated as possible. The "round one" data cuts are applied to remove glitches, flux jumps, and irregularity in the data.

For each pair, the timestreams are summed and differenced. The pair-sum timestreams are used to make temperature maps, and the pair-diff timestreams measure the polarization. Pair-differencing the timestreams up front allows us to reduce the effect of atmospheric fluctuations. The timestreams are then filtered with a third-order polynomial as well as a template of ground-synchronous signals in order to reduce contamination from fluctuations that vary across large scales. This also removes the sensitivity of the telescope to fluctuations at large scales. Each forward and backward halfscan is filtered separately.

The pointing of the telescope is calibrated against the Planck 143 GHz template in a

process similar to that which determines the absolute calibration of the telescope. The pointing calibration is made for each deck angle, for left-going and right-going scans separately, and we find that the absolute pointing uncertainty is 0.05° [42].

5.1.3 Making Maps

Once we have the pointing information for each detector pair, we can now make maps. We bin the timestream data for each detector pair from a scanset into maps that have square pixels that are 0.25° wide at the center of the map. The timestream data from each scanset is inverse-variance weighted before being added into per-pair maps. We make pair-sum and pair-difference maps, where pair-sum maps measure the temperature anisotropy, and where the pair-difference map measures the polarization. The pair-difference maps take the polarization angle orientation into account to make Q and U maps. These per-pair maps are made for every scanset of data taking and saved on disk to allow the possibility of permuting the final coadded maps.

A second round of cuts (round two cuts) is implemented at the coadd stage, at which we coadd all per-pair maps into final maps. These cuts are made of various parameters such as the skewness, stationarity, the value of the elnod calibration (an indication of weather), the temperature of the focal plane and various other measures of good data. The channel cuts are also applied here. These channel cuts exclude poorly performing channels. The beam parameterization obtained using far-field beam map calibration is used in determining the channel cuts, as are the pointing error and relative gain.

Once the second round cuts and the channel cuts have been made, we coadd the pairmaps from every detector pair in a phase into a phase map. These phase maps are then coadded

in various combinations to make final coadded maps as well as jackknife maps.

5.1.4 Jackknives

One of the most powerful tests we have is the "jackknife" tests. To make a jackknife map, we split the data into two halves with equal weights, and then difference the two halves. The data splits are designed to isolate potential sources of temperature-to-polarization leakage, either from external sources (like the ground) or from internal telescope systematics. In any jackknife, real signal should be completely differenced leaving only noise in the maps. Any false signals visible in only one half of the map will be enhanced. A jackknife test "fails" when it shows a signal.

For BICEP2 and the Keck Array, we have fourteen jackknife tests. I briefly describe them here, but full descriptions can be found in [2, 24]. The temporal-split jackknife splits the data between data taken in the first and second half of the observing season. The azimuth jackknife halves the data depending on the azimuth position that the telescope is observing at, while the moon jackknife isolates times at which the moon is up or down. The deck jackknife and the alt-deck jackknife splits the data taken at various deck angle combinations.

For studying the beam systematics, the detector subset jackknifes are the jackknifes that we are most interested in. These include the tile jackknife, which splits the data taken for detectors in tile 1 and 3 from the data taken by detectors in tile 2 and 4. The tile jackknife explores the difference between the beam shapes for half the tiles in the focal plane. The tile inner/outer and tile top/bottom jackknives split the data taken from detectors based on their positions in the tile. The focal plane inner/outer jackknife splits the data taken

from detectors at the inner part of the focal plane and detectors at the outer part of the focal plane. The tile inner/outer, tile top/bottom, and focal plane inner/outer jackknives are very sensitive to differential ellipticity, as well as any other aberrant beam effects that vary across the focal plane.

The mux row and mux column jackknifes probe systematics that are related to the multiplexing system. The mux row and mux column jackknifes are sensitive to contamination from various cross-talk effects that affect the detectors. The tile/deck jackknife tests for effects that come from observing the sky at a particular detector orientation.

A jackknife that particularly targets the differential pointing mismatch is the differential pointing best/worst jackknife. Maps made with detectors with the smallest differential pointing are compared to maps made with detectors with the largest differential pointing mismatch. If the differential pointing is not mitigated well enough, this jackknife will fail. Finally, while the deck and alt-deck jackknives are not a detector split jackknives, these jackknives split the data into maps made with deck angles that are 180° rotated from each half, which exacerbates the differential pointing temperature-to-polarization leakage. A failure of both these jackknifes will make it obvious that the differential pointing in the beams are contaminating the data.

5.1.5 Power Spectra

Once the maps are made, we can calculate power spectra, which are measurements of power at specific angular scales. Starting from temperature (T), and polarization (Q and U) maps, we start by apodizing, then Fourier-transforming the maps. The Q and U Fourier-transformed maps are mathematically transformed to make E and B transforms using the

following equation [58]:

$$E(\vec{\ell}) = Q(\vec{\ell})\cos(2\phi_{\vec{\ell}}) + U(\vec{\ell})\sin(2\phi_{\vec{\ell}}) \tag{5.1}$$

$$B(\vec{\ell}) = -Q(\vec{\ell})\sin(2\phi_{\vec{\ell}}) + U(\vec{\ell})\cos(2\phi_{\vec{\ell}}) \tag{5.2}$$

where $\phi_{\vec{\ell}}$ is the angle in the transformed map and $Q(\vec{\ell})$ and $U(\vec{\ell})$ are the transforms of the Q and U maps. We multiply the appropriate transformed maps to obtain 2-dimensional Fourier-transforms of TT, TE, EE, BB, TB and EB. To obtain power spectra, we then take the mean of an annulus corresponding to the angular scale that we are interested in.

Figure 5.1 shows the T, Q, and U maps that have been made for BICEP2. Here we show the maps made using the non-jackknifed accumulated CMB data in the left column, and the maps made for the temporal-split jackknife on the right column. The maps are discussed further in Section 6.1.

Figure 5.2 are BICEP2 E-mode and B-mode maps made from filtering and transforming the Fourier space maps of E and B. The maps have been filtered to only show structure for $50 < \ell < 120$. The left column shows the BICEP2 signal, while the right column is the E-mode and B-mode maps shown for a simulated signal + noise sky with no inherent B-mode polarization.

The process of separating the Q and U maps into E and B maps is complicated by the fact that we do not map the entire sky, and our data has had various filtering processes applied, all of which result in a mixing of E to B signals. This mixing can easily overwhelm the expected B-mode signal that we are hoping to measure, and to minimize the B-mode contamination as much as possible, we use a matrix purification method in order to cleanly separate the E-modes from the B-modes [66, 2].

Once we have the power spectra, we remove the noise bias from the spectra (noise-

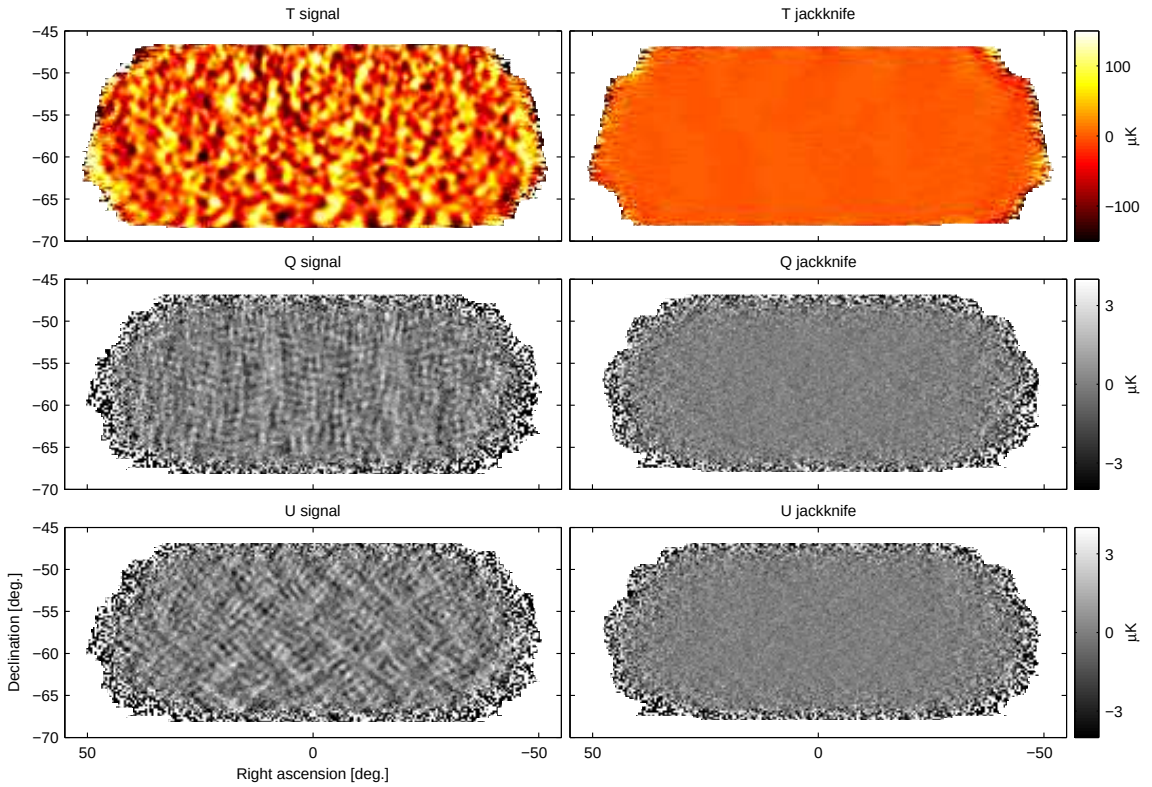

Figure 5.1: BICEP2's T, Q, and U maps. The left column shows signal maps, and the right column shows the temporal jackknife map split of the first and second half of the season. The jackknife maps are clean and show no contamination. The Q and U patterns are dominated by E-mode polarization in the CMB sky. *Figure from [2].*

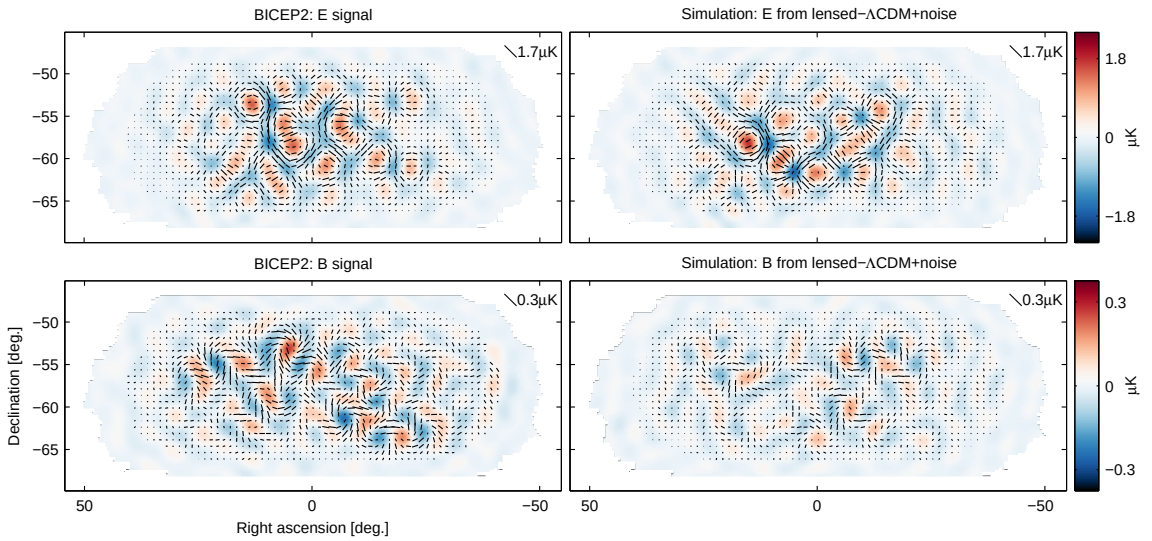

Figure 5.2: BICEP2's maps of E-mode and B-mode polarization. The maps have been filtered to only show structure for $50 < \ell < 120$, and are made from Fourier transforms of the Q and U maps. The left column shows the BICEP2 signal, while the right column is the E-mode and B-mode maps shown for a simulated signal + noise sky with no inherent B-mode polarization. *Figure from [2].*

debias) by subtracting the mean of the signal+noise simulations. We also apply the filter-beam correction to the spectra to account for the beam suppression. The noise debias and filter beam correction function are generated from the simulations. The filter-beam correction comes from the shape of the beams as it modulates the signal that we observe, while the noise debias subtracts from all spectra (simulation and observed CMB data) the effect of noise in the maps.

We generate spectra from the fully coadded maps, as well as the jackknife maps. Figure 5.3 shows the power spectra that we obtain from the BICEP2 maps (black points). We evaluate all six TT, TE, EE, BB, TB, and EB spectra. The solid red lines indicate the spectra predicted by standard ΛCDM-cosmology (including lensing). The dashed red line indicates a tensor mode at $r = 0.2$. The blue points are jackknife spectra for a single jackknife (the temporal-split jackknife). The error bars are obtained from the signal+noise simulations described in Section 5.2. Also noted in the figure are the probability to exceed values (PTE) evaluated against the simulations of standard ΛCDM-cosmology. The BICEP2 spectra is further discussed in Section 6.2.

5.1.6 Deprojection

The analysis pipeline includes a method of mitigating the temperature to polarization leakage from main beam mismatch modes [2, 24, 4, 60] from the CMB data, which is called "deprojection." Our beam systematics, particularly the differential pointing of the detectors as measured in Chapter 4, already induce a temperature-to-polarization signal large enough to overwhelm the faint B-mode polarization signal. While the observing strategy does play a role in mitigating the beam systematics, we need to be able to remove as much of the

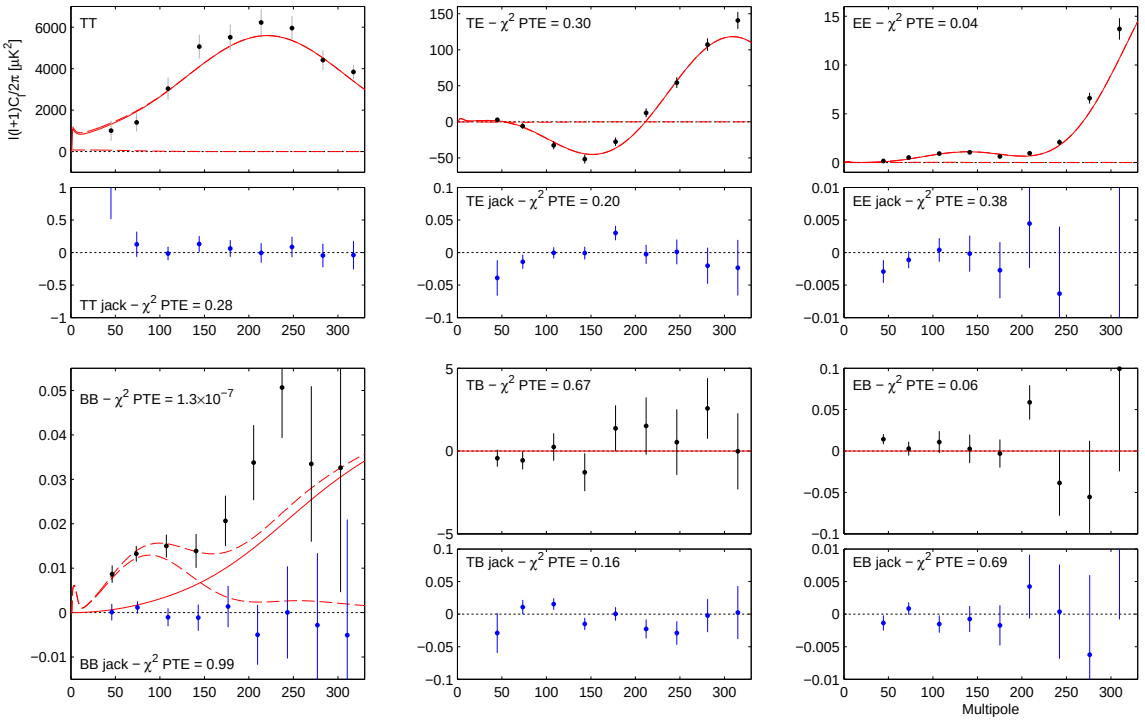

Figure 5.3: BICEP2 power spectra. The black points indicate the CMB power spectrum after the filter-beam correction and noise debias has been applied. The blue points are spectra taken from jackknifes. As shown, we expect the jackknifes to show no signals whatsoever. The red line indicates theory curves. *Figure from [2].*

leaked polarization signal in order to detect the B-mode polarization signal from inflation.

Since the difference beam characteristics of each detector pair are expected to be static and unchanging as we observe the CMB, we can model the expected temperature-to-polarization leakage for a given mismatch mode observing a given patch of sky. The template of expected leakage can then be scaled against the observed data, and then subtracted from the observed data in order to remove the temperature-to-polarization leakage for that particular mode. In general, the template can be constructed for any beam mismatch mode in any parameterization we choose.

One of the main reasons we chose to parameterize our main beams in the basis described in Section 4.2.3 is to enable us to construct leakage templates that correspond to each of the main mismatch modes. The main beam mismatch modes that we describe in Chapter 4 can be directly related to first and second order derivatives of the temperature field, $\Theta(\hat{\mathbf{n}})$. The derivation of the relationship between the derivatives of the temperature field and the elliptical Gaussian difference parameters can be found in detail in [24, 4, 60]. A heuristic description can also be found in [60]. Here we present a very short summary of the expected leakage from the main beam mismatch modes.

We consider the leakage induced by the main beam mismatch modes (differential gain, differential pointing, differential beam width and differential ellipticity) in the parameterization that we present in Section 4.2.3.

The differential gain mismatch, $\delta g = g_A - g_B$ where $(g_A + g_B)/2 = 1$, is a mismatch in the overall normalization of the beam, and so the leakage induced by this mode is simply proportional to the difference in the detectors' response to the input temperature sky. The

leakage from the differential gain mismatch is then

$$d_{\delta g} = \delta g \tilde{\Theta}(\hat{\mathbf{n}}) \tag{5.3}$$

where $\tilde{\Theta}(\hat{\mathbf{n}})$ is the Gaussian beam-convolved temperature map.

The differential pointing mismatches in x and y are defined to be $\delta x = x_A - x_B$ and $\delta y = y_A - y_B$. In this mismatch mode, the otherwise identical beams respond to the temperature at different parts of the sky. If the temperature at the two different points is different, there is an induced temperature-to-polarization leakage when the signals from each detector are differenced. Therefore the predicted leakage from differential pointing is related to the temperature gradients, and therefore to first-order spatial derivatives of the temperature sky. The leakage induced by differential pointing modes is

$$d_{\delta x} = \delta x \nabla_x \tilde{\Theta}(\hat{\mathbf{n}}) \tag{5.4}$$

$$d_{\delta y} = \delta y \nabla_y \tilde{\Theta}(\hat{\mathbf{n}}) \tag{5.5}$$

where $\nabla_x = \frac{\partial}{\partial x}$ and $\nabla_y = \frac{\partial}{\partial y}$. $\nabla_x \tilde{\Theta}(\hat{\mathbf{n}})$ and $\nabla_y \tilde{\Theta}(\hat{\mathbf{n}})$ are the spatial derivatives of the beam-convolved temperature sky.

Differential beam width, $\delta\sigma = \sigma_A - \sigma_B$, is azimuthally symmetric and therefore insensitive to temperature gradients; however, it responds to the second-order derivatives of the temperature field. The leakage induced by this mode is

$$d_{\delta\sigma} = \delta\sigma(\nabla_x^2 + \nabla_y^2)\tilde{\Theta}(\hat{\mathbf{n}}) \tag{5.6}$$

where $\nabla_x^2 = \frac{\partial^2}{\partial x^2}$ and $\nabla_y^2 = \frac{\partial^2}{\partial y^2}$.

The quadrupolar mismatch modes, differential plus and cross ellipticity, are also only responsive to the second-order derivatives of the temperature field. The symmetry of the

definitions of the plus ellipticity (ellipticity along the x- or y-axis) and cross ellipticity (ellipticity along the diagonals of the axes) governs which terms of the second order derivatives contribute to the temperature-to-polarization leakage. Differential plus ellipticity, $\delta p = p_A - p_B$, induces a leakage that is related to the second-order derivatives of the temperature field along the x- and y-axes:

$$d_{\delta p} = \delta p \frac{\sigma^2}{2}(\nabla_x^2 - \nabla_y^2)\tilde{\Theta}(\hat{\mathbf{n}}) \tag{5.7}$$

Differential cross ellipticity, $\delta c = c_A - c_B$, on the other hand, induces leakage that is related to the cross terms of the second-order derivative of the temperature field.

$$d_{\delta c} = \delta c \frac{\sigma^2}{2}(2\nabla_x \nabla_y \tilde{\Theta}(\hat{\mathbf{n}})) \tag{5.8}$$

The deprojection templates that we construct in our pipeline are simply the derivatives of the temperature field itself. Specifically, the deprojection templates used are shown in Table 5.1. Once we have these deprojection templates, we can use one of two possible methods of removing the leakage from the data. We can renormalize the deprojection template with measured beam parameters (as listed in Table 5.1) to estimate the resulting temperature-to-polarization leakage and then subtract the predicted leakage. Or, we can deproject the modes, which is to say we can regress the templates against the CMB observation data to obtain the part of the observations that is contaminated by these particular modes of temperature-to-polarization leakage, which is then subtracted. We call the regression coefficient the "deprojection coefficient." Table 5.1 summarizes the relationship between the deprojection templates, the deprojection coefficients, and the measured beam parameters.

There are advantages and disadvantages to both the techniques of scaling to external measurements and the fitting to observed data. In many cases, we would prefer to regress

and fit the deprojection templates to remove the amount of leakage that is present in the observations. This method does not rely on external calibration measurements, and would be robust if the systematics were to change over time. However, deprojection will also remove real signal if there is real signal that corresponds to the mode that we are deprojecting. In these cases (particularly for the differential ellipticity case for BICEP2 and the Keck Array), since we have robust measurements of the beam parameters that are unlikely to change with time, we choose to scale the template with the measured beam parameters and subtract the predicted leakage.

Differential Mode	Differential Parameter	Definition	Deprojection Coefficient	Deprojection Template
Gain	δg	$g_A - g_B$	δg	$\tilde{\Theta}(\hat{\mathbf{n}})$
Pointing, x	δx	$x_A - x_B$	δx	$\nabla_x \tilde{\Theta}(\hat{\mathbf{n}})$
Pointing, y	δy	$y_A - y_B$	δy	$\nabla_y \tilde{\Theta}(\hat{\mathbf{n}})$
Beam width	$\delta\sigma$	$\sigma_A - \sigma_B$	$\sigma\delta\sigma$	$(\nabla_x^2 + \nabla_y^2)\tilde{\Theta}(\hat{\mathbf{n}})$
Ellipticity, +	δp	$p_A - p_B$	$\frac{\sigma^2}{2}\delta p$	$(\nabla_x^2 - \nabla_y^2)\tilde{\Theta}(\hat{\mathbf{n}})$
Ellipticity, x	δc	$c_A - c_B$	$\frac{\sigma^2}{2}\delta c$	$2\nabla_x\nabla_y\tilde{\Theta}(\hat{\mathbf{n}})$

Table 5.1: The differential beam mismatch modes, beam parameter definitions, deprojection coefficients as a function of differential beam parameters and deprojection template definitions. *Table from [24].*

The deprojection template is made in parallel during the observed data pairmap processing stage. The deprojection template is made by using the per-pair pointing to sample a template sky and its derivatives (as described in [24]) in order to generate a timestream template of the expected temperature-to-polarization leakage from the differential beam mismatches. The template map used is the Planck 143 GHz temperature map that has been smoothed with the BICEP2 beam profile. These timestream templates are generated for every detector pair and, once generated, are then coadded using the same criteria as science

data into per-pair maps. These maps are then coadded into per-pair, per-phase maps. At this stage, a regression is performed on the data against the template. This is done for every detector pair. We choose to regress and deproject the leakage templates over 10-hour long timescales in order to guard against short-timescale variations, as well as to increase the accuracy/precision of the regression. The deprojection is only performed on pair-differenced maps.

Once we have deprojected the per-pair, per-phase maps, we accumulate all the maps across all good detector pairs and all phases into T, Q, U maps. At this point, we also coadd the data into various subsets in order to perform jackknife splits. From here, we obtain power spectra.

In Figure 5.4, 5.5, and 5.6 we compare the deprojection coefficients from the CMB observations against the timestream templates to the measured beam parameters. In Figure 5.4, BICEP2 shows a high correlation between the deprojection coefficients and the measured beam parameters. The deprojection coefficients have been extracted from the per-phase fits and weighted-averaged over three years of observations for BICEP2, and one year each of observations for the Keck Array.

There is a positive offset seen in the differential plus ellipticity coefficients that comes from inherent TE correlation in the CMB. Since the differential plus ellipticity is defined to have modes that are along the x or y axis (which we have defined to be along the polarization axes of the B and A detectors respectively), differential plus ellipticity leaks the temperature signal into E-mode polarization signal. Therefore, deprojecting differential plus ellipticity removes not only the leaked temperature to E-mode polarization signal, but also some part of the existing E-mode polarization that correlates with the temperature

signal. This additional signal removal causes a positive offset in the correlation between the differential plus ellipticity deprojection coefficients and the measured differential plus ellipticity parameters. Simulations performed for sky realizations with inherent TE correlation reproduces this effect, while simulations without polarization signal as well as without inherent TE correlation do not show a positive offset in the comparison. As a result of this additional removal of inherent TE signal that occurs when we deproject differential plus ellipticity, for the science analysis, we choose to scale the template by the measured beam parameters and subtract the estimated leakage.

In Figure 5.5 and 5.6 we compare the deprojection coefficients derived from the CMB observations with measured beam parameters for Keck 2012 and Keck 2013 separately. The differential pointing coefficient shows a strong correlation with the measured differential pointing. However, the deprojection coefficients for differential beam width and differential ellipticity show a large scatter. This is due to the larger scatter in the deprojection coefficients for Keck which are derived from only one year of CMB observations. In comparison, for BICEP2, we use all three years of CMB observations to derive the deprojection coefficients. From simulating the noise in one year of Keck Array data, we are able to reproduce the scatter in deprojection coefficients.

In the final analysis, we regress the template for differential gain and differential pointing but, for differential ellipticity, we subtract a scaled template based on measured differential ellipticity. We prefer to deproject since deprojecting does not rely on external measurements of beam parameters and gain calibrations of the detectors. However, since there is inherent TE correlation in the sky, and the deprojection of differential ellipticity does remove real signal, we choose to subtract differential ellipticity instead of deproject-

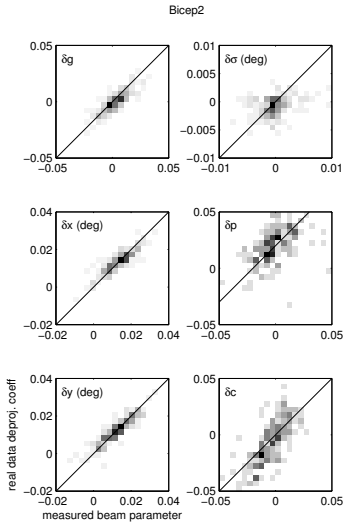

Figure 5.4: A comparison of deprojection coefficients derived from observed data with measured beam parameters for BICEP2. The measured beam parameters for differential pointing, differential beam width, and differential ellipticity are taken from far field beam map measurements, while the measured differential gain is taken from the absolute calibration scaling of the per-detector maps to the Planck CMB temperature map. The deprojection coefficients from CMB data show a strong correlation with the measured beam parameters. The differential plus ellipticity deprojection coefficients are positively biased due to inherent TE correlation in the CMB. *Figure from [24].*

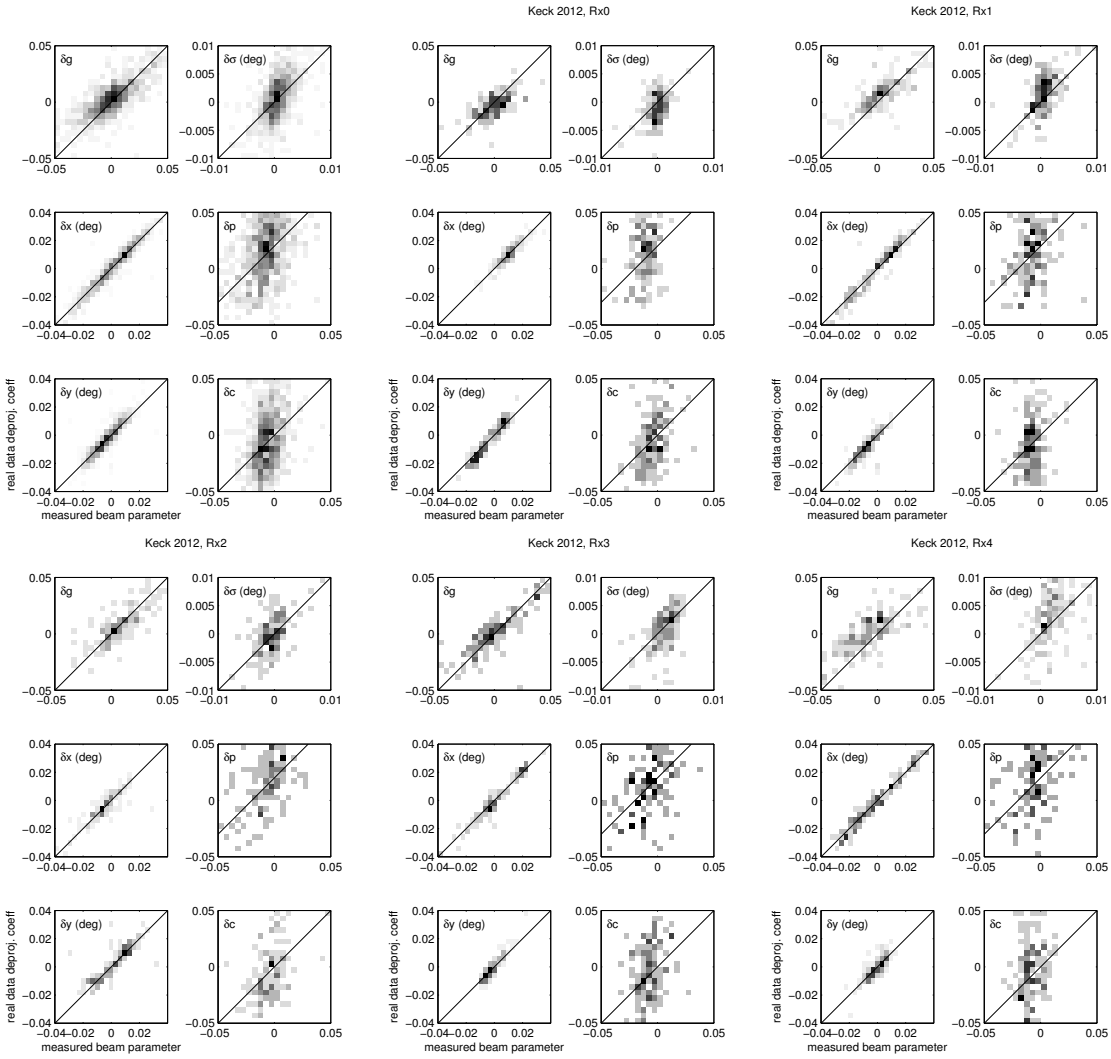

Figure 5.5: A comparison of deprojection coefficients from observed data with measured beam parameters for the Keck Array 2012 observing season. The measured beam parameters for differential pointing, differential beam width and differential ellipticity are taken from far field beam map measurements, while the measured differential gain is taken from the absolute calibration scaling of the per-detector maps to the Planck temperature map. The scatter in the deprojection coefficients seen here is due to the noise in the observed data from only using one year of observations.

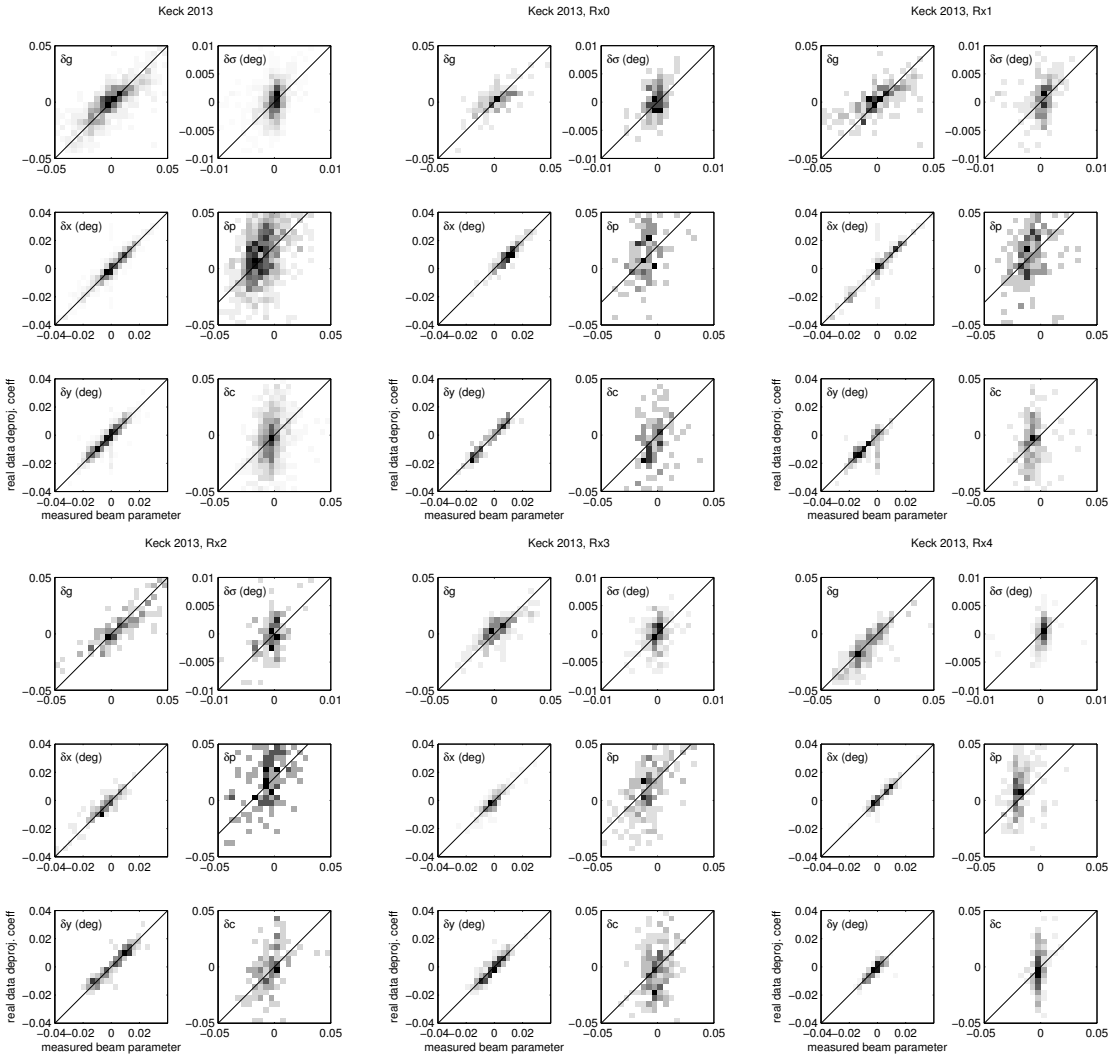

Figure 5.6: A comparison of deprojection coefficients derived from observed data with measured beam parameters for the Keck Array 2013 observing season. The measured beam parameters for differential pointing, differential beam width, and differential ellipticity are taken from far field beam map measurements, while the measured differential gain is taken from the absolute calibration scaling of the per-detector maps to the Planck temperature map. The scatter in the deprojection coefficients seen here is due to the noise in the observed data from only using one year of observations.

ing it.

5.2 Simulation pipeline

In this section, we will discuss the simulation pipeline that allows us to generate simulated timestreams that we can then feed into the analysis pipeline.

The signal-only simulation takes an input T, Q and U sky that has been smoothed with the BICEP2 beam profile, and samples the input map according to the pointing trajectory of each detector, creating simulated timestreams for each detector. The simulated timestreams are then fed into the analysis pipeline to be filtered and binned in the same way real timestreams are, to make maps, and are then reduced to power spectra.

For the general analysis, we generate a variety of input skies that are randomly generated but match the required power spectra. We also use constrained realization simulations, where the input skies used are all simulated skies with the observed T sky pattern. The matrix purification method is computationally expensive to perform, and so we take advantage of the precise knowledge of the temperature sky to generate the observation matrix. For the signal-only simulations, we run unlensed ΛCDM spectra, lensed ΛCDM, as well as B-mode only simulations at $r = 0.2$.

The noise simulations are generated by randomly flipping the sign of each scanset. The sign-flip sequences require that the total weight of the positively and negatively weighted maps are equal.

These signal and noise simulations are then combined in various combinations [2] to create simulation sets which are then used to estimate the filter-beam correction to the power spectra, the noise debias, as well as used to estimate the statistics of the observed

signal.

In addition to the general simulation pipeline, we have additional simulation techniques in order to simulate various instrumental effects [24]. Of concern to us is the method we use to simulate elliptical Gaussian beams called the "multi-Gaussian" (multigauss) simulations. A full description can be found in [24]. An elliptical Gaussian beam can be approximated by superposing multiple circular Gaussian beams with various beam widths, centers and amplitudes. The multigauss simulations use two or more input maps that have been pre-smoothed to varying circular beam widths. The simulation pipeline interpolates these maps and superposes the resulting timestreams in order to approximate the timestream that results from an elliptical Gaussian beam. Arbitrary precision can be reached by using an arbitrary number of input maps smoothed to different beam widths, but in our simulations, we use three input maps smoothed to three different beam widths which allow us to simulate timestreams that are accurate for elliptical beams with ellipticities less than 0.15. The multigauss simulations use spherical input skies and simulate the response of elliptical beams to relatively high accuracy [24], and we can use these simulations to predict the temperature-to-polarization leakage for elliptical Gaussian beam mismatch modes.

5.3 Temperature to polarization leakage using beam map simulations

In addition to the multigauss simulations, which simulate temperature-to-polarization leakage from mismatched elliptical beams, we would like to understand the temperature-to-polarization leakage from higher-order terms of our beams. To do this, we use the "beam

map simulations."

5.3.1 Beam map simulations

The beam map simulations convolve any two-dimensional convolution kernel that has an arbitrary beam with an input flat sky. The convolved maps are then sampled to produce per-detector timestreams which are then fed into the regular data processing pipeline. The convolution can be done with an arbitrary convolution kernel for any detector. This method allows us to apply all the filtering and deprojections onto the simulated timestreams that we perform on the science observations to accurately simulate what happens when we observe the sky with our beams.

We run temperature-only simulations (no polarization signal included) in order to make it easier to understand the results of the simulations. Since there is no intrinsic polarization, any polarization signal that results in the simulation must be a consequence of temperature-to-polarization leakage from beam mismatch. We run signal only simulations in order to ensure that all the polarization leakage is due to the beam shapes and the noise in the beam maps. The input sky map is the Planck 143 GHz temperature map. The timestreams are deprojected using the deprojection template used for CMB observations which does have noise in it in order to accurately reflect what we do during science observations.

A robust check on the beam map simulation is performed by comparing the results of the simulation to the results of the multigauss simulation pipeline. In the multigauss approach, we use multiple curved-sky, circular Gaussian beam-convolved input maps in order to simulate elliptical Gaussian beams. This approach has been shown to accurately simulate elliptical Gaussian beams for ellipticities $e < 0.15$[24]. The multigauss approach

uses a curved sky and, as such, is used as the standard against which we can check the results and the validity of the beam map simulations.

Since we have a benchmark to compare against, we can run the beam map simulation with exactly the same inputs as we run the multigauss simulations with. The input beam mismatch modes used here are the measured per-detector beam parameters. In order to use the exact same input beam parameters in the multigauss sim as in the beam map simulations, we make two dimensional elliptical Gaussian beam maps using these beam parameters. These simulated elliptical Gaussian beam maps can have noise added to them in order to understand how much the noise in the real composite beam maps affects the results of the simulations.

Comparing the results of the elliptical Gaussian beam map simulations with the results of the multigauss simulations tells us how well the beam map simulations are working and where they are not. As a first order check, if the constructed beam map simulations do not reflect the behavior of the multigauss simulations, then there has to be something wrong with the simulation procedure. Once we have checked that, we can explore the limitations of the beam map simulation by comparing both the maps and the spectra against the multigauss simulation.

By far, the most obvious limitation of the beam map simulation procedure is that it uses a flat-sky convolution. This creates distortions, particularly at the edges of the input map. However, since both the A and B detectors use the same flat sky, the predicted leakage is highly accurate. The deprojection of the simulation, however, is performed using the regular curved sky templates. The mismatch between the deprojection template and the input flat sky causes the leakage from the main beam mismatch modes to not be completely

deprojected away. As such, the accuracy of the beam map simulation prediction is limited as we deproject more and more modes away.

This mismatch is most clearly seen in Figure 5.7. Most of this mismatch is a product of differential pointing. The discrepancy between the flat sky convolution and the deprojection template causes the differential pointing mismatches to not be perfectly deprojected away, resulting in residual leakage that is most clearly noticed in the deck jackknife (which is the jackknife most sensitive to differential pointing). This results in a leakage deprojection floor (Figure: 5.8) beyond which we cannot know the residual leakage. This floor is at a level of $r \simeq 10^{-4}$ [24].

On the whole, we find that the flat sky convolution does not limit our understanding of the temperature-to-polarization leakage predicted by the beam map simulations. We take advantage of this simulation pipeline to run simulations using our measured beam shapes. Using the high signal-to-noise beam maps that we describe in Chapter 4, we can make composite beam maps of the beam response for each detector to relatively wide angular distances. We use these high signal-to-noise composite beam maps to directly simulate and predict the temperature to polarization leakage from mismatch in the beam shapes.

5.3.2 Composite Beam Maps

The two-dimensional kernels that are fed into the beam map simulation pipeline to predict the temperature-to-polarization leakage from the entire beam shape are constructed from a composite of the far field beam maps that we describe in Section 4.2.1.

For BICEP2, we use the 45 cm aperture "uber-chopper" source maps taken in November and December 2012. Three sets of maps were taken at different bias levels in order to find

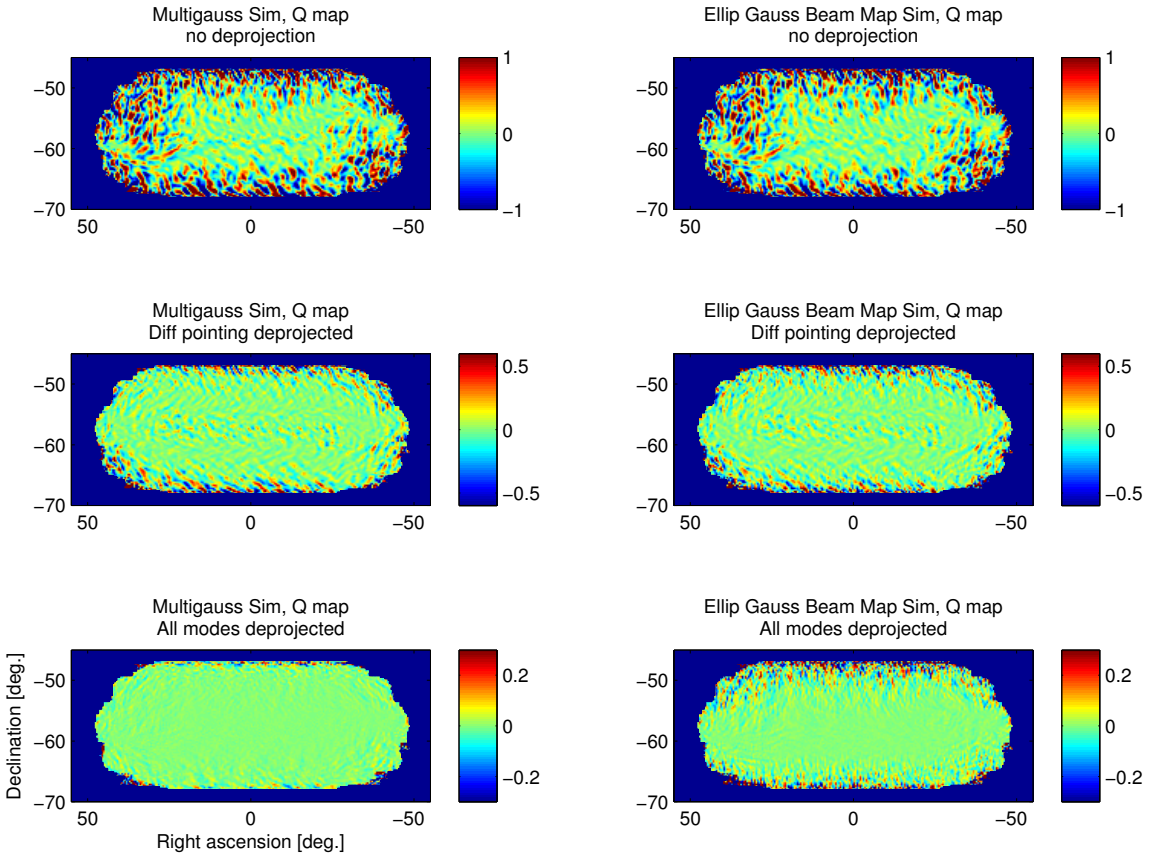

Figure 5.7: Deprojection limitation of the beam map simulation compared to the multigauss simulation. The maps display the Q polarization map after various deprojection options. The left column shows the Q polarization map from the multigauss simulation, while the right column shows the Q polarization map from the beam map simulation. The top row has not been deprojected, the center row shows the resulting contamination after deprojecting differential pointing mismatch, and the bottom row displays the temperature-to-polarization leakage after all main beam mismatch modes have been deprojected. The input sky as well as input beam mismatches are the same for both simulations. As we can see, the mismatch between the flat sky convolution that the beam map simulation uses and the curved sky deprojection template results in a floor below which we cannot predict. *Figure after Chris Sheehy*.

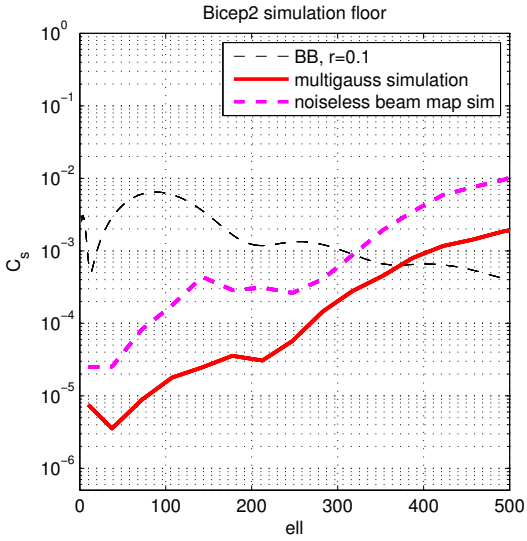

Figure 5.8: Deprojection floor for the multigauss simulation (red) and the beam map simulations (magenta). The beam map simulation deprojection floor is a result of the mismatch between the flat sky algorithm used for generating the beam map simulations and the curved sky used in deprojection. The artificial floor of the beam map simulations is larger than that which we obtain for the multigauss sim.

optimal response settings for all detectors and to reduce gain compression issues that were present in a few detectors. Each set of maps consists of maps taken at 4 different deck angles (Deck=90, Deck=0, Deck=-90, Deck=-180), resulting in a total of 12 beam maps for each detector.

Since the mast that holds the thermal source is 40 feet high, the thermal source is only approximately 2° above the horizon. We are unable to prevent seeing the ground, the mast, and the building when we are mapping out the source. While the demodulation helps reduce the signal from the ground, the remaining noise is still high. In addition, we are usually able to see the mast that holds the source in the maps. The lower half part of any map (below the beam) is noisy and does not reflect the true beam systematics. In order to mitigate this imperfect map of the beam response, we take maps at multiple deck angles, at multiple bias settings. Figure 5.9 shows an example of a composite beam map that has been built from the set of 12 component maps for BICEP2.

Using these maps, we make a composite beam map that will show the entire shape of the beam on the sky out to large angular distances from the center of the beam. We first process these maps identically, and bin them at twice the elevation step size. We mask out the ground and mast in these maps by masking the entire bottom of the map that is $\sim 1.5^\circ$ below the beam. Then, we rotate these maps to deck=0, in order to have everything in the same orientation. These maps are then centered between the beam centers of each detector in the detector pair (called the common AB beam centroid). We then take the median value for each pixel across all the component maps.

Taking a median filter allows us to downweight the spurious signals in the individual maps that are not repeatable across maps. It is a simple and effective method for making

clean, high signal-to-noise composite beam maps. As we can see in Figure 5.9, not all parts of the composite beam map have the same number of input component beam maps. This is primarily the consequence of masking the ground contaminated part of the component map However, for a radius of less than 1.2° from the beam center all 12 component maps contribute to the composite map. All pixels in the map also include maps from at least three separate maps.

The Keck Array composite beam maps for 2012 and 2013 are built from set of maps taken in February 2012 and February 2013 respectively. The maps taken in February 2012 use the 20 cm diameter "ze-choppa" thermal source, and as a result have lower signal levels compared to the Bicep2 component maps or the Keck February 2013 maps, which use the 45 cm diameter "uber-chopper" thermal source. The Keck beam maps are taken from a set of ~ 25 beam maps taken at 10 different deck angles. For each receiver, however, we can only use beam maps taken at a maximum of 5 deck angles. For the other 5 deck angles, the receiver is not below the mirror, and therefore is not mapped. For each of the 5 deck angles for which the receiver is under the mirror, there is a cut implemented that removes all the maps for pixels that do not reflect off the mirror. As a result of this, each Keck detector's composite map has maps with only 2 to 4 deck angles included. Figure 5.10 shows the distribution of deck angles included for each detector's location in the focal plane.

The minimum number of maps included in any detector's composite map is one. This is primarily due to Receiver 0 in the Keck 2013 season. Due to various problems during the beam mapping runs, only 4 maps were taken and, with various cuts implemented, there are detectors that only have one component map. In general, the minimum number of maps included in the composites is 4. The median number of maps included is 9, while the

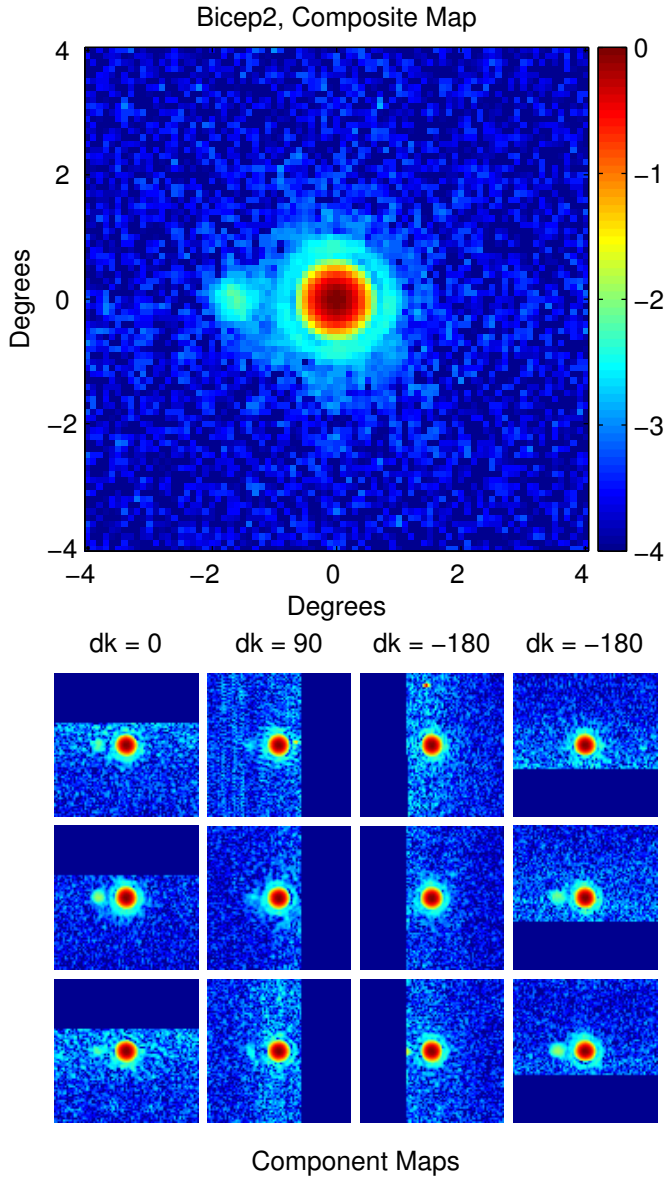

Figure 5.9: Example composite beam map for a single detector in BICEP2. The composite beam maps for BICEP2 are made from 12 component maps taken at four deck angles. The component maps have been masked to remove contamination from the ground, and then rotated to deck 0, and then composited with a median filter. An Airy ring and an inductive cross talk beam can clearly be seen. *Figure from [25].*

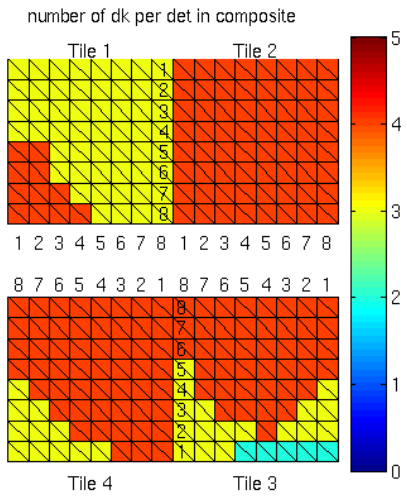

Figure 5.10: Number of deck angles that are included in the composite map for each detector in each receiver of the Keck Array. The number of deck angles that goes into each map varies between 2 and 4 deck angles, with the majority of detectors having component maps taken at 4 deck angles.

maximum number of maps included is 11.

Figure 5.11 shows an example of the resulting composite beam map for a single detector for Keck. Because the source that Keck maps is on the DSL mast, Keck also sees the South Pole Telescope (SPT) in the maps. In addition to masking the ground, for the Keck composite maps, we have also masked out SPT. As we can see, as a result of the deck angle coverage limitations, for each detector there is a rather large patch of map that is not mapped. Figure 5.12 shows the fraction of missing data for each detector in each receiver. In order to as accurately as possible reflect the real beam map, we fill in the empty parts of the composite beam map with an estimate of signal and noise. To a first order approximation, the beam maps are azimuthally symmetric, so the empty parts of the beam map are filled with values that are dithered on the azimuthally averaged mean. Despite the lack of coverage at large angular distances away from the center of the beam, for a radius

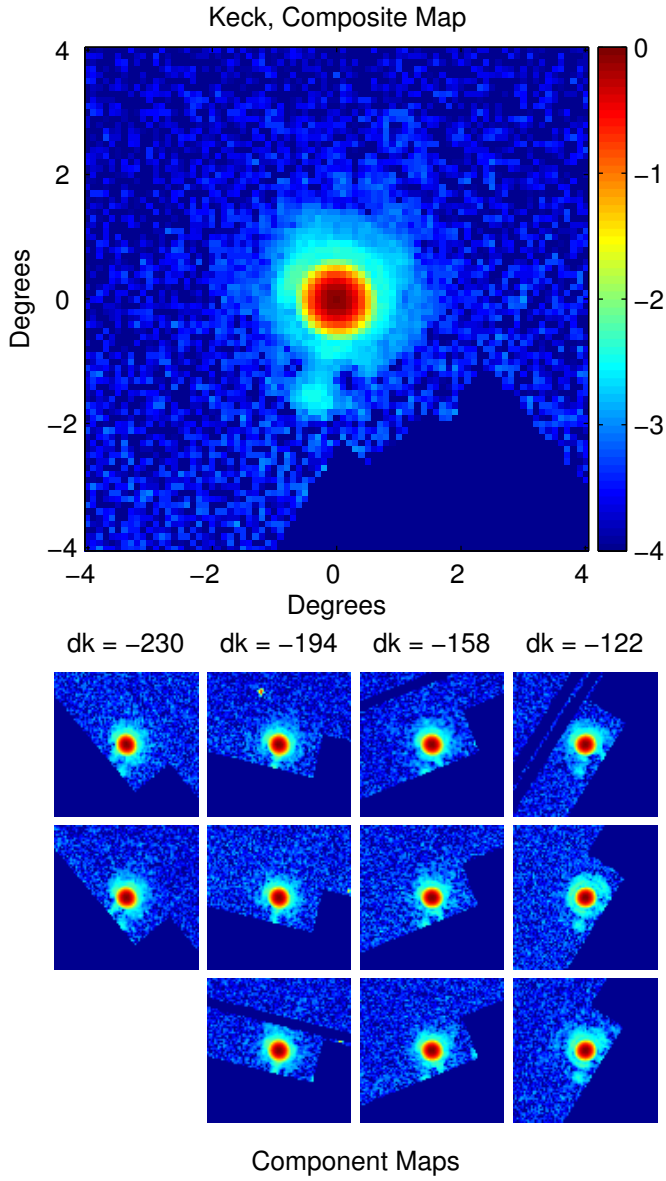

Figure 5.11: Component and composite beam maps for a single detector in the Keck Array made with the 45cm aperture source. The maps are masked to remove contamination from the ground and from the South Pole Telescope. Due to the increased masking as well as the lack of maps taken at enough deck angles, the composite beam maps for Keck do not fully cover the $8^\circ \times 8^\circ$ field. The empty parts have been filled with the mean of the radial annulus and noise. *Figure from [25].*

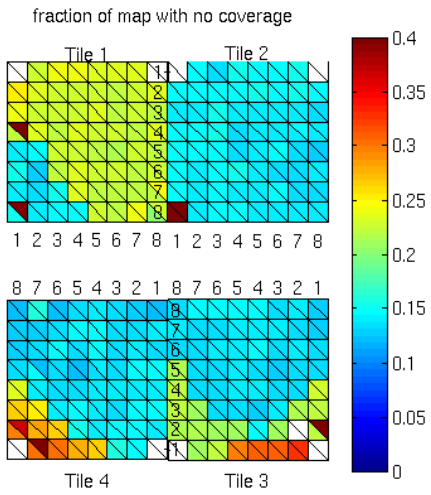

Figure 5.12: Fraction of composite beam map for each detector in Keck that has no data due to the masking of the ground as well as SPT. On average, each composite map is missing 15% of data, as can be seen in Figure 5.11.

of $r < 1.2^\circ$ away from the center of the beam, the composite beam maps do have beam map data and therefore are generally built from multiple beam maps.

In making the maps for Keck, we have also implemented a semi-automated quality cut, which removes maps that do not show a beam, or have too much noise. The cut judges the quality of the map based on the amplitude of the fitted Gaussian beam as well as the position of the Gaussian beam. A cut is also implemented by hand, once we have made the composites and run a first round simulation to cut out component maps that are too noisy or have too many artifacts. While this reduces the number of component maps, this also reduces the possibility of simulating leakage that is not real. In addition, there is also a set of detectors that were not working for various reasons during the beam mapping runs. We do have evidence from science observations that these detectors work during the CMB runs, and so we kept them in our analysis. However, this means that there are some channels that

are not cut from the science analysis that do not have any beam maps. There are 9 such channels in the Keck 2012 composite beam maps, and 28 such channels in the Keck 2013 composite beam maps. Finally, we exclude detectors that have maps that are too noisy and contribute false signals in the simulation. This is an additional 4 pairs in 2012, and 4 in 2013. In total, we disregard 2% of good channels in 2012 and 4% in 2013.

Since the BICEP2 and Keck Array 2013 composite beam maps were made with multiple uber-chopper beam maps, they are high signal to noise. In order to evaluate the contamination that is caused by the noise in the beam maps, we run beam map simulations with constructed beam maps with added white noise in comparison to the simulations run with noiseless beam maps.

We estimate the level of noise in the beam maps by finding the standard deviation of the values of the pixels for the area of the map that is beyond a radius of 2° from the center of the map. This removes the bulk of the beam response and allows us to accurately measure the noise in the beam maps. Gaussian random numbers are generated using the standard deviation of the measured noise values and inserted into noiseless elliptical Gaussian maps.

We find that for maps with levels of noise below the noise level of the uber-chopper beam maps the noise in the beam maps do not contribute significantly to the predicted temperature to polarization leakage. Figure 5.13 shows the level of temperature-to-polarization leakage that we expect from the noise levels in the uber-chopper beam maps. The noise levels in the composites are expected to be smaller, since we use multiple component maps to make the composites. The flat sky convolution limitations trumps the limitations from the noise in the beam maps. The algorithmic floor is discussed in Section 5.5 and shown in Figure 5.24.

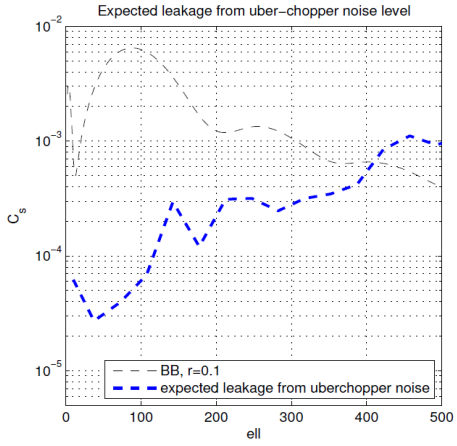

Figure 5.13: The temperature-to-polarization leakage predicted from the noise levels in the uber-chopper beam maps. This prediction is obtained by taking the difference of the leakage predicted by the noiseless beam maps and the leakage predicted by artificially constructed beam maps with uber-chopper noise levels inserted. The composite beam maps are expected to have even lower noise levels from the averaging down of multiple component beam maps.

5.4 Understanding the beam map simulations

Our entire analysis and simulation pipeline results in power spectra for the fourteen jackknife maps and for the fully coadded map. Similarly for the beam map simulations, we obtain six spectra (TT, TE, EE, BB, TB, and EB) for all fourteen jackknife maps, and for the single non-jackknifed (jack0) map. We evaluate these spectra in order to understand the performance and results of the beam map simulations.

We are primarily interested in the channel-split jackknives, as well as the jack0 spectra. The channel-split jackknives let us probe the differences between the performance of different subsets of detectors, allowing us to understand the effect of specific beam mismatches. The jack0 spectra will ultimately tell us what the level of temperature-to-polarization leakage is predicted to be based on the actual beam shape mismatches that are present in the

beam maps. Here we scrutinize the TE, TB, and BB spectra. The EB spectra is not very informative since we do not use polarization in the beam map simulations.

A very powerful test of the validity of the beam map simulations is the comparison of the beam map simulations against our observed data. We try to make the simulations reflect what is happening in our CMB observations as much as possible, by using our high signal-to-noise real beam shapes and the Planck input sky, as well as processing the simulation using the same pipeline as processing the observed data. As much as the beam maps reflect the real shape of the beams, we should see the leakage predicted by the simulations in the observed data.

To do this, we visually compare the spectra from the beam map simulations, and the observed data points. We start with looking at the jackknife spectra, particularly the channel-split jackknives. The jackknifes should not contain any signal, and so any failure in the jackknife spectra are due to telescope systematics. Failures in the channel split jackknifes that are attributed to beam mismatch should be reproduced and predicted in the beam map simulations. This is a check, both that the beam map simulations are accurately predicting behavior in the real CMB observations, and also that the main beam mismatches are accurately represented in the beam maps.

Once we understand the jackknife spectra of the beam map simulations, we can then turn our attention to the non-jackknifed spectra from the beam map simulations and from the CMB observations. The non-jackknifed spectra for the beam map simulations predicts the level of temperature-to-polarization leakage from the beam shape mismatches. We would like to quantify the level of temperature-to-polarization signal that is predicted to be in the science observations before and after deprojection, and remove the leakage from the

science data.

5.4.1 Differential pointing mismatch

The differential pointing beam mismatch in BICEP2 and the Keck Array is by far the most dominant beam mismatch mode in our detectors and, as such, is easy to quantify and to predict the leakage of. The regular simulation pipeline which simulates timestreams from each detector's pointing can simulate the leakage from the pointing mismatch accurately. The predicted leakage from the beam map simulations which encapsulate the pointing mismatch in the beam maps themselves should also predict the leakage from the pointing mismatch accurately.

Figure 5.14 shows that the beam map simulations do capture the differential pointing mismatch very well. In this figure, we show the TT, TB, and BB spectra for the non-jackknifed map for BICEP2. The black points are points from BICEP2's data, and the error bars have been derived from the signal+noise simulations. The dashed black line indicates spectra derived from ΛCDM-cosmology as well as tensor B-mode spectra at $r = 0.1$. The green lines indicate the spectra we obtain from the beam map simulations. Visually, we can see that the green lines agree with the data points relatively well. We can take a cross spectrum between the real B map as well as the beam map simulated B map, to find the level of signal that is common in both maps. This is the red line in the BB spectra plot. As we can see, the temperature-to-polarization leakage from differential pointing shows up both in observed data as well as in the beam map simulations.

The deck jackknife also fails without any deprojection of the differential pointing mismatch. Figure 5.15 shows the failure in the BB spectra in the deck jackknife for BICEP2. As

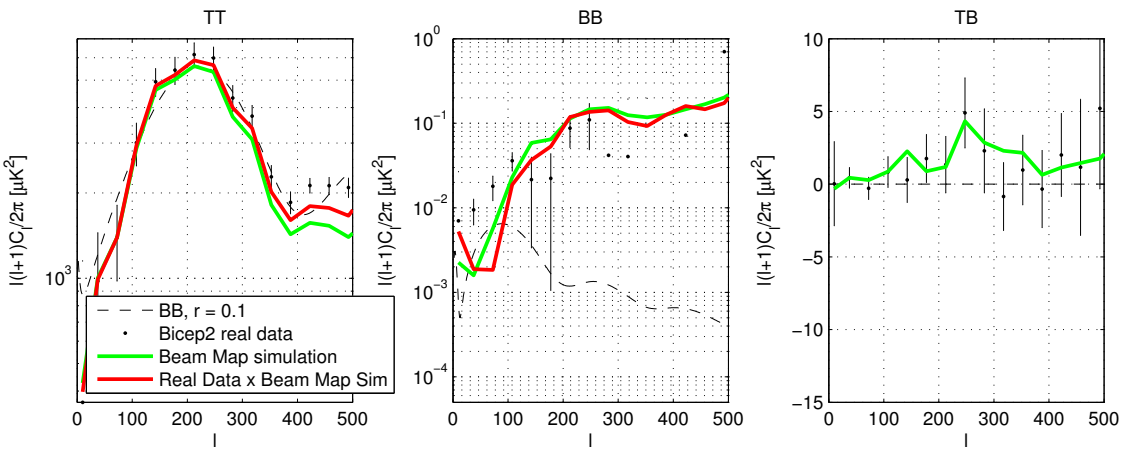

Figure 5.14: The beam map simulations reproduces the temperature to polarization leakage seen in the CMB data. The black points are BICEP2's observed CMB data without any deprojections. The green lines, which are the spectra generated from the beam map simulations, follow the observed CMB data points quite well. The red lines are the cross spectra of the observed CMB data with the beam map simulations and picks out features that are common between the CMB data and the beam map simulations, and agree with the beam map simulation results.

the figure illustrates, when differential pointing is deprojected, the leakage that is induced is significantly lowered.

Deprojecting differential pointing removes much of the induced temperature-to-polarization leakage for many of the jackknifes. This is encouraging and seems to reflect the behavior of the observed CMB data. The resulting beam mismatches (differential beam width and differential ellipticity) are much smaller than the differential pointing mismatch.

5.4.2 Differential ellipticity mismatch

Once we have deprojected the differential pointing mismatch, we can look at other beam mismatch modes which are smaller than the differential pointing mismatch modes. In this section, we consider the differential ellipticity mismatch mode.

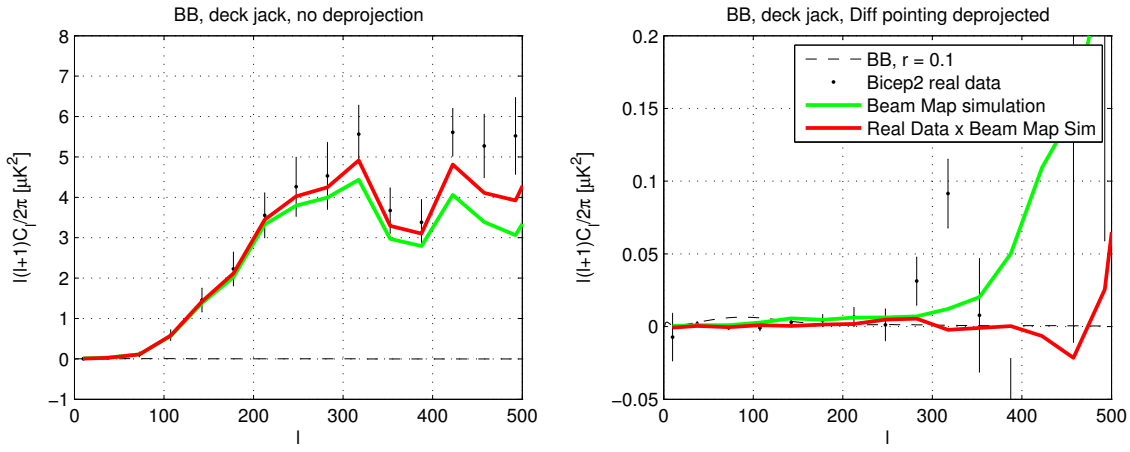

Figure 5.15: Left: The deck jackknife failure in the CMB observations due to differential pointing is reproduced in the beam map simulations. Right: Once the differential pointing mismatch is deprojected, the beam map simulation still predicts the observed CMB data spectrum.

Figure 5.16 shows how differential ellipticity mismatches affect the focal plane inner/outer jackknife for BICEP2. As we see in Chapter 4, the ellipticity of the detectors is worse towards the edges of the focal plane. Also, the differential ellipticity is worse on the edges of the focal plane, so we do expect the focal plane inner/outer jackknife to show jackknife failures. This is well predicted in the multigauss simulations as well as in the beam map simulations. In Figure 5.16, we find that the predicted simulation leakage is well matched by the observed data points. Deprojecting the differential ellipticity removes this leakage, and this is again well reflected in the beam map simulation as well as the multigauss simulation.

For Keck, however, once we have deprojected the leakage due to differential pointing mismatch, the leakage due to differential beam width or differential ellipticity does not obviously show up in the jackknives. Figure 5.17 shows the focal plane inner/outer jackknife spectra for Keck. The Keck Array receivers are all located 72° from each other allowing

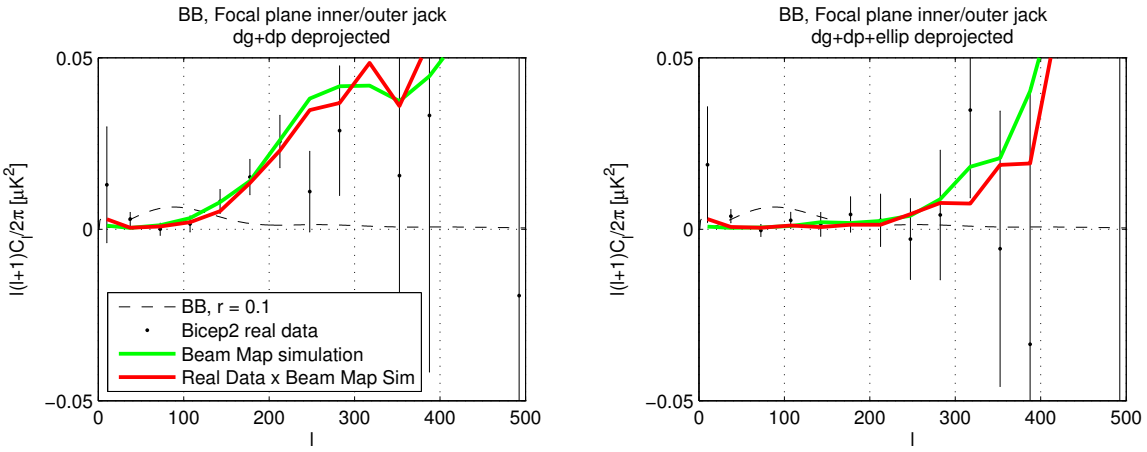

Figure 5.16: Left: Focal plane inner/outer jackknife after differential gain and differential pointing are deprojected. Differential ellipticity has not been removed. Right: Focal plane inner/outer jack after deprojecting differential gain, differential pointing, and differential ellipticity. Black points indicate observed data, green lines show the spectra predicted by the beam map simulations, and the red lines are the cross spectra between the observed data and the simulation. The beam map simulations accurately predicts the jackknife spectra of observed data before and after deprojecting differential ellipticity.

for more cancellation of systematics, and so once we have deprojected differential pointing, there are few other jackknife failures. However, the beam map simulations do predict a failure in the TB spectra if we do not deproject differential ellipticity and this is confirmed by the science data as seen in Figure 5.18.

5.4.3 Simulating Relative Gain Mismatch

As we have described in Section 4.2.3, we do not use the beam maps to measure the gain of the detectors. Since the composite beam maps use the aluminum transition and take data pointed closely at the horizon, we do not take calibration elnods during beam mapping data taking schedules. As a result, the amplitude of the beam response in each detector is somewhat arbitrary.

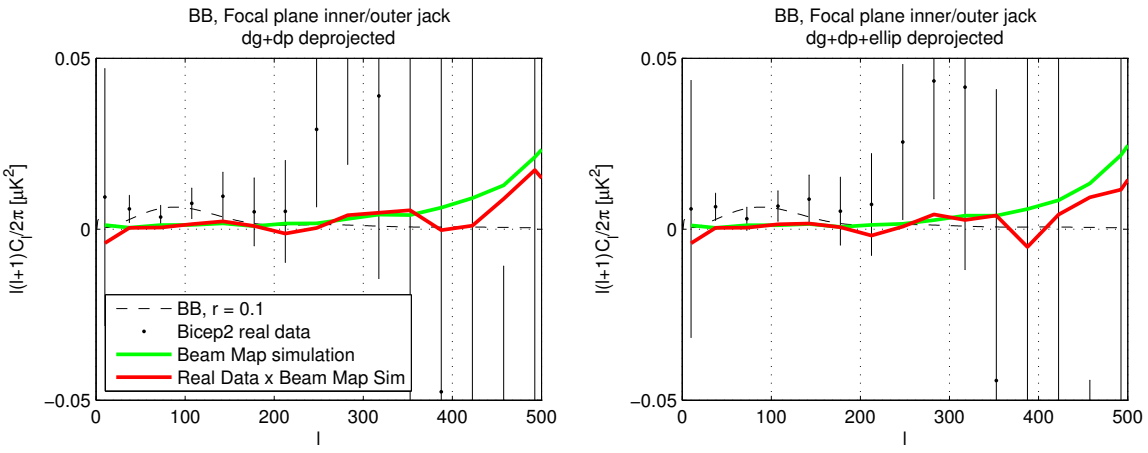

Figure 5.17: Left: Focal plane inner/outer jackknife for Keck 2012 after deprojecting differential gain and differential pointing. Right: Focal plane inner/outer jackknife for Keck 2012 after deprojecting differential gain, differential pointing, and differential ellipticity. Black points indicate observed data, green lines are the beam map simulation spectra, and the red lines show the cross spectra between observed data and simulation. The five Keck receivers are oriented at 72° from each other resulting in more averaging down of beam systematics resulting in fewer jackknife failures once we have deprojected differential gain and differential pointing.

In order to simulate relative gain mismatch in the beam map simulations, we have to renormalize the input beam maps to correctly reflect the relative gains of each detector in a pair. We would like to ensure that we are renormalizing the beam maps in a similar manner to the method by which we obtain the absolute gain calibration of the detector. The absolute calibration of the detector gains is calculated by comparing the normalization of the per-detector CMB temperature maps to the Planck 143 GHz temperature map at $100 < \ell < 300$. Similarly, we renormalize our beam maps such that the beam window function, B_ℓ, derived from each detector's beam map, matches the relative calibration in the same ℓ range of $100 < \ell < 300$.

We find that differential gain mismatch deprojection is an effective process. We have simulated up to three times the measured relative gain mismatch and have found that de-

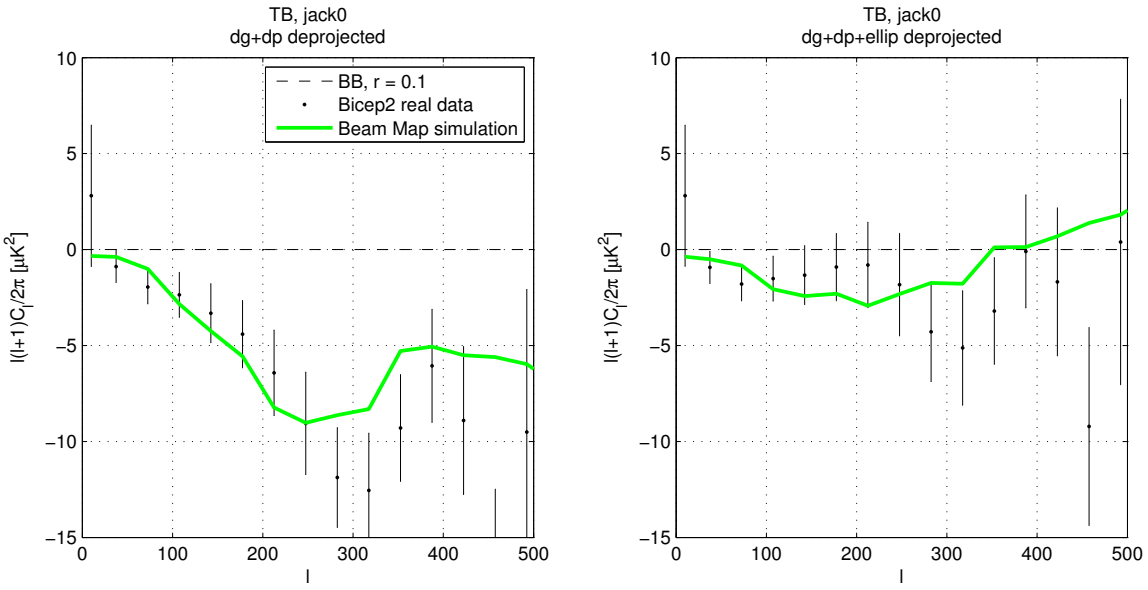

Figure 5.18: Left: Keck 2012 TB spectra after deprojecting differential gain and differential pointing. Right: Keck 2012 TB spectra after deprojecting differential gain, differential pointing, and differential ellipticity. Black points are observed data for Keck 2012's observing season and green lines are the TB spectra from the beam map simulation. The differential ellipticity deprojection on Keck data only shows a strong effect on the TB spectra. Without differential ellipticity projection, the TB spectrum shows a strong non-zero spectra, while with differential ellipticity deprojection, the TB spectrum is closer to 0.

projecting the relative gain always results in a complete removal of the induced differential gain mismatch. A detailed discussion on the differential gain mismatch can be found in [24].

5.4.4 Deprojection coefficient comparison

A final method for understanding the validity of the beam map simulations is to compare the deprojection coefficients from the simulations to the deprojection coefficients from observed data. If we are simulating the correct main beam mismatch modes in the beam map simulations that appears in observed data, the deprojection coefficients from the beam map simulations should match the deprojection coefficients we obtain from observed data.

Figure 5.19, 5.20, 5.21 show a comparison of the deprojection coefficients from observed data with deprojection coefficients from the beam map simulations for BICEP2, and the Keck Array for 2012 and 2013. Figure 5.19 shows a strong correlation in all main beam mismatch modes for BICEP2. There is a positive offset in the observed data deprojection coefficients as there is inherent TE correlation in the CMB as described in Section 5.1.6. The beam map simulation does not include polarization and therefore does not show a positive offset in the deprojection coefficients. In Figure 5.20 and 5.21, the scatter in the Keck Array observed data deprojection coefficients is due to the larger noise from one year of observations (also described in Section 5.1.6) instead of three years of observations for BICEP2.

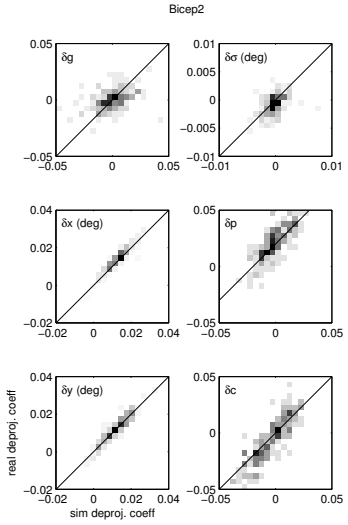

Figure 5.19: A comparison of deprojection coefficients from observed CMB data with deprojection coefficients from the beam map simulations for BICEP2. The correspondence between the deprojection coefficients look very similar to Figure 5.4 and very close to one-to-one, and so it appears that the beam map simulations are simulating the same main beam mismatch modes as they appear in observed data. The positive bias in the differential plus ellipticity deprojection coefficients is due to the fact that the real CMB sky has inherent TE correlations, while the beam map simulations do not. *Figure from [25].*

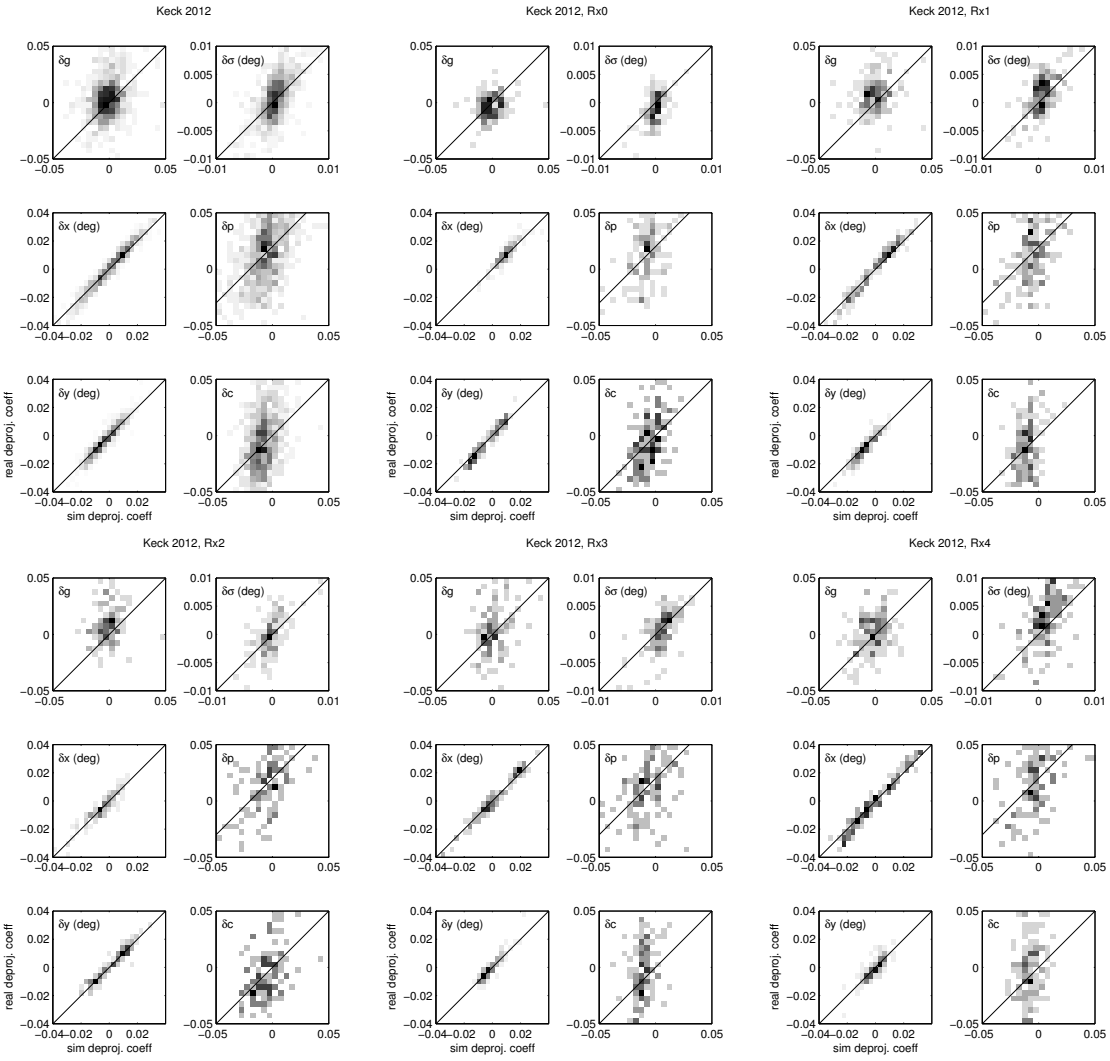

Figure 5.20: A comparison of deprojection coefficients from science observations to deprojection coefficients from the beam map simulations for the Keck Array 2012 observing season. The scatter in the deprojection coefficients from science observations seen here is due to the noise in the CMB data from one year of observations compared to three for BICEP2. *Figure from [25].*

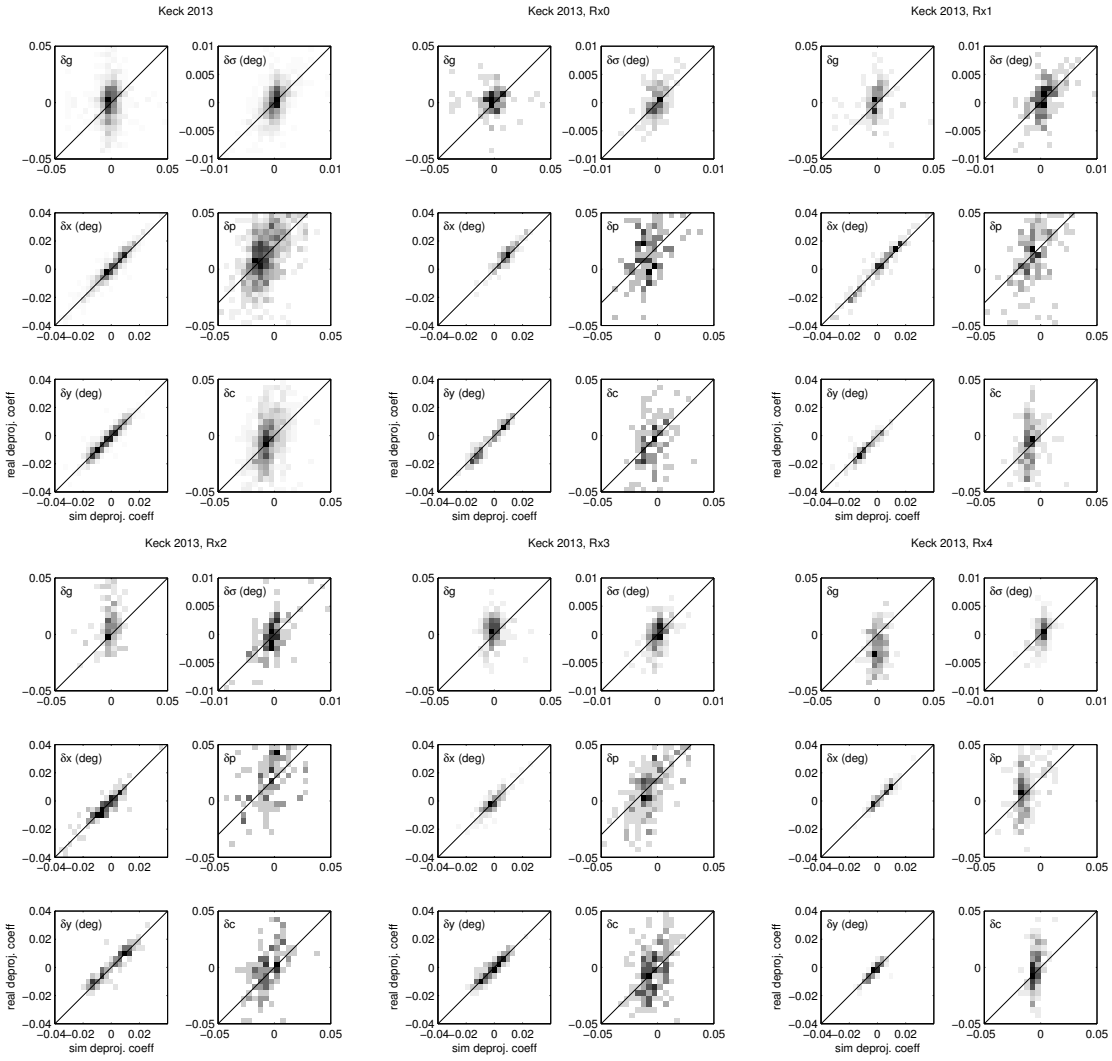

Figure 5.21: A comparison of deprojection coefficients from science observations to deprojection coefficients from the beam map simulations for the Keck Array 2013 observing season. The scatter in the deprojection coefficients from science observations seen here is due to the noise in the CMB data from one year of observations compared to three for BICEP2. *Figure from [25].*

5.5 Residual temperature-to-polarization leakage

In running and studying the results of the beam map simulations, we have ample evidence that the beam map simulations accurately predict the leakage induced by the main beam mismatch modes, such as differential pointing and differential ellipticity. It is more difficult to ascertain what the residual polarization leakage is after we have deprojected the main beam mismatch modes.

After we have deprojected the main beam mismatch modes, the CMB data pass the jackknife tests. It is clear that the level of residual temperature-to-polarization leakage that is left is low enough to not cause jackknife failures. While this is great for the science observations, since it proves that our systematics levels are low, it makes it difficult to really know if the residual temperature-to-polarization leakage that we predict is actually present in the data.

An effective method of picking out common mode signals in two maps is to take the cross spectrum between the maps. In an effort to understand if the predicted residual temperature to polarization leakage is real, we can take a cross spectrum between the B-mode map made using observed CMB data and the B-mode map made using the beam map simulation. In an ideal situation, if the predicted temperature-to-polarization leakage is present in the observations, the cross spectrum would be able to pick out the correct level of residual leakage. However, the noise in the real maps, as well as the noise in the beam maps interact, causing the cross spectrum between the science observations and the simulation to be noisy. Figure 5.22 displays the cross spectra of the observed science data and the temperature-to-polarization leakage predicted by the beam map simulations. The cross spectrum is noisy, particularly at $70 < \ell < 300$, but do show some indication of real

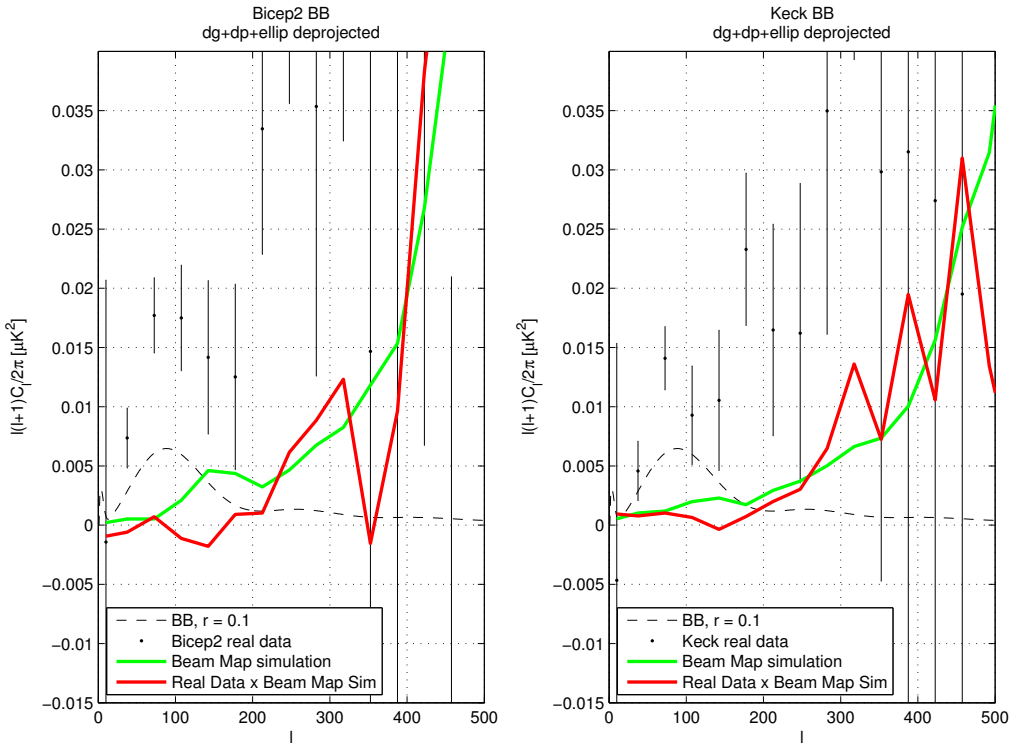

Figure 5.22: The cross spectra between the beam map temperature-to-polarization leakage predicted by the beam map simulations (green), real CMB data (black points), and the cross spectra taken between observed science data and the simulation (red) for BICEP2 on the left, and the Keck Array on the right. The cross spectra between the simulation and observed data are noisy, particularly at $70 < \ell < 300$, making it hard to tell if there is real residual. While the cross spectra at $\ell > 300$ are also noisy, the cross spectra do indicate that real residual leakage which is predicted by the beam map simulations.

residual at $\ell > 300$.

We used composite beam maps that were $8^\circ \times 8^\circ$ in width to try to capture as much of the beam as possible. While the bulk ($\sim 97\%$) of the power in the beam resides within a radius of $\sim 1^\circ$, we would like to capture as much angular structure of the beam as possible, driving us to choose to extend the composite beam map as widely as possible. However, the masking and compositing procedure outlined in Section 5.3.2 results in an uneven number of maps going into each part of the map. The outer region of the composite map has less

data entering the composite. This can be seen in Figure 5.9 and Figure 5.11. Since the outer regions have fewer component maps the noise in these regions is greater and is more susceptible to spurious fluctuations. The full composite beam maps also include cross talk beams, particularly clearly for BICEP2. In addition, for Keck, not all outer edges of the map include data from beam maps. Recall that the lack of deck angle coverage and the increased masking of the Keck Array beam maps cause patches of the map to be empty. In these empty patches we have added an estimate of the mean of the annulus as well as noise.

There are worries that the noise level in the outer parts of the beam maps would dominate the predicted temperature-to-polarization leakage, particularly as we deproject the main beam mismatch modes. It is also a concern that adding information to the outer parts of the composite beam maps for Keck Array induces false levels of temperature-to-polarization leakage. Finally, while the cross talk beams are clearly visible, it is unclear that they behave the same way during the science data taking, since the CMB data taking uses the titanium transition and not the aluminum transition. In response to these concerns, and in an effort to reduce the level of noise and spurious effects, we consider what the predicted leakage would be if we only use the inner 1.2° radius of the composite beam maps. The inner 1.2° radius of the composite beam maps include the maximum number of available component maps in as many deck angles as possible for both BICEP2 and Keck. We refer to the simulations performed using the inner 1.2° radius maps as main beam simulations, and to the simulations that use the full $8^\circ \times 8^\circ$ composite beam maps as extended beam simulations.

For BICEP2, the inner 1.2° radius beam maps have the advantage of having 12 maps going into every spot in the composite beam maps. Since the beam maps are strongly signal-

dominated in this radius, we are able to take the mean value of all the component maps here in order to make the composite beam map, allowing us to better estimate the uncertainty on the residual leakage. Figure 5.23 shows the predicted temperature-to-polarization leakage from the extended beam map simulations, the main beam maps, and the cross spectra from both sets of simulations with science observations for BICEP2. Again, the cross spectra are noisy, but it does look like the main beam simulations predict real leakage that is consistent to within the noise. For BICEP2, it is clear that the extended beam map simulations have some structure or a high degree of noise outside the 1.2° radius that induces a larger temperature-to-polarization leakage. It is unclear if this larger prediction is real. It does appear, however, that the temperature-to-polarization leakage from the main beam simulations are consistent with the cross spectra.

For BICEP2 we use a bootstrap method for estimating the noise bias and uncertainty on the predicted leakage. A detailed discussion can be found in [24]. Using the set of 12 component maps, we can create 12 versions of composite beam maps by leaving out one component map from the composites. These composites are then inserted into the beam map simulation pipeline to generate 12 predictions of temperature-to-polarization leakage. The uncertainty is estimated using the rms of each band power. The noise bias is estimated by taking the difference between the mean of the 12 additional simulation results and the main simulation we perform. This estimate of uncertainty as well as noise bias is performed for the main beam simulations as well as for the extended beam simulations. Subtracting the noise bias from the simulations, we find that the extended beam simulations predict a leakage consistent with zero, while the main beam simulation's predicted leakage has a small correction. We choose to use the uncertainty derived from the extended beam

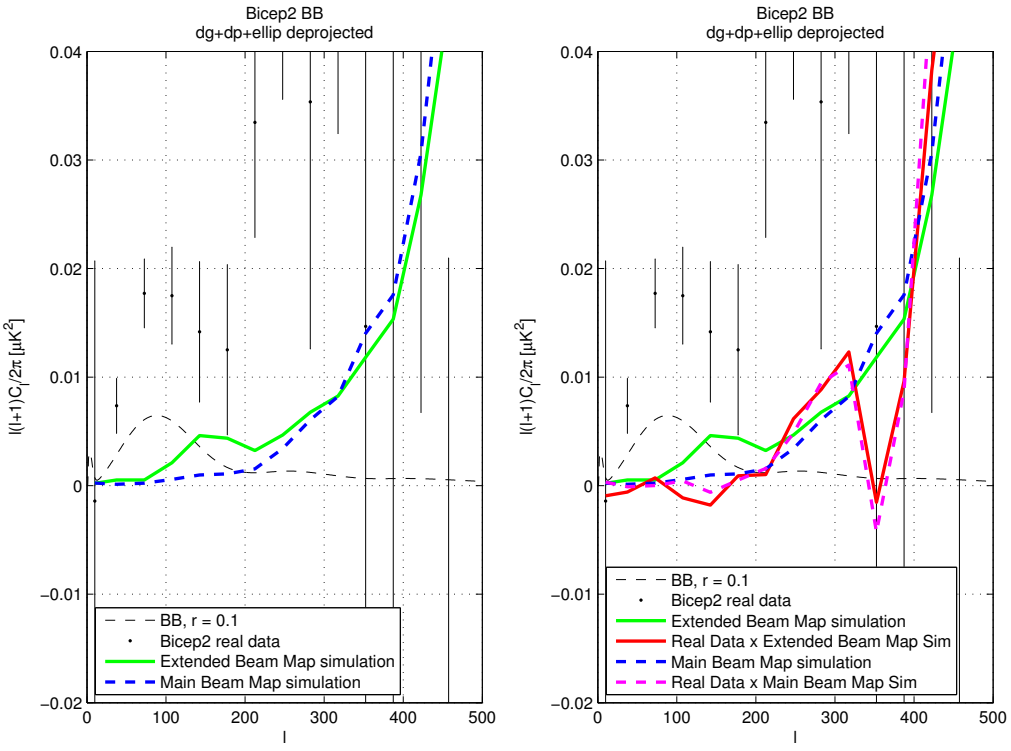

Figure 5.23: Left: Predicted temperature-to-polarization leakage from using the extended beam map simulations(green), as well as the main beam map simulations (dashed blue). Right: Cross spectra between both sets of simulations and observed science data. The cross spectra are noisy, but it does look like the main beam simulations predict real leakage that is consistent within the noise.

simulations, as we expect the extended beam simulations to capture more of the beam, although it is highly affected by the noise. We take the uncertainty as the upper limit on the predicted temperature-to-polarization leakage from residual beam mismatches and find that this upper limit corresponds to $r < 3 \times 10^{-3}$.

Finally, we consider the algorithmic floor of the simulations. There is an algorithmic floor from the beam map simulations that we obtain from simulating idealized elliptical Gaussian beam maps and deprojecting all mismatch modes. Since these are idealized elliptical Gaussian beams, the resulting leakage after deprojecting all mismatch modes is the result of the flat sky limitation of the simulation. We remove this deprojection floor from the final predicted temperature-to-polarization leakage. Figure 5.24 shows the algorithmic floor, as well as noise bias for BICEP2.

We expect that the algorithmic floor for the Keck Array 2012+2013 data to be at approximately the same level as the algorithmic floor obtained for BICEP2. After all, the beam map simulation algorithm is the same one used for both sets of data, and the floor is derived from signal-only simulations using noiseless beam maps. We expect that the noise floor and the uncertainty for the Keck Array data to also be similar to the noise floor and uncertainty derived for BICEP2 data. The noise bias and uncertainty does not come from the noise in the composite beam maps, but rather from the consistency of the beam shape from measurement to measurement. We do not expect that the consistency of the beam measurements for Keck to differ much from BICEP2, and so we expect that the noise bias and uncertainty for Keck will be similar to BICEP2.

Figure 5.25 shows the predicted temperature-to-polarization leakage for various deprojection options for BICEP2. The spectra shown here predict the level of BB contamination

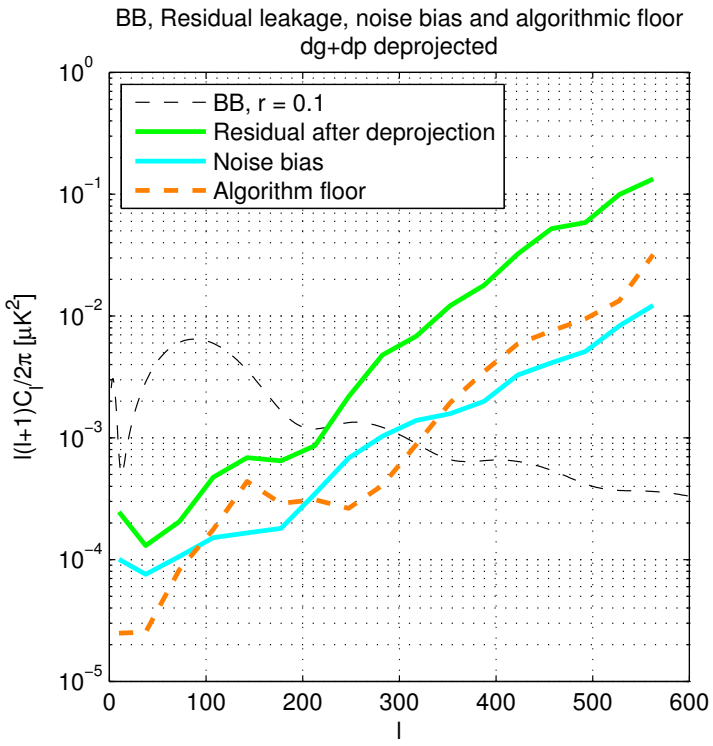

Figure 5.24: The leakage predicted by the main beam map simulations, the algorithmic floor of the beam map simulations, and the noise bias calculated for the main beam simulations. The algorithmic floor and the noise bias are subtracted from the predicted residual temperature-to-polarization leakage before the leakage is removed from observed science data.

from the beams without any deprojection options, after deprojecting differential pointing (dp), after deprojecting differential pointing and differential relgain (dp+dg), after deprojecting differential pointing, differential relgian, and differential beam width (dp+dg+bw), and finally, after deprojecting differential pointing, differential relgain, and subtracting differential ellipticity (dp+dg+ellip). As we see here, differential beam width for BICEP2 is small, and does not cause large leakage. The residual beam mismatch is at the level of $r = 0.001 \pm 0.003$ and is subtracted from the observed CMB BB auto spectra.

Figure 5.26 shows the predicted leakage from the beam mismatch modes for Keck. Recall that in Section 5.4.2, there is a substantial non-zero TB spectrum that is predicted after we have deprojected the main mismatch modes. The main beam map simulations for Keck also predict this non-zero TB spectrum, giving us more confidence that this effect does come from the residual beam mismatches.

5.5.1 Undeprojected Beam Map Residual

The beam map simulations are a robust and informative way of predicting the temperature-to-polarization leakage from the beam mismatch modes. We can understand the level of the predicted leakage from the main beam mismatch modes as well as the residual after deprojection, in a method that mirrors what happens during science observations. However, we are able to deproject the same modes in the beam maps themselves to see what the residual beam mismatch modes are.

Using the deprojection template definition in Table 5.1, we can generate the equivalent templates as derivatives of a circular Gaussian. Figure 5.27 displays the deprojection template that we will use on the beam maps.

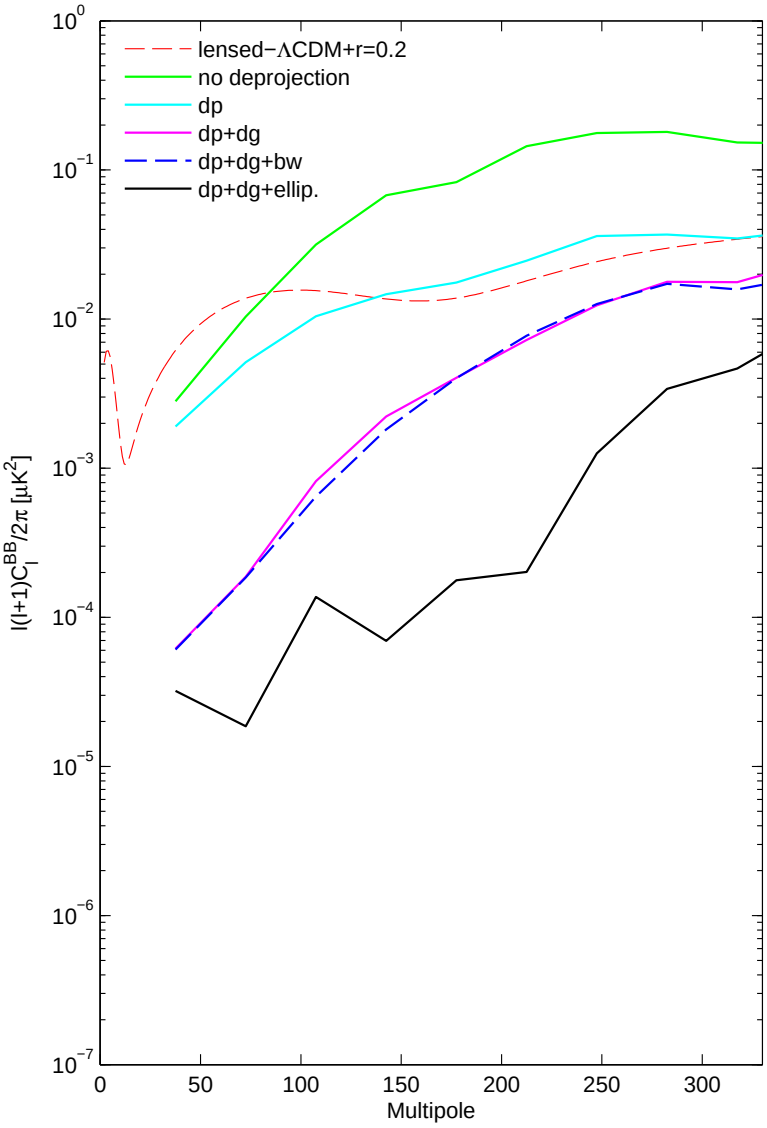

Figure 5.25: Temperature-to-polarization leakage predicted from the beam map simulations for BICEP2. The spectra shown here predict the level of BB contamination from the beams the case without any deprojection options, after deprojecting differential pointing (dp), after deprojecting differential pointing and differential relgain (dp+dg), after deprojecting differential pointing, differential relgian, and differential beam width (dp+dg+bw), and finally, after deprojecting differential pointing, differential relgain, and subtracting differential ellipticity (dp+dg+ellip). As we see here, differential beam width for BICEP2 is small, and does not cause large contamination. The residual beam mismatch is at the level of $r \sim 1 \times 10^{-3}$ and is subtracted from the observed CMB data. *Figure from [2].*

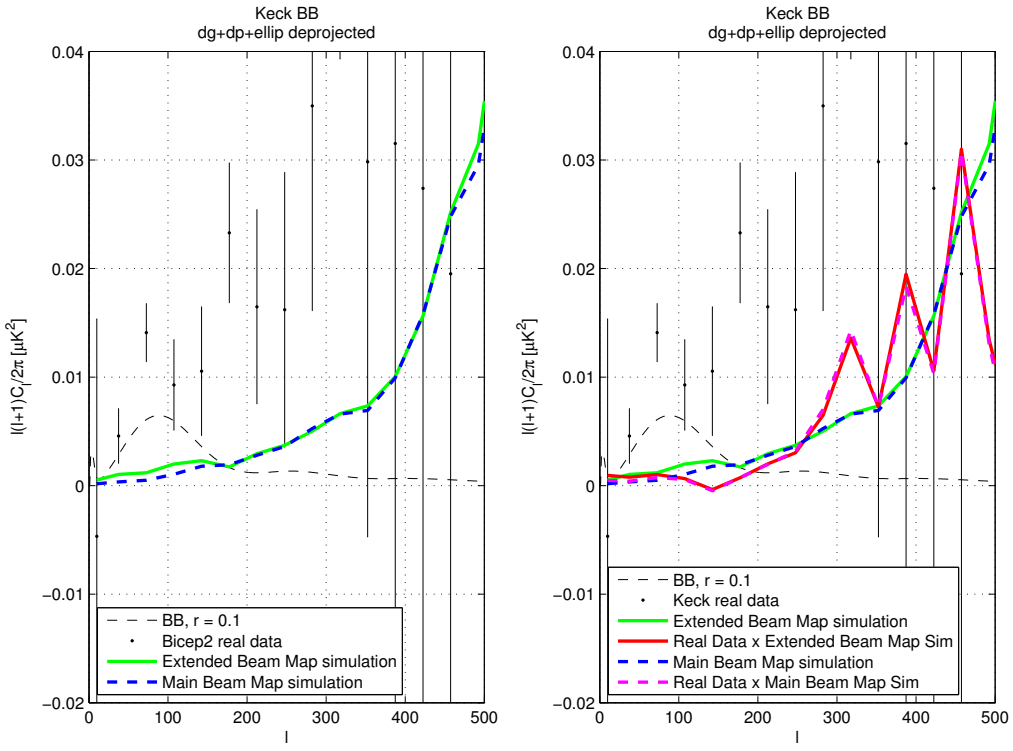

Figure 5.26: Left: Predicted temperature to polarization leakage from using the extended beam map simulations(green), as well as the main beam map simulations (dashed blue) for Keck 2012 and Keck 2013 combined data. Right: Cross spectra between both sets of simulations and observed science data. Although the cross spectra is noisy, the main beam simulations predict real leakage that is consistent within the noise.

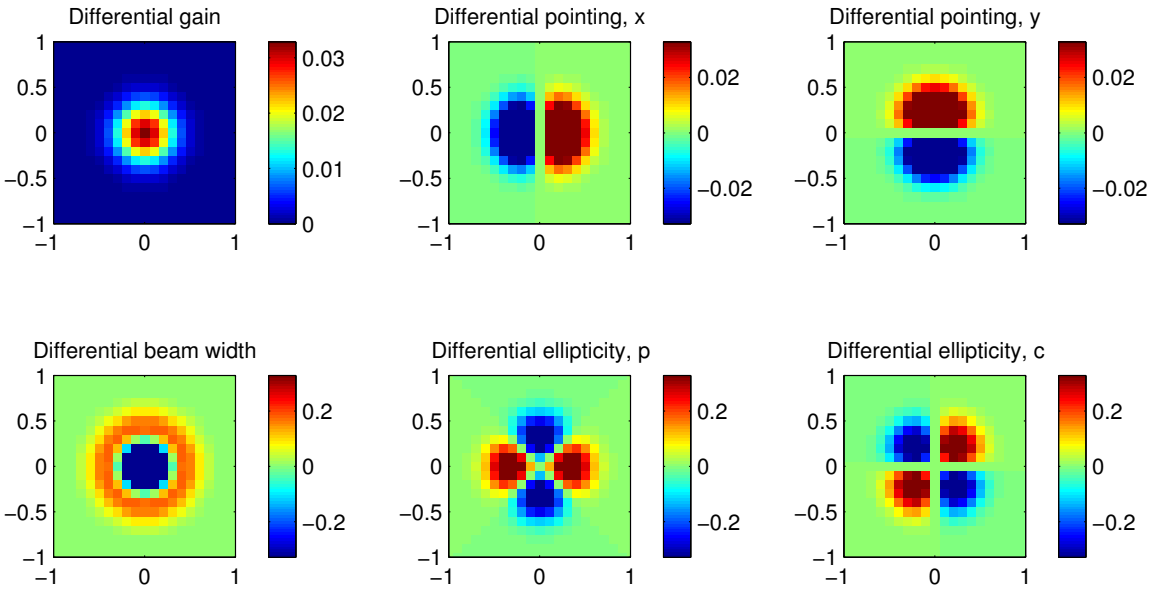

Figure 5.27: The deprojection template for beam maps built using derivatives of a circular Gaussian beam, using the equations in Table 5.1. The template is expected to be equivalent to the template used in the analysis pipeline.

Using the templates in Figure 5.27, we can perform the same deprojections on the beam maps, equivalent to the deprojections that are performed on the observed science data and in the simulations. Instead of deprojecting the timestreams of each detector using a template built from the derivatives of a beam convolved temperature sky, we deproject the beam maps using a template built from the derivatives of a circular Gaussian beam. Following what we do for our science observations, we deproject the differential gain and differential pointing mismatch modes. We also subtract the differential ellipticity mismatch modes. Figure 5.28 show the weighted average of the residual beam mismatch modes across all detectors used in the science analysis (excluding ~ 40 detector pairs ($\sim 2\%$ of detectors) that have bad beam maps).

These stacked residual maps are a measure of the detector-averaged temperature to po-

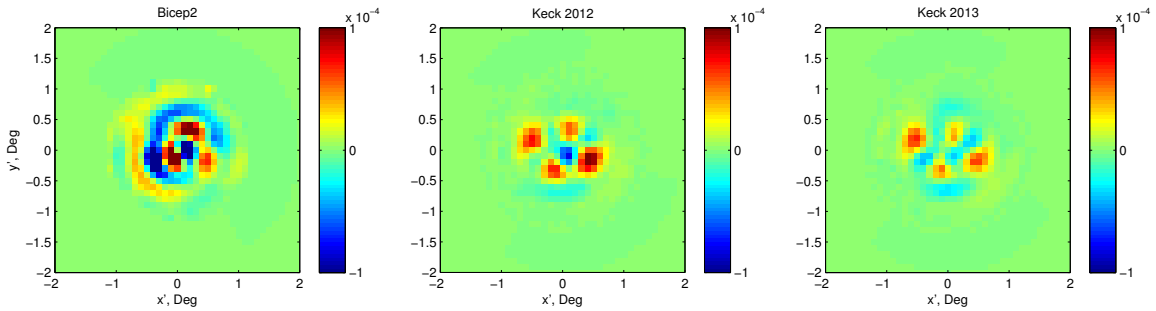

Figure 5.28: The weighted average of the residual beam mismatch modes for BICEP2, Keck 2012 and Keck 2013 over all detectors used in the science analysis (but excluding detectors with bad maps). Differential gain and differential pointing have been deprojected, while the appropriately scaled differential ellipticity has been subtracted. The residual shows a clear pattern above the noise floor.

larization leakage. Depending on the orientation of the map, a convolution of these residual maps with a temperature sky will result in a prediction of the leaked Q or U polarization signal. Therefore, using these beam residual maps, we should be able to predict the resulting temperature to polarization leakage from the detector-averaged beam residual. To do this, we parallel the analysis pipeline and take a Fourier transform of the beam residual map. At specific orientation angles, these transforms measure the fraction of temperature-to-polarization leakage in the Q and U basis. Then, using the Equation 5.1 we can convert this into a prediction of the fraction of leakage induced from temperature to E-mode or B-mode polarization.

Figure 5.29 shows the real part of the 2-dimensional Fourier transform of the stacked beam residual displayed in Figure 5.28. The symmetry of the A and B detectors' polarization orientation results in this particular map orientation measuring the leaked Q signal. The fraction of B-mode polarization signal induced for a given temperature sky (as given by Equation 5.1) is a function of $\sin(2\phi)$. From here, using the deck angles with which we

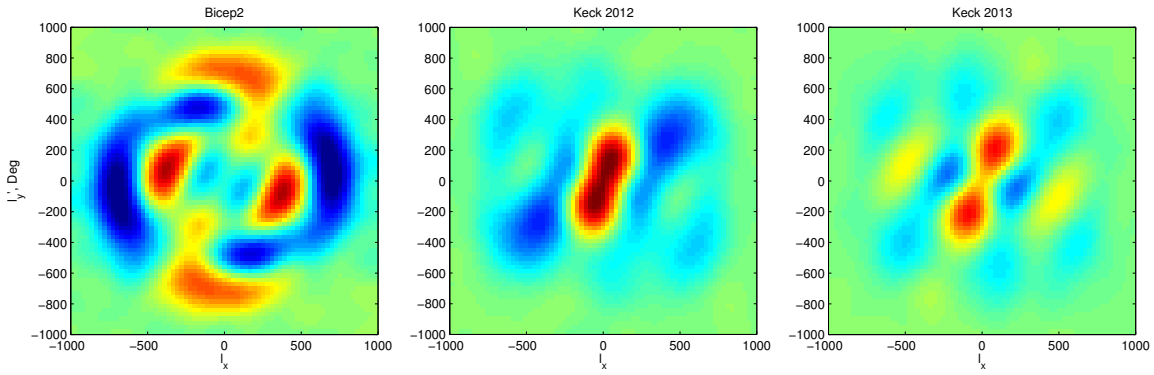

Figure 5.29: Real part of the 2-dimensional Fourier transforms of the residual beam mismatch modes plotted in Figure 5.28. Using these Fourier-transforms, we can predict the residual temperature-to-polarization leakage. The modes along the diagonals correlate with the leakage B-mode polarization, while the modes along the vertical and horizontal correlates with the leaked E-mode polarization.

observe the sky at, we can predict the level of B-mode polarization seen by BICEP2 and the Keck Array.

Figure 5.30 shows the level of predicted leakage estimated from the stacked beam residual for BICEP2. Figure 5.31 shows the level of predicted leakage estimated from the stacked beam residual for Keck 2012 and Keck 2013. On the whole, the stacked beam residual predicts a lower level of BB leakage than the beam map simulation predicts. This is particularly true at high-multipole, and for Keck 2013. This is caused by the more perfect cancellation which occurs when stacking the beams from all the detectors, which does not occur when taking science observations. In CMB data taking, not all the beams overlap with each other, resulting in an imperfect averaging of the systematics. Also, 180 degree rotations in the stacked beam residual will completely cancel the dipole modes, while 180 deck angle rotations during CMB data taking do not overlap each detector exactly on top of itself, again resulting in an imperfect cancellation.

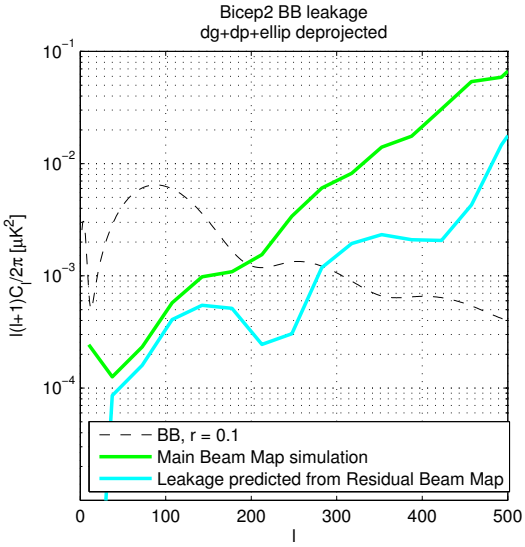

Figure 5.30: The predicted temperature-to-polarization leakage from the beam map residuals for BICEP2. The leakage predicted from the beam map residuals in Figure 5.28 is smaller than the leakage predicted from the beam map simulations. During science data observations, the detectors do not stack perfectly, resulting in less cancellation of the beam mismatch modes than in the stacked beam residual maps.

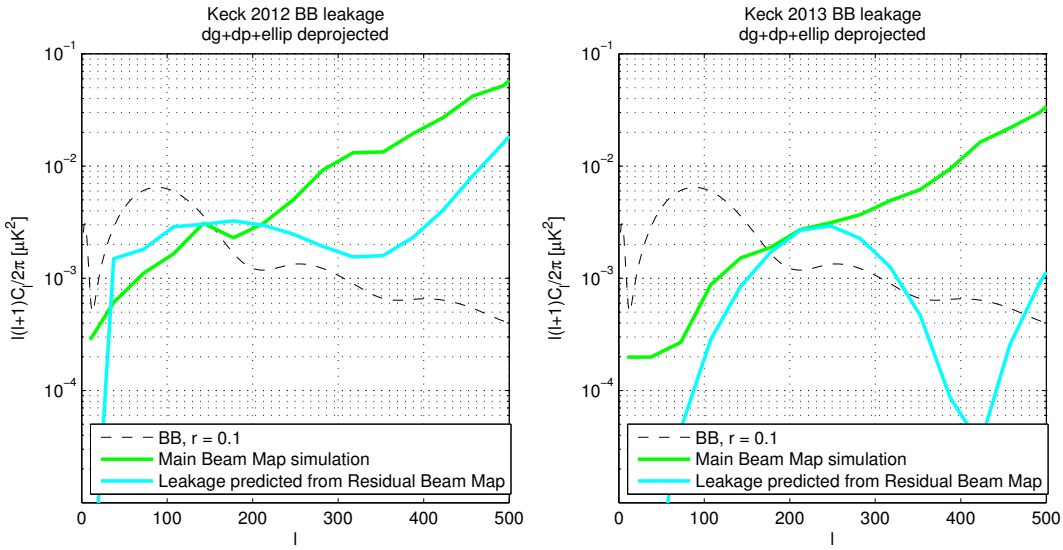

Figure 5.31: The predicted temperature to polarization leakage from the beam map residuals for Keck 2012 on the left, and Keck 2013 on the right. The leakage predicted from the beam map residuals in Figure 5.28 is smaller for $\ell > 200$ than the leakage predicted from the beam map simulations. During CMB observations, the detectors do not stack perfectly, resulting in less cancellation of the beam mismatch modes than in the stacked beam residual maps. The clearly predicted BB leakage at $\ell = 200$ corresponds to the leaked B-mode polarization that correlates to the temperature sky.

A prediction of the beam map simulation for Keck is a non-zero TB spectrum as seen in Figure 5.18. If the non-zero TB spectrum really is due to leaked B-mode polarization from residual beam mismatches, we should be able to predict this spectrum using the stacked beam residuals. Figure 5.32 shows the predicted TB spectrum using the stacked beam residuals. It is interesting to note that the TB spectra is well predicted by both the beam map simulations and in the beam map residuals themselves.

We take advantage of the relatively high signal to noise beam residual map to create a template that we subtract from Keck Array data to remove this residual TB leakage. The subtraction is performed in the timestreams, and the template is generated using the Planck 143 GHz map, flattened and convolved with the residual beam map. We find that this template subtraction does remove the part of the B-mode polarization leakage that correlates with the temperature, thus bringing the TB spectra closer to zero, but does not remove very much of the residual B-mode leakage. This is simply due to the fact that the detector-to-detector variation of the residual temperature to polarization leakage is not taken into account using this method. So in addition to the template subtraction in the timestreams to remove the part of the B-mode polarization leakage that corresponds to the temperature sky, we have to perform a similar subtraction in the BB auto spectra, in the same way we remove the residual leakage for BICEP2.

Figure 5.34 shows the leakage predicted from the beam map simulations for the Keck Array. We deproject the differential pointing and differential gain mismatch modes, but subtract the differential ellipticity modes, as well as the leakage that correlates T to B and is predicted from the stacked beam residual maps. As we can see, the subtraction of the leakage predicted by the stacked residual beam maps is very effective in removing the BB

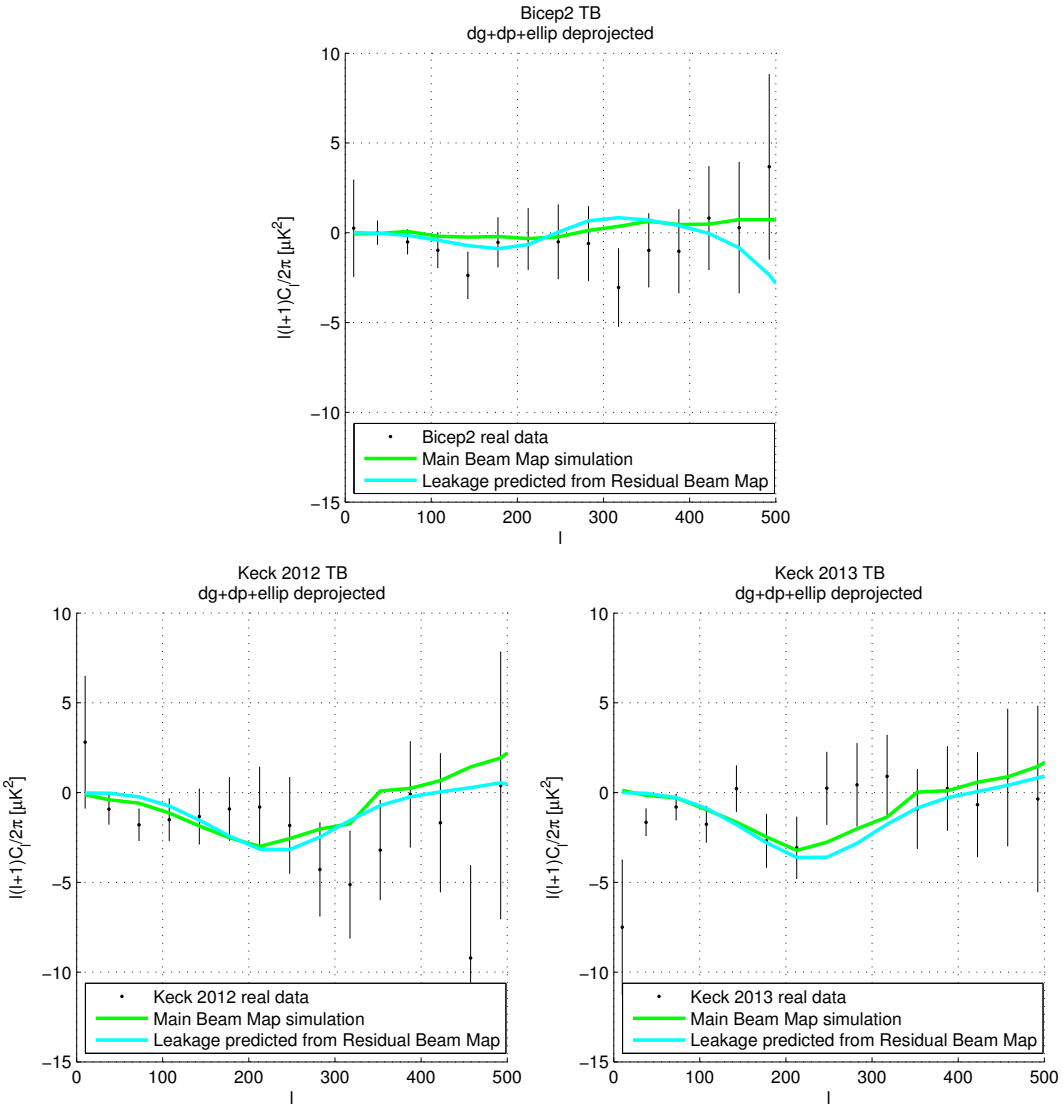

Figure 5.32: Top: The TB spectrum for BICEP2 predicted from the beam map simulations (green) and the BICEP2 beam map residuals (cyan). The BICEP2 beam map residuals do not predict any deviation from zero in the TB spectrum. Bottom: The predicted TB spectrum from the beam map simulations (green) and beam map residuals (cyan) for Keck 2012 on the left, and Keck 2013 on the right. Interestingly, the TB spectrum predicted from the beam map residuals match the TB spectrum predicted in the main beam map simulations, and are reflected in science data. The leaked B-mode polarization signal for Keck is clearly predicted by the stacked beam map residuals, unlike for BICEP2. We use the stacked beam map residuals to build a template to subtract the leaked B-mode polarization that correlates with the temperature signal.

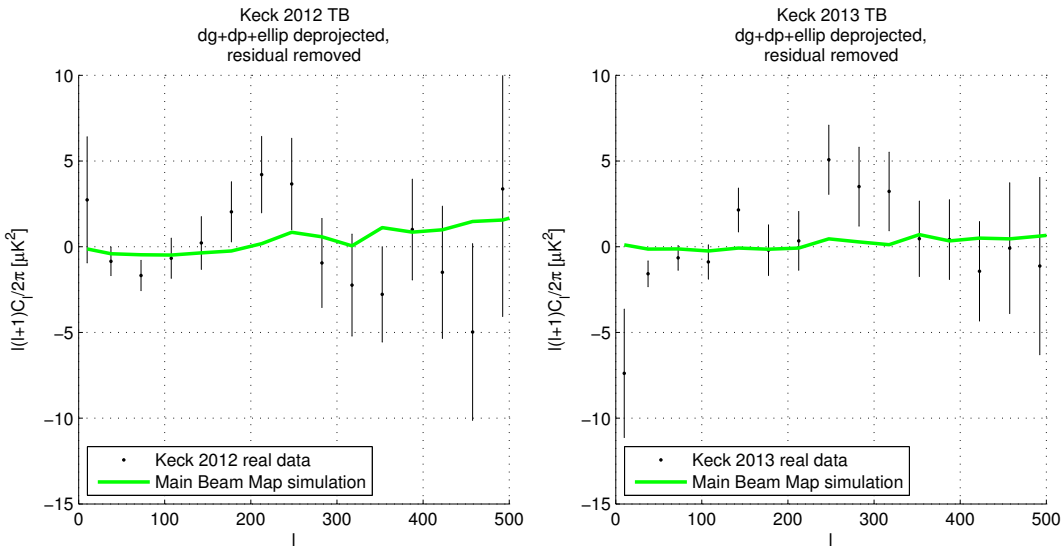

Figure 5.33: The TB spectra for the main beam map simulations as well as for science data for Keck 2012 (left) and Keck 2013 (right) once we subtract the leaked TB signal from the timestreams using the stacked residual beam maps.

leakage that correlates with the temperature sky. The final residual leakage is at the level of $r = 7 \times 10^{-3}$, and we will subtract this leakage from the science observations.

The beam systematics play an important role in understanding the observed science data in BICEP2 and the Keck Array. We are able to quantify and remove the temperature-to-polarization leakage from not only the main beam mismatch modes, but also the higher order beam mismatch modes, ensuring that the resulting measurement of B-mode polarization is free of beam systematics. The techniques discussed here are expected to be used to quantify the leakage predicted by the beam mismatch modes in future experiments.

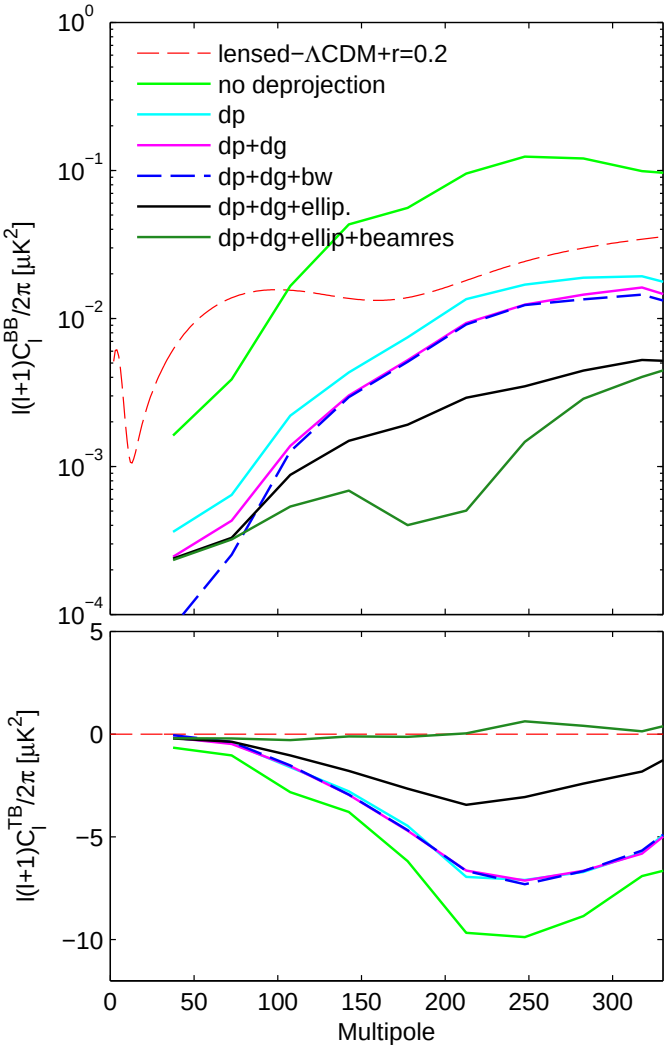

Figure 5.34: Temperature-to-polarization leakage predicted from the beam map simulations for combined Keck Array 2012 and Keck Array 2013 data. The spectra shown here predict the level of contamination from the beams from the case without any deprojection options, after deprojecting differential pointing (dp), after deprojecting differential pointing and differential relgain (dp+dg), after deprojecting differential pointing, differential relgian, and differential beam width (dp+dg+bw), and after deprojecting differential pointing, differential relgain, and subtracting differential ellipticity (dp+dg+ellip). The final line here is the leakage after subtracting the residual derived from the stacked residual beam maps. Subtracting the residual derived from the stacked residual is effective in removing the part of the leakage that correlates T to B. The level of residual BB leakage is at $r = 7 \times 10^{-3}$, and this residual leakage is removed from the observed CMB data. *Figure from [27].*

Chapter 6

BICEP2 and Keck Array results

IN CHAPTER 5 WE SHOW THAT we understand the beam systematics of BICEP2 and Keck well enough to have confidence in the performance of the instrument. We also discuss the analysis pipeline with which we use to analyze real data as well as simulated data. Some of the results from BICEP2 have been presented in Chapter 5.

In this chapter, we present the results of BICEP2 and the Keck Array analysis. We describe briefly the jackknife test statistics, as well as cosmological parameter constraints.

6.1 Maps

BICEP2 took data beginning February 2010 and was decommissioned in November 2012. The summer months of mid-November to mid-February were used for taking summer calibration data. The total integration time is 27×10^6 seconds for the entire season [1]. For BICEP2, we retain 63% of the data collected after relevant cuts have been made to re-

move bad data [1]. The map depth (a measure of the noise in the polarized maps) obtained for BICEP2 is 87 nK·degree over an effective map area of 383.7 square degrees [1, 2].

The Keck Array data presented here and in [42, 27] were taken during the 2012 and 2013 observing season. Total integration time accumulated for the Keck Array is 18×10^6 seconds of data, and after relevant cuts, we retain $\sim 50\%$ of data [42, 27]. The final map depth for the Keck Array maps made from data taken in the 2012 and 2013 observing season is 74nK·degrees across an area of 398 square degrees.

Figure 5.1 shows the T, Q, and U maps that have been made for BICEP2. Figure 6.1 shows the T, Q, and U maps that have been made for the Keck Array 2012 and 2013 observing season. The left column shows signal maps. The polarization maps are dominated by the E-mode polarization signal in the CMB, which appears as vertical/horizontal hatching in the Q maps, and cross-hatching in the U maps. The column on the right shows the temporal split jackknife map. Any visible signal that appears in the jackknife maps is an indication of a possible systematic, as true signals should be in both halves of the jackknife, and therefore subtract away. The jackknife map appears consistent with noise.

Figure 5.2 are BICEP2 E-mode and B-mode maps made from the Q and U polarization maps shown in Figure 5.1. Figure 6.2 are the Keck Array E-mode and B-mode maps made from the Q and U polarization maps shown in Figure 6.1. The maps have been filtered to only show structure for $50 < \ell < 120$, and are made from Fourier transforms of the Q and U maps. The left column shows the observed CMB signal, while the right column is the E-mode and B-mode signal shown for a simulated signal + noise sky with no inherent B-mode polarization. Standard ΛCDM cosmology does not include tensor B-modes and so the B-mode map for BICEP2 and Keck Array show an excess signal.

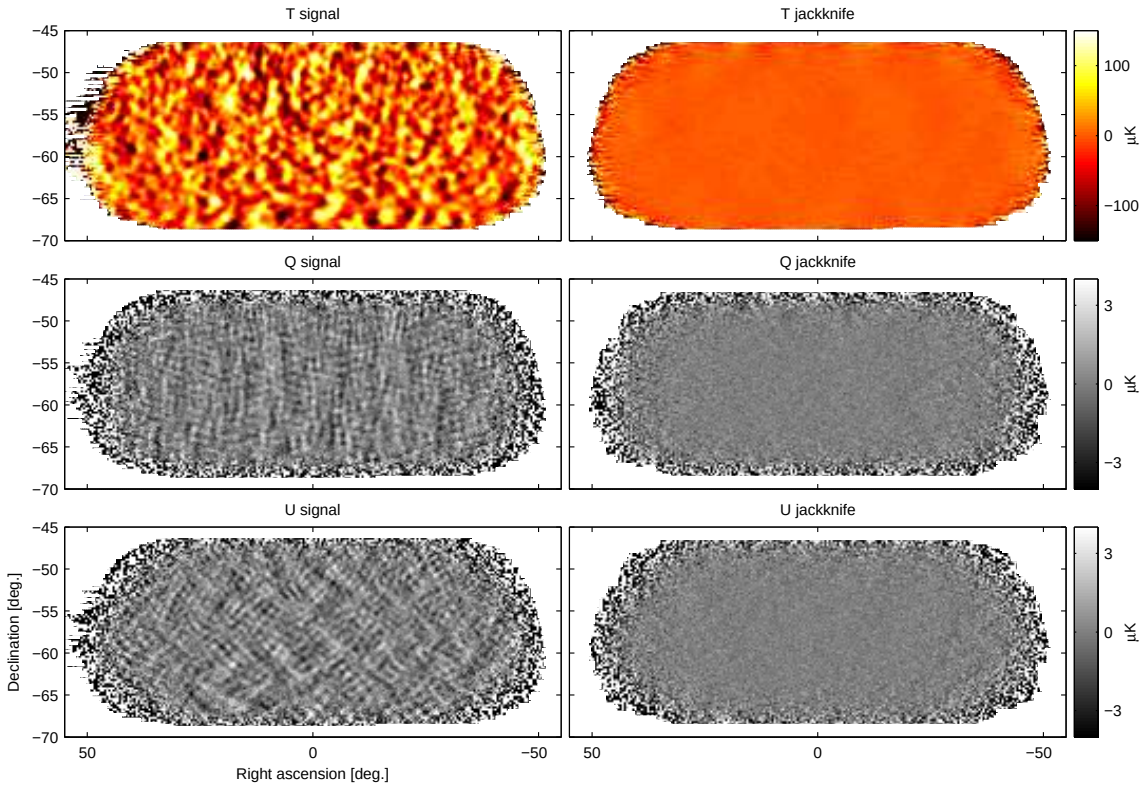

Figure 6.1: T, Q, and U maps for the Keck Array 2012 and 2013 observing season. The left column shows signal maps, and the right column shows the temporal jackknife maps of the first and second half of the season. The jackknife maps are clean and show no contamination. The Q and U patterns are dominated by E-mode polarization in the CMB sky. *Figure from [27].*

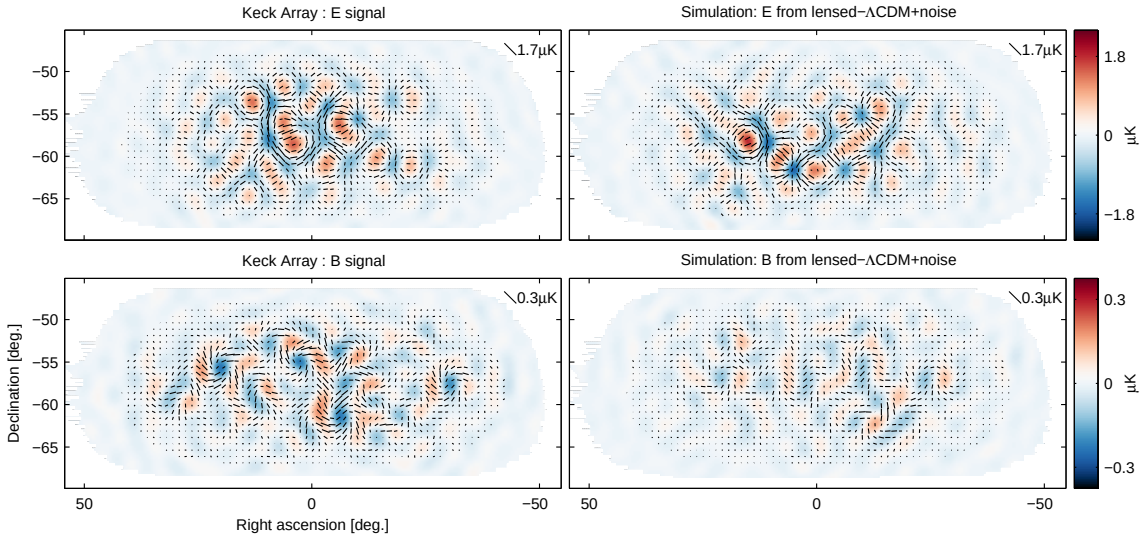

Figure 6.2: E-mode and B-mode polarization maps made from the Keck Array 2012 and 2013 Q and U maps displayed in Figure 6.1. The maps have been filtered to only show structure for $50 < \ell < 120$, and are made from Fourier transforms of the Q and U maps. The left column shows the observed CMB signal, while the right column is the E-mode and B-mode signal shown for a simulated signal + noise sky with no inherent B-mode polarization. *Figure from [27].*

6.2 Power Spectra/Cross Spectra

We calculate power spectra in the process described in Section 5.1.5.

Figure 5.3 shows the power spectra that we obtain from the BICEP2 maps (black points). Figure 6.3 shows the power spectra that we obtain for the Keck Array data. We evaluate all six TT, TE, EE, BB, TB, and EB spectra. The solid red lines indicate the spectra predicted by standard ΛCDM-cosmology (including lensing). The dashed red line indicates a tensor mode at $r = 0.2$. The blue points are jackknife spectra for a single jackknife (the temporal-split jackknife). The error bars are obtained from the signal+noise simulations described in Section 5.2. Also noted in the figure are the probability to exceed values (PTE) evaluated against the simulations of standard ΛCDM-cosmology.

For BICEP2 (Figure 5.3), the residual temperature-to-polarization leakage from beam mismatch modes has been removed from the observed CMB data. For Keck (Figure 6.3), the residual temperature-to-polarization leakage has not yet been removed.

For both BICEP2 and the Keck Array, the TT, TE, and EE spectra look consistent with expectations from ΛCDM-cosmology. The TB and EB spectra are consistent with null, partly as a result of the overall polarization calibration that we perform, which forces these spectra to be zero, consistent with expectations from ΛCDM. At $\ell = 200$ and above, the BB spectra looks consistent with lensed-ΛCDM: the lensing BB spectrum is expected from gravitational lensing of E-mode polarization into B-mode polarization. At low ℓ, the BB spectra for BICEP2 and the Keck Array show an excess of signal above the expected lensed-ΛCDM BB spectrum. Considering the first nine band powers ($0 < \ell < 300$) for BICEP2, we calculate PTE of 1.3×10^{-7}, a significance of 5.3σ. A thorough description of the BICEP2 spectra can be found in [2], while the Keck Array spectra is discussed in [27].

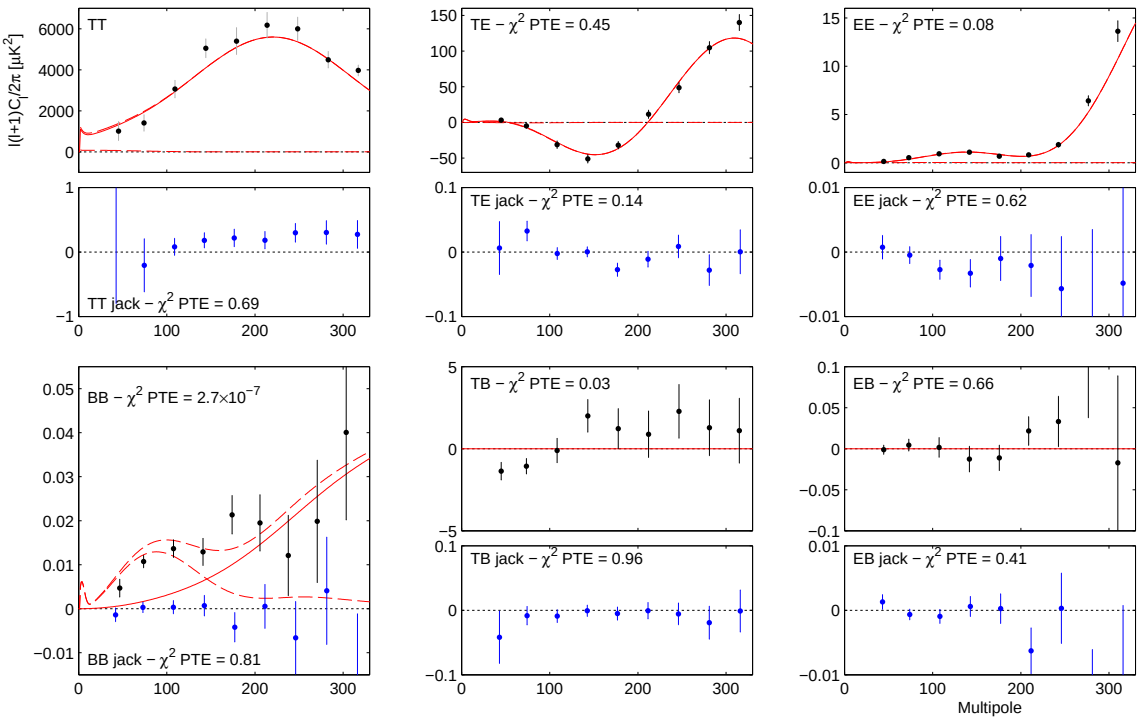

Figure 6.3: Keck Array power spectra. The black points indicate observed CMB data after the filter-beam correction and noise debias has been applied. The blue points are spectra taken from jackknifes. As shown, we expect the jackknifes to show no signals whatsoever. The red line indicates theory curves. *Figure from [27].*

6.3 Jackknife Tests and Systematic Levels

We describe the jackknife tests in Section 5.1.4. The jackknife tests are our most sensitive tests against systematics. In order to understand the jackknife spectra of real data, we test the jackknife spectra of real data against the simulations using a χ^2 statistic as shown in Equation 6.1.

$$\chi^2 = (\mathbf{d} - \langle \mathbf{m} \rangle)^{\mathrm{T}} \mathbf{D}^{-1} (\mathbf{d} - \langle \mathbf{m} \rangle) \tag{6.1}$$

where $\mathbf{d}$ is the observed data, $\langle \mathbf{m} \rangle$ is the mean of the lensed-ΛCDM+noise simulations and $\mathbf{D}$ is the bandpower covariance matrix evaluated from the simulations. We calculate χ^2 for each of the simulations as well, and from this set of χ^2 numbers, we calculate the probability-to-exceed (PTE). We also calculate a χ statistic

$$\chi = \sum_i \frac{d_i - \langle m_i \rangle}{\sigma_{m_i}} \tag{6.2}$$

where d_i are the real data bandpower values, m_i and σ_{m_i} are the mean and standard deviation of the simulations. A full description of the jackknife PTEs can be found in [2].

The jackknife PTEs are calculated for all spectra for all the jackknives, as well as for the non-jackknifed spectra. The χ^2 and χ statistics are evaluated for the first five bins ($0 < \ell < 200$) as well as for the first nine bins ($0 < \ell < 300$). The EE, EB, and BB jackknife spectra are presented in [2], and are found to have a rather uniform distribution of values.

We evaluate the systematics of the telescope in great detail, using a combination of calibration measurements and simulations. In Figure 6.4, we show that for BICEP2, the expected polarization leakage due to various instrumental systematics is low. The internal parts of the Keck Array telescopes are designed to be almost exactly the same as the BICEP2

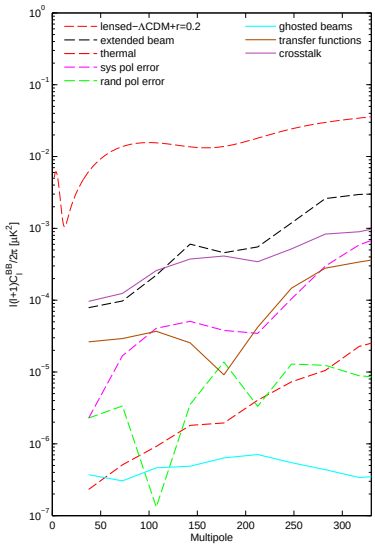

Figure 6.4: Expected contamination levels from various instrumental systematics for BICEP2. Solid lines are an indication of expected leakage, while the dashed lines are upper limits on the expected leakage from the relevant systematic. The dashed red line is the B-mode spectra expected for tensor modes at $r = 0.2$. *Figure from [2].*

telescope and so we expect that the systematics levels for Keck is similar to the systematics levels for BICEP2.

6.4 Cross Spectra

We can take cross spectra of BICEP2 with data from BICEP1. Despite the design similarities of the telescope and overall approach, the detectors used in BICEP1 and BICEP2 use completely different technologies. BICEP1 used feedhorn-coupled semiconductor bolometers, while BICEP2 used planar-antenna array coupled to transition-edge sensor bolometers. Cross spectra that show both BICEP1 and BICEP2 observing the same signals are a strong argument against the possibility of the signal being caused by instrumental effects.

Figure 6.5 shows the cross spectra of BICEP2 and BICEP1. BICEP1 operated at 100

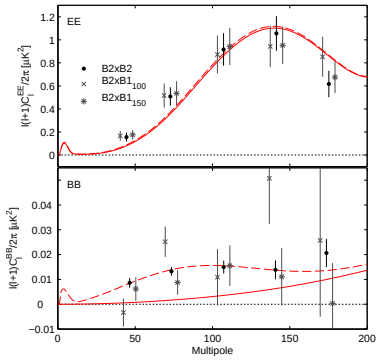

Figure 6.5: The EE and BB cross spectra of BICEP2 and BICEP1 data at 100 GHz and 150 GHz. The error bars are the standard deviations of the simulations, the red lines indicate the spectra expected from lensed-ΛCDMcosmology, while the dashed red line indicates the spectrum expected with the addition of tensors at $r = 0.2$. *Figure from [2].*

GHz as well as 150 GHz, and so we take cross spectra at both frequencies. The errorbars are the standard deviation of the signal and noise simulations The correlation in the EE spectra confirms that the procedure is working as expected. The BB cross spectra are noisier and we calculate the χ^2 and χ values against the spectra expected for lensed-ΛCDM. BICEP2 $\times$ BICEP1$_{150}$ has PTEs of 0.37 and 0.05 respectively, while the BICEP2 $\times$ BICEP1$_{100}$ spectrum has PTEs of 0.005 and 0.001, which show some evidence correlated signal in both BICEP1 and BICEP2. A discussion of the cross spectra can be found in [2].

6.5 Conclusion

In this thesis we have discussed the scientific motivations behind the BICEP2 and Keck Array experiments as well as the experiments themselves with a focus on the optics. We presented an extensive study of the beam characterization of every detector in BICEP2 and the Keck Array. Since understanding the beam response of the detectors is critical

to understanding the data we take, we have taken advantage of our small aperture and relatively short far-field to map each detector's beam with high signal-to-noise. Using these maps, we predicted the temperature-to-polarization leakage from main mismatch modes of the beam as well as the higher-order terms. Once the main beam mismatch modes have been removed in the analysis, we find that the temperature-to-polarization leakage from the residual beam mismatch modes in both BICEP2 and the Keck Array is small. We remove the residual leakage in the BICEP2 analysis so that there remains no temperature-to-polarization leakage from beam mismatches in the CMB data. The Keck analysis is ongoing, but we expect to also remove the predicted temperature-to-polarization leakage from the data.

So we close with what we started with: Figure 6.6. BICEP2 has detected B-mode polarization at degree angular scales. In [2], these results are discussed in detail. In [2] and [24], we present the systematic studies and jackknife tests that show that the systematics of the telescope is well enough understood and controlled such that the temperature-to-polarization leakage from the systematics is much lower than the signal detected. In this thesis, we have focussed on understanding the beam systematics of the telescope and ensuring that the temperature-to-polarization leakage from the beam mismatches is removed from the CMB data. Since BICEP2 only observed at a single frequency, however, it is unclear that the signal detected is entirely from inflation. More data from various experiments is required to fully understand the signal that BICEP2 has detected.

The Keck Array results using 150 GHz data from the 2012 and 2013 observing season will be published soon. The beam characterization and systematics presented in this thesis for Keck feeds into this analysis.

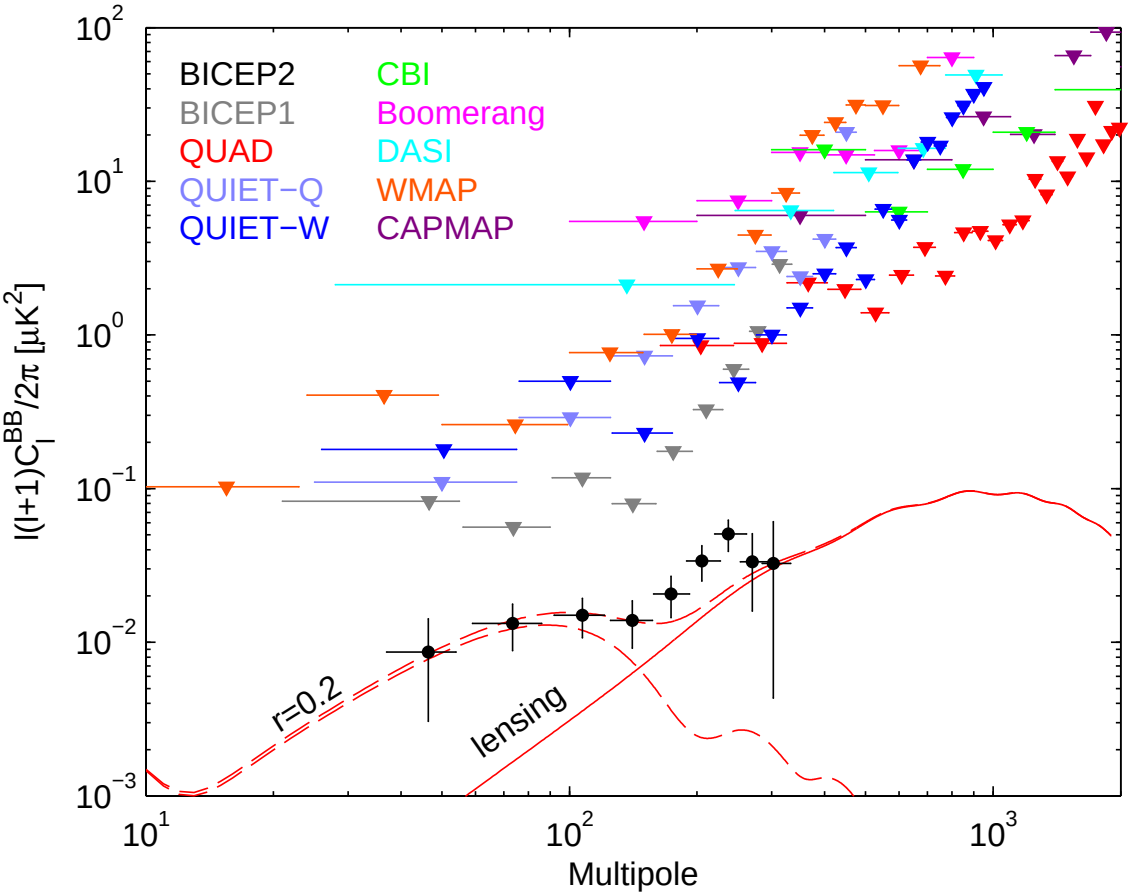

Figure 6.6: The B-modepolarization power spectrum as measured by BICEP2. The power spectrum is well fit by a primordial gravitational wave spectrum with tensor to ratio of $r = 0.2$, with no foreground subtraction. *Figure from [2].*

Currently, the Keck Array is operating with two receivers at 100 GHz, while the other three are still at 150 GHz. In addition to the Keck Array, BICEP3, the next telescope in the BICEP series of experiments, is planning to deploy at the end of 2014 with 2500 detector pairs at 100 GHz. Data from the Keck Array and BICEP3 at 100 GHz will allow us to further understand the signal that BICEP2 has found.

Bibliography

[1] P. A. R. Ade, R. W. Aikin, M. Amiri, D. Barkats, S. J. Benton, C. A. Bischoff, J. J. Bock, J. A. Brevik, I. Buder, E. Bullock, G. Davis, P. K. Day, C. D. Dowell, L. Duband, J. P. Filippini, S. Fliescher, S. R. Golwala, M. Halpern, M. Hasselfield, S. R. Hildebrandt, G. C. Hilton, K. D. Irwin, K. S. Karkare, J. P. Kaufman, B. G. Keating, S. A. Kernasovskiy, J. M. Kovac, C. L. Kuo, E. M. Leitch, N. Llombart, M. Lueker, C. B. Netterfield, H. T. Nguyen, R. O'Brient, IV R. W. Ogburn, A. Orlando, C. Pryke, C. D. Reintsema, S. Richter, R. Schwarz, C. D. Sheehy, Z. K. Staniszewski, K. T. Story, R. V. Sudiwala, G. P. Teply, J. E. Tolan, A. D. Turner, A. G. Vieregg, P. Wilson, C. L. Wong, K. W. Yoon, and Bicep2 Collaboration. Bicep2. ii. experiment and three-year data set. *The Astrophysical Journal*, 792(1):62, 2014.

[2] P. A. R. Ade, R. W. Aikin, D. Barkats, S. J. Benton, C. A. Bischoff, J. J. Bock, J. A. Brevik, I. Buder, E. Bullock, C. D. Dowell, L. Duband, J. P. Filippini, S. Fliescher, S. R. Golwala, M. Halpern, M. Hasselfield, S. R. Hildebrandt, G. C. Hilton, V. V. Hristov, K. D. Irwin, K. S. Karkare, J. P. Kaufman, B. G. Keating, S. A. Kernasovskiy, J. M. Kovac, C. L. Kuo, E. M. Leitch, M. Lueker, P. Mason, C. B. Netterfield, H. T. Nguyen, R. O'Brient, R. W. Ogburn, A. Orlando, C. Pryke, C. D. Reintsema, S. Richter, R. Schwarz, C. D. Sheehy, Z. K. Staniszewski, R. V. Sudiwala, G. P. Teply, J. E. Tolan, A. D. Turner, A. G. Vieregg, C. L. Wong, K. W. Yoon, and Bicep2 Collaboration. Detection of B-Mode Polarization at Degree Angular Scales by BICEP2. *Physical Review Letters*, 112(24):241101, June 2014.

[3] Peter A. R. Ade, Giampaolo Pisano, Carole Tucker, and Samuel Weaver. A review of metal mesh filters. *Proc. SPIE*, 6275:62750U–62750U–15, 2006.

[4] R. W. Aikin. *Testing Inflationary Cosmology with the Bicep1 and Bicep2 Experiments*. PhD thesis, California Institute of Technology, 2013.

[5] R. W. Aikin et al. Optical performance of the BICEP2 Telescope at the South Pole. *Millimeter, Submillimeter, and Far-Infrared Detectors and Instrumentation for Astronomy V*, 7741(1):77411G, 2010.

[6] D. Barkats, R. Aikin, C. Bischoff, I. Buder, J. P. Kaufman, B. G. Keating, J. M. Kovac, M. Su, P. A. R. Ade, J. O. Battle, E. M. Bierman, J. J. Bock, H. C. Chiang, C. D. Dowell, L. Duband, J. Filippini, E. F. Hivon, W. L. Holzapfel, V. V. Hristov, W. C. Jones,

C. L. Kuo, E. M. Leitch, P. V. Mason, T. Matsumura, H. T. Nguyen, N. Ponthieu, C. Pryke, S. Richter, G. Rocha, C. Sheehy, S. S. Kernasovskiy, Y. D. Takahashi, J. E. Tolan, and K. W. Yoon. Degree-scale cosmic microwave background polarization measurements from three years of bicep1 data. *The Astrophysical Journal*, 783(2):67, 2014.

[7] D. Barkats, C. Bischoff, P. Farese, L. Fitzpatrick, T. Gaier, J. O. Gundersen, M. M. Hedman, L. Hyatt, J. J. McMahon, D. Samtleben, S. T. Staggs, K. Vanderlinde, and B. Winstein. First Measurements of the Polarization of the Cosmic Microwave Background Radiation at Small Angular Scales from CAPMAP. *Astrophys. J. Lett.* , 619:L127–L130, February 2005.

[8] E. S. Battistelli et al. Functional description of read-out electronics for time-domain multiplexed bolometers for millimeter and sub-millimeter astronomy. *J. Low Temp. Phys.*, 151:908–914, 2008.

[9] D. Baumann and H. V. Peiris. Cosmological Inflation: Theory and Observations. *ArXiv e-prints*, October 2008.

[10] C. L. Bennett, D. Larson, J. L. Weiland, N. Jarosik, G. Hinshaw, N. Odegard, K. M. Smith, R. S. Hill, B. Gold, M. Halpern, E. Komatsu, M. R. Nolta, L. Page, D. N. Spergel, E. Wollack, J. Dunkley, A. Kogut, M. Limon, S. S. Meyer, G. S. Tucker, and E. L. Wright. Nine-year wilkinson microwave anisotropy probe (wmap) observations: Final maps and results. *The Astrophysical Journal Supplement Series*, 208(2):20, 2013.

[11] C. Bischoff, L. Hyatt, J. J. McMahon, G. W. Nixon, D. Samtleben, K. M. Smith, K. Vanderlinde, D. Barkats, P. Farese, T. Gaier, J. O. Gundersen, M. M. Hedman, S. T. Staggs, B. Winstein, and CAPMAP Collaboration. New Measurements of Fine-Scale CMB Polarization Power Spectra from CAPMAP at Both 40 and 90 GHz. *Astrophys. J.* , 684:771–789, September 2008.

[12] J. J. Bock. The promise of bolometers for CMB polarimetry. *Proc. SPIE Int. Soc. Opt. Eng.*, 4843:314–323, February 2003.

[13] K. J. Bradford. *A Rotating Polarized Source: Instrumentation Development for Precision Calibration of Cosmic Microwave Background (CMB) Polarimeters at the South Pole*. PhD thesis, Harvard University, 2012.

[14] J. A. Brevik, R. W. Aikin, M. Amiri, S. J. Benton, J. J. Bock, J. A. Bonetti, B. Burger, C. D. Dowell, L. Duband, J. P. Filippini, S. R. Golwala, M. Halpern, M. Hasselfield, G. Hilton, V. V. Hristov, K. Irwin, J. P. Kaufman, B. G. Keating, J. M. Kovac, C. L. Kuo, A. E. Lange, E. M. Leitch, C. B. Netterfield, H. T. Nguyen, R. W. Ogburn IV, A. Orlando, C. Pryke, C. Reintsema, S. Richter, J. E. Ruhl, M. Runyan, C. Sheehy,

Z. Staniszewski, R. Sudiwala, J. E. Tolan, A. D. Turner, P. Wilson, and C. L. Wong. Initial performance of the bicep2 antenna-coupled superconducting bolometers at the south pole. *Proc. SPIE*, 7741:77411H–77411H–10, 2010.

[15] M. L. Brown, P. Ade, J. Bock, M. Bowden, G. Cahill, P. G. Castro, S. Church, T. Culverhouse, R. B. Friedman, K. Ganga, W. K. Gear, S. Gupta, J. Hinderks, J. Kovac, A. E. Lange, E. Leitch, S. J. Melhuish, Y. Memari, J. A. Murphy, A. Orlando, et al. Improved Measurements of the Temperature and Polarization of the Cosmic Microwave Background from QUaD. *Astrophys. J.* , 705:978–999, November 2009.

[16] A. Challinor. Anisotropies in the Cosmic Microwave Background. *ArXiv Astrophysics e-prints*, March 2004.

[17] Richard A Chamberlin, Adair P Lane, and Antony A Stark. The 492 ghz atmospheric opacity at the geographic south pole. *The Astrophysical Journal*, 476(1):428, 1997.

[18] Liu Chao. Detection of b-mode polarization in the cosmic microwave background using bicep2: Vacuum window construction and performance. *Caltech's Summer Undergraduate Research Report*, 2009.

[19] H. C. Chiang, P. A. R. Ade, D. Barkats, J. O. Battle, E. M. Bierman, J. J. Bock, C. D. Dowell, L. Duband, E. F. Hivon, W. L. Holzapfel, V. V. Hristov, W. C. Jones, B. G. Keating, J. M. Kovac, C. L. Kuo, A. E. Lange, E. M. Leitch, P. V. Mason, T. Matsumura, H. T. Nguyen, N. Ponthieu, C. Pryke, S. Richter, G. Rocha, C. Sheehy, Y. D. Takahashi, J. E. Tolan, and K. W. Yoon. Measurement of Cosmic Microwave Background Polarization Power Spectra from Two Years of BICEP Data. *Astrophys. J.* , 711:1123–1140, March 2010.

[20] S. Das, T. Louis, M. R. Nolta, G. E. Addison, E. S. Battistelli, J. R. Bond, E. Calabrese, D. Crichton, M. J. Devlin, S. Dicker, J. Dunkley, R. Dünner, J. W. Fowler, M. Gralla, A. Hajian, M. Halpern, M. Hasselfield, M. Hilton, A. D. Hincks, R. Hlozek, et al. The Atacama Cosmology Telescope: temperature and gravitational lensing power spectrum measurements from three seasons of data. *J. Cosmol. Astropart. Phys.*, 4:14, April 2014.

[21] P. A. J. de Korte, J. Beyer, S. Deiker, G. C. Hilton, K. D. Irwin, M. Macintosh, S. W. Nam, C. D. Reintsema, L. R. Vale, and M. E. Huber. Time-division superconducting quantum interference device multiplexer for transition-edge sensors. *Review of Scientific Instruments*, 74:3807–3815, August 2003.

[22] Lionel Duband and Bernard Collaudin. Sorption coolers development at cea-sbt. *Cryogenics*, 39(8):659–663, 1999.

[23] J. W. Ekin. *Experimental techniques for low-temperature measurements: Cryostat design, material properties, and superconductor critical-current testing*. Oxford: Oxford University Press, 2006.

[24] BICEP2 Collaboration et al. BICEP2 III: Systematics. *In prep.*, 2014.

[25] BICEP2 Collaboration et al. BICEP2 IV: Beams. *In prep.*, 2014.

[26] BICEP2 Collaboration et al. BICEP2 V: Detectors. *In prep.*, 2014.

[27] BICEP2 Collaboration et al. Keck First Results. *In prep.*, 2014.

[28] Douglas P. Finkbeiner, Marc Davis, and David J. Schlegel. Extrapolation of Galactic Dust Emission at 100 Microns to CMBR Frequencies Using FIRAS. *Astrophys. J.*, 524:867–886, 1999.

[29] D. J. Fixsen. The Temperature of the Cosmic Microwave Background. *Astrophys. J.* , 707:916–920, December 2009.

[30] A. H. Guth. Inflationary universe: A possible solution to the horizon and flatness problems. *Phys. Rev. D* , 23:347–356, January 1981.

[31] E. Hecht. *Optics 3rd Edition*. Addison Wesley Longman Inc, 1998.

[32] G. Hinshaw, D. Larson, E. Komatsu, D. N. Spergel, C. L. Bennett, J. Dunkley, M. R. Nolta, M. Halpern, R. S. Hill, N. Odegard, L. Page, K. M. Smith, J. L. Weiland, B. Gold, N. Jarosik, A. Kogut, M. Limon, S. S. Meyer, G. S. Tucker, E. Wollack, and E. L. Wright. Nine-year Wilkinson Microwave Anisotropy Probe (WMAP) Observations: Cosmological Parameter Results. *Astrophys. J. Suppl.* , 208:19, October 2013.

[33] Z. Hou, C. L. Reichardt, K. T. Story, B. Follin, R. Keisler, K. A. Aird, B. A. Benson, L. E. Bleem, J. E. Carlstrom, C. L. Chang, H.-M. Cho, T. M. Crawford, A. T. Crites, T. de Haan, R. de Putter, M. A. Dobbs, S. Dodelson, J. Dudley, E. M. George, N. W. Halverson, et al. Constraints on Cosmology from the Cosmic Microwave Background Power Spectrum of the 2500 deg^2 SPT-SZ Survey. *Astrophys. J.* , 782:74, February 2014.

[34] W. Hu and M. White. A CMB polarization primer. *New Astron.* , 2:323–344, October 1997.

[35] K. D. Irwin. An application of electrothermal feedback for high resolution cryogenic particle detection. *Appl. Phys. Lett.* , 66:1998–2000, April 1995.

[36] K. D. Irwin, L. R. Vale, N. E. Bergren, S. Deiker, E. N. Grossman, G. C. Hilton, S. W. Nam, C. D. Reintsema, D. A. Rudman, and M. E. Huber. Time-division SQUID multiplexers. *Low Temperature Detectors*, 605:301–304, February 2002.

[37] K.D. Irwin and G.C. Hilton. Transition-edge sensors. In Christian Enss, editor, *Cryogenic Particle Detection*, volume 99 of *Topics in Applied Physics*, pages 63–150. Springer Berlin Heidelberg, 2005.

[38] M. Kamionkowski, A. Kosowsky, and A. Stebbins. A Probe of Primordial Gravity Waves and Vorticity. *Phys. Rev. Lett.* , 78:2058–2061, March 1997.

[39] B. G. Keating, P. A. R. Ade, J. J. Bock, E. Hivon, W. L. Holzapfel, A. E. Lange, H. Nguyen, and K. W. Yoon. BICEP: a large angular scale CMB polarimeter. *Proc. SPIE Int. Soc. Opt. Eng.*, 4843:284, February 2003.

[40] B. G. Keating, M. Shimon, and A. P. S. Yadav. Self-calibration of Cosmic Microwave Background Polarization Experiments. *Astrophys. J. Lett.* , 762:L23, January 2013.

[41] S. Kernasovskiy, P. A. R. Ade, R. W. Aikin, M. Amiri, S. Benton, C. Bischoff, J. J. Bock, J. A. Bonetti, J. A. Brevik, B. Burger, G. Davis, C. D. Dowell, L. Duband, J. P. Filippini, S. Fliescher, S. R. Golwala, M. Halpern, M. Hasselfield, G. Hilton, V. V. Hristov, K. Irwin, J. M. Kovac, C. L. Kuo, E. Leitch, M. Lueker, C. B. Netterfield, H. T. Nguyen, R. O'Brient, R. W. Ogburn, C. L. Pryke, C. Reintsema, J. E. Ruhl, M. C. Runyan, R. Schwarz, C. D. Sheehy, Z. Staniszewski, R. Sudiwala, G. Teply, J. E. Tolan, A. D. Turner, A. Vieregg, D. V. Wiebe, P. Wilson, and C. L. Wong. Optimization and sensitivity of the keck array. *Proc. SPIE*, 8452:84521B–84521B–12, 2012.

[42] S. A. S. Kernasovskiy. *Measuring the Polarization of the Cosmic Microwave Background with the Keck Array and Bicep2*. PhD thesis, Stanford University, 2014.

[43] J. M. Kovac and D. Barkats. CMB from the South Pole: Past, Present, and Future. *ArXiv e-prints*, July 2007.

[44] J. M. Kovac, E. M. Leitch, C. Pryke, J. E. Carlstrom, N. W. Halverson, and W. L. Holzapfel. Detection of polarization in the cosmic microwave background using DASI. *Nature (London)*, 420:772, December 2002.

[45] L. M. Krauss and F. Wilczek. Using cosmology to establish the quantization of gravity. *Phys. Rev. D* , 89(4):047501, February 2014.

[46] J. W. Lamb. Miscellaneous data on materials for millimetre and submillimetre optics. *International Journal of Infrared and Millimeter Waves*, 17:1997–2034, December 1996.

[47] A. D. Linde. A new inflationary universe scenario: A possible solution of the horizon, flatness, homogeneity, isotropy and primordial monopole problems. *Phys. Lett. B*, 108:389–393, February 1982.

[48] T. E. Montroy, P. A. R. Ade, J. J. Bock, J. R. Bond, J. Borrill, A. Boscaleri, P. Cabella, C. R. Contaldi, B. P. Crill, P. de Bernardis, G. De Gasperis, A. de Oliveira-Costa, G. De Troia, G. di Stefano, E. Hivon, A. H. Jaffe, T. S. Kisner, W. C. Jones, A. E. Lange, S. Masi, et al. A Measurement of the CMB <EE> Spectrum from the 2003 Flight of BOOMERANG. *Astrophys. J.* , 647:813–822, August 2006.

[49] S. Naess, M. Hasselfield, J. McMahon, M. D. Niemack, G. E. Addison, P. A. R. Ade, R. Allison, M. Amiri, A. Baker, N. Battaglia, J. A. Beall, F. de Bernardis, J. Bond, J. Britton, E. Calabrese, H.-m. Cho, K. Coughlin, D. Crichton, S. Das, R. Datta, M. J. Devlin, S. R. Dicker, J. Dunkley, R. Dünner, J. W. Fowler, A. E. Fox, P. Gallardo, E. Grace, M. Gralla, A. Hajian, M. Halpern, S. Henderson, J. C. Hill, G. C. Hilton, M. Hilton, A. D. Hincks, R. Hlozek, P. Ho, J. Hubmayr, K. M. Huffenberger, J. P. Hughes, L. Infante, K. Irwin, R. Jackson, J. Klein, B. Koopman, A. Kosowsky, D. Li, T. Louis, M. Lungu, M. Madhavacheril, T. A. Marriage, L. Maurin, F. Menanteau, K. Moodley, C. Munson, L. Newburgh, J. Nibarger, M. R. Nolta, L. A. Page, C. Pappas, B. Partridge, F. Rojas, B. Schmitt, N. Sehgal, B. D. Sherwin, J. Sievers, S. Simon, D. N. Spergel, S. T. Staggs, E. R. Switzer, R. Thornton, H. Trac, C. Tucker, A. Van Engelen, J. Ward, and E. J. Wollack. The Atacama Cosmology Telescope: CMB Polarization at $200¡\ell¡9000$. *ArXiv e-prints*, May 2014.

[50] A. Orlando, R. W. Aikin, M. Amiri, J. J. Bock, J. A. Bonetti, J. A. Brevik, B. Burger, G. Chattopadthyay, P. K. Day, J. P. Filippini, S. R. Golwala, M. Halpern, M. Hasselfield, G. C. Hilton, K. D. Irwin, M. Kenyon, J. M. Kovac, C. L. Kuo, A. E. Lange, H. G. LeDuc, N. Llombart, H. T. Nguyen, R. W. Ogburn, C. D. Reintsema, M. C. Runyan, Z. Staniszewski, R. Sudiwala, G. Teply, A. R. Trangsrud, A. D. Turner, and P. Wilson. Antenna-coupled tes bolometer arrays for bicep2/keck and spider. *Proc. SPIE*, 7741:77410H–77410H–10, 2010.

[51] L. Page, G. Hinshaw, E. Komatsu, M. R. Nolta, D. N. Spergel, C. L. Bennett, C. Barnes, R. Bean, O. Doré, J. Dunkley, M. Halpern, R. S. Hill, N. Jarosik, A. Kogut, M. Limon, S. S. Meyer, N. Odegard, H. V. Peiris, G. S. Tucker, L. Verde, et al. Three-Year Wilkinson Microwave Anisotropy Probe (WMAP) Observations: Polarization Analysis. *Astrophys. J. Suppl.* , 170:335–376, June 2007.

[52] Planck Collaboration XV. Planck 2013 results. XV. CMB power spectra and likelihood. *ArXiv e-prints*, March 2013.

[53] Planck Collaboration XVI. Planck 2013 results. XVI. Cosmological parameters. *ArXiv e-prints*, March 2013.

[54] C. Pryke, P. Ade, J. Bock, M. Bowden, M. L. Brown, G. Cahill, P. G. Castro, S. Church, T. Culverhouse, R. Friedman, K. Ganga, W. K. Gear, S. Gupta, J. Hinderks, J. Kovac, A. E. Lange, E. Leitch, S. J. Melhuish, Y. Memari, J. A. Murphy, et al. Second and Third Season QUaD Cosmic Microwave Background Temperature and Polarization Power Spectra. *Astrophys. J.* , 692:1247–1270, February 2009.

[55] QUIET Collaboration. First Season QUIET Observations: Measurements of Cosmic Microwave Background Polarization Power Spectra at 43 GHz in the Multipole Range 25 <= ℓ <= 475. *Astrophys. J.* , 741:111, November 2011.

[56] QUIET Collaboration. Second Season QUIET Observations: Measurements of the Cosmic Microwave Background Polarization Power Spectrum at 95 GHz. *Astrophys. J.* , 760:145, December 2012.

[57] A. C. S. Readhead, S. T. Myers, T. J. Pearson, J. L. Sievers, B. S. Mason, C. R. Contaldi, J. R. Bond, R. Bustos, P. Altamirano, C. Achermann, L. Bronfman, J. E. Carlstrom, J. K. Cartwright, S. Casassus, C. Dickinson, W. L. Holzapfel, J. M. Kovac, E. M. Leitch, J. May, S. Padin, et al. Polarization Observations with the Cosmic Background Imager. *Science*, 306:836–844, October 2004.

[58] U. Seljak. Measuring Polarization in the Cosmic Microwave Background. *Astrophys. J.* , 482:6–16, June 1997.

[59] U. Seljak and M. Zaldarriaga. Signature of Gravity Waves in the Polarization of the Microwave Background. *Phys. Rev. Lett.* , 78:2054–2057, March 1997.

[60] C. D. Sheehy. *Progress Towards a Detection of Inflationary B-modes with the BICEP2 and Keck Array Polarimeters* . PhD thesis, University of Chicago, 2013.

[61] C. D. Sheehy et al. The Keck Array: a pulse tube cooled CMB polarimeter. *Millimeter, Submillimeter, and Far-Infrared Detectors and Instrumentation for Astronomy V*, 7741(1):77411G, 2010.

[62] J. L. Sievers, C. Achermann, J. R. Bond, L. Bronfman, R. Bustos, C. R. Contaldi, C. Dickinson, P. G. Ferreira, M. E. Jones, A. M. Lewis, B. S. Mason, J. May, S. T. Myers, N. Oyarce, S. Padin, T. J. Pearson, M. Pospieszalski, A. C. S. Readhead, R. Reeves, A. C. Taylor, and S. Torres. Implications of the Cosmic Background Imager Polarization Data. *Astrophys. J.* , 660:976–987, May 2007.

[63] J. L. Sievers, R. A. Hlozek, M. R. Nolta, V. Acquaviva, G. E. Addison, P. A. R. Ade, P. Aguirre, M. Amiri, J. W. Appel, L. F. Barrientos, E. S. Battistelli, N. Battaglia, J. R. Bond, B. Brown, B. Burger, E. Calabrese, J. Chervenak, D. Crichton, S. Das, M. J. Devlin, et al. The Atacama Cosmology Telescope: cosmological parameters from three seasons of data. *J. Cosmol. Astropart. Phys.*, 10:60, October 2013.

[64] K. T. Story, C. L. Reichardt, Z. Hou, R. Keisler, K. A. Aird, B. A. Benson, L. E. Bleem, J. E. Carlstrom, C. L. Chang, H.-M. Cho, T. M. Crawford, A. T. Crites, T. de Haan, M. A. Dobbs, J. Dudley, B. Follin, E. M. George, N. W. Halverson, G. P. Holder, W. L. Holzapfel, et al. A Measurement of the Cosmic Microwave Background Damping Tail from the 2500-Square-Degree SPT-SZ Survey. *Astrophys. J.* , 779:86, December 2013.

[65] Y. D. Takahashi, P. A. R. Ade, D. Barkats, J. O. Battle, E. M. Bierman, J. J. Bock, H. C. Chiang, C. D. Dowell, L. Duband, E. F. Hivon, W. L. Holzapfel, V. V. Hristov, W. C. Jones, B. G. Keating, J. M. Kovac, C. L. Kuo, A. E. Lange, E. M. Leitch, P. V.

Mason, T. Matsumura, H. T. Nguyen, N. Ponthieu, C. Pryke, S. Richter, G. Rocha, and K. W. Yoon. Characterization of the BICEP Telescope for High-precision Cosmic Microwave Background Polarimetry. *Astrophys. J.* , 711:1141–1156, March 2010.

[66] J. E. Tolan. *Testing Inflationary Cosmology with Bicep2 and the Keck Array*. PhD thesis, Stanford University, 2014.

[67] J. H. P. Wu, J. Zuntz, M. E. Abroe, P. A. R. Ade, J. Bock, J. Borrill, J. Collins, S. Hanany, A. H. Jaffe, B. R. Johnson, T. Jones, A. T. Lee, T. Matsumura, B. Rabii, T. Renbarger, P. L. Richards, G. F. Smoot, R. Stompor, H. T. Tran, and C. D. Winant. MAXIPOL: Data Analysis and Results. *Astrophys. J.* , 665:55–66, August 2007.

[68] K. W. Yoon. *Design and Deployment of BICEP: A Novel Small-Aperture CMB Polarimeter to Test Inflationary Cosmology* . PhD thesis, California Institute of Technology, 2007.

[69] K. W. Yoon, P. A. R. Ade, D. Barkats, J. O. Battle, E. M. Bierman, J. J. Bock, J. A. Brevik, H. C. Chiang, A. Crites, C. D. Dowell, L. Duband, G. S. Griffin, E. F. Hivon, W. L. Holzapfel, V. V. Hristov, B. G. Keating, J. M. Kovac, C. L. Kuo, A. E. Lange, E. M. Leitch, P. V. Mason, H. T. Nguyen, N. Ponthieu, Y. D. Takahashi, T. Renbarger, L. C. Weintraub, and D. Woolsey. The Robinson Gravitational Wave Background Telescope (BICEP): a bolometric large angular scale CMB polarimeter. In *Society of Photo-Optical Instrumentation Engineers (SPIE) Conference Series*, volume 6275 of *Society of Photo-Optical Instrumentation Engineers (SPIE) Conference Series*, July 2006.